Title Page

Report Title: *Reactive Transport Models with Geomechanics to Mitigate Risks of CO_2 Utilization and Storage*

Type of Report: Final Scientific and Technical

Report Period: October 1, 2012 - December 31, 2015

Principal Author(s): Milind Deo, Hai Huang, Hyukmin Kweon, Luanjing Guo

Date Report was Issued: March 28, 2016

DOE Award Number: DE-FE009773

Name and Address of Submitting Organization: University of Utah, 201 S Presidents Circle, Salt Lake City, Utah 84112

DISCLAIMER

ABSTRACT

Reactivity of carbon dioxide (CO_2), rocks and brine is important in a number of practical situations in carbon dioxide sequestration. Injectivity of CO_2 will be affected by near wellbore dissolution or precipitation. Natural fractures or faults containing specific minerals may reactivate leading to induced seismicity. In this project, we first examined if the reactions between CO_2, brine and rocks affect the nature of the porous medium and properties including petrophysical properties in the timeframe of the injection operations. This was done by carrying out experiments at sequestration conditions (2000 psi for corefloods and 2400 psi for batch experiments, and 60^0C) with three different types of rocks – sandstone, limestone and dolomite. Experiments were performed in batch mode and corefloods were conducted over a two-week period. Batch experiments were performed with samples of differing surface area to understand the impact of surface area on overall reaction rates. Toughreact, a reactive transport model was used to interpret and understand the experimental results.

The role of iron in dissolution and precipitation reactions was observed to be significant. Iron containing minerals – siderite and ankerite dissolved resulting in changes in porosity and permeability. Corefloods and batch experiments revealed similar patterns. With the right cationic balance, there is a possibility of precipitation of iron bearing carbonates. The results indicate that during injection operations mineralogical changes may lead to injectivity enhancements near the wellbore and petrophysical changes elsewhere in the system.

Limestone and dolomite cores showed consistent dissolution at the entrance of the core. The dissolution led to formation of wormholes and interconnected dissolution zones. Results indicate that near wellbore dissolution in these rock-types may lead to rock failure. Micro-CT images of the cores before and after the experiments revealed that an initial high-permeability pathway facilitated the formation of wormholes.

The peak cation concentrations and general trends were matched using Toughreact. Batch reactor modeling showed that the geometric factors obtained using powder data that related effective surface area to the BET surface area had to be reduced for fractured samples and cores. This indicates that the available surface area in consolidated samples is lower than that deduced from powder experiments.

Field-scale modeling of reactive transport and geomechanics was developed in parallel at Idaho National Laboratory. The model is able to take into account complex chemistry, and consider interactions of natural fractures and faults. Poroelastic geomechanical considerations are also included in the model.

TABLE OF CONTENTS

LIST OF FIGURES

LIST OF TABLES

LIST OF ABBREVIATIONS

BET	Brunauer-Emmett-Teller
CO_2	Carbon Dioxide
CCS	Carbon Capture and Storage
CH_4	Methane
CT	Computerized Tomography
DI H_2O	Deionized Water
EDX	Energy Dispersive X-ray Spectroscopy
EGI	Energy and Geosciences Institute
GHG	Greenhouse Gas
He	Helium
HF	Hydrofluoric Acid
HNO_3	Nitric Acid
ICP-MS	Inductively Coupled Plasma Mass Spectrometry
N_2	Nitrogen
N_2O	Nitrous Oxide
NaCl	Sodium Chloride
QEMSCAN	Quantitative Evaluation of Minerals by Scanning Electron Microscopy
SEM	Scanning Electron Microscope
XRD	X-ray Diffraction

EXECUTIVE SUMMARY

In this project, sequestration experiments at around 2000 psi and 60^0C were undertaken with sandstone, limestone and dolomite samples and CO_2 and brine. Coreflooding and batch experiments with different types of samples (powdered, fractured, core) were performed. Analytical procedures included inductively coupled plasma mass spectrometry (ICP-MS) for aqueous phase effluents and X-ray diffraction (XRD), BET,QEM-scans, porosity measurements for solids. Selected Micro-CT analyses were performed. Modeling was performed using Toughreact. A reactive-transport, geomechanical simulator was developed at Idaho National Laboratory.

In sandstones dissolution of iron bearing minerals was prevalent. This was observed in corefloods and in batch experiments. This level of dissolution leads to increased porosity and permeability in the near injection region. Under favorable cationic environments, the iron may re-precipitate in the form of iron carbonates. The batch experiments conducted with samples of different surface areas helped determine the effective reactive surface areas for use in kinetic models. The factor to calculate these surface areas was obtained using QEM-scan and BET surface areas for core plug samples. However, when the actual sample areas increased (for powdered and fractured samples) it was necessary to use higher effective surface areas to match experimentally observed reaction rates.

Extensive dissolution resulting in the formation of wormholes and larger dissolution structures were observed in limestones and dolomites. In limestones, wormholes were formed in preferential permeability pathways, while in dolomites the dissolution was all pervasive due to the more heterogeneous nature of the rock.

Toughreact models were able to explain the data for the most part. The batch experiments Toughreact model provided kinetic rates of relevant reactions. The rates had the combined effect of the reaction rate constant and surface area. The surface area geometric factors were calculated using BET surface areas and QEM-scan surface areas. Less effective surface area is available for reactions as samples became more consolidated.

Reactive transport models and geomechanical models were developed by Idaho National Laboratory. Geomechanical model developed at Idaho National Laboratory showed that the injection has led to both slipping and dilation openings of natural fractures near injection well, which in turn significantly changes fracture network permeability and wellbore injectivity.

INTRODUCTION

The atmospheric concentrations of greenhouse gases (GHG), such as CO_2, methane (CH_4), and nitrous oxide (N_2O), have increased since the 20th century as a result of human activity. Land use (agriculture and deforestation) is the major factor in the increase in CH_4 and N_2O concentrations, and the use of fossil fuels for power generation, industrial processes, and transportation are the main causes of the increase of anthropogenic CO_2 concentration in the atmosphere. The greenhouse effect works as follows: energy arrives from the sun in the form of visible light and ultraviolet radiation. The Earth then emits some of this energy as infrared radiation. Greenhouse gases in the atmosphere capture some of this heat, then the heat is re-emitted in all directions – including back to the Earth's surface. Some studies indicate that the concentration of CO_2 in the atmosphere increased from 280 ppm to 380 ppm in 1994, and is expected to reach over 550 ppm by 2050.(Wang, Luo et al. 2011, Sohrabi, Kechut et al. 2012) CO_2 is categorized as the major anthropogenic GHG and it is believed it will cause climate changes and global warming if industry does not concern itself with CO_2 emissions.(Salimi, Wolf et al. 2012) Climate changes and global warming due to industrial CO_2 emissions has been recognized as a serious social concern since 1950.(Hoffert, Caldeira et al. 2002, Oelkers and Schott 2005) Fossil fuels have many advantages, such as low cost, high energy, abundant supply, etc. Nevertheless, fossil fuels emit high amounts of CO_2 into the atmosphere, resulting from combustion processes and transportation. Certain industrial processes such as cement making and land use changes also emit CO_2.(Siegenthaler 1987, Keeling 1997, Olajire 2013) The current situation of the greenhouse effect is formidable; therefore, reducing the emission of CO_2 to reverse climate changes and the global warming trend becomes a prime concern.(Bachu 2009, Court 2012) Under ongoing greenhouse gas emissions, available Earth System Models project that the Earth's surface temperature could exceed historical analogs as early as 2047, affecting most ecosystems on Earth and the livelihoods of over 3 billion people worldwide.(Mora, Frazier et al. 2013)

Recently, many countries have become aware of the significance of carbon emission reduction technologies. There are many technologies used to solve these problems; 1) Energy efficiency and conservation practices that reduce the consumption of carbon-based fuels, 2) Use of carbon-free and reduced-carbon energy sources, 3) Carbon capture and storage (CCS), and 4) Cap and trade and market-based controls, among which CCS has been considered as the most effective way to reduce carbon emission.(Zhou, Birkholzer et al. 2008) Energy efficiency and energy conservation are often referred to as the "cheapest and cleanest sources of energy." The benefits come in protection against rising energy costs and decreased demand for construction of new energy projects. The latter can translate into a cleaner environment and address climate change concerns. Energy efficiency and energy conservation also contribute to greater national security by reducing demand for other energy sources. Using carbon-free and reduced-carbon energy sources is one way to reduce carbon emissions. Carbon-free sources such as solar power, wind power, geothermal energy, nuclear power, etc. generate energy without producing and emitting carbon dioxide into the atmosphere. Another solution is switching from high carbon fuel such as coal and oil to low carbon fuels such as natural gas and biomass energy. For instance, the use of cultivated biomass fuels in place of fossil fuels such as coal, oil, and natural gas can result in a reduction in the amount of CO_2 that accumulates in the atmosphere, but only if the carbon released by the combustion of biomass fuels is effectively recaptured. There are two main ways to capture and sequester CO_2 to mitigate carbon levels in the atmosphere; terrestrial sequestration and geologic sequestration. Terrestrial sequestration involves the collection and storage of CO_2 by plants and the storage of CO_2 in soil. Geological sequestration involves collecting and placing CO_2 into suitable underground formations for storage. In general, in a cap and trade system, an entity establishes

an overall cap for CO_2 emissions within its region. Participants receive permits to emit CO_2 up to that limit. Participants can also purchase "carbon offset credits". A carbon offset credit is a kind of certificate stipulating that a certain amount of GHG was eliminated or avoided.

Carbon Capture and Storage (CCS) is the process of capturing CO_2 from industry and transporting it to a storage site. CCS has been considered for combating the global rise in CO_2 concentration and is a key technology which could be utilized to stabilize CO_2 concentrations to about 450 ppm. There are many options of CCS. First is terrestrial carbon capture and sequestration in which carbon is stored in forests or soils. Second is geosequestration in which CO_2 is stored in underground rock sites. CO_2 can be directly captured at the point of release, transported to a well site, and injected deep underground into the geologic formation. Chemical conversion can be used to convert CO_2 to another substance to use or sell again. The main purpose is to prevent the release of large quantities of CO_2 into the atmosphere. Many geological sequestration methods for storing CO_2 have attracted interest and been developed in order to manage CO_2. Sequestration sites in geological formations (see Figure 1), such as in saline aquifers, depleted oil and gas fields, and unmineable coalbeds, are considered the best geological storage sites.(Bachu 2008, Morris, Detwiler et al. 2011) CO_2 storage is believed to be particularly feasible in deep saline aquifers because of their large storage capacity and geological ubiquity. In addition, many studies show that most saline aquifers have low permeability.(De Silva, Ranjith et al. 2015, Rathnaweera, Ranjith et al. 2015, Song, Song et al. 2015) The research on the CO_2 flow and storage in low permeability saline aquifers has important significance for mitigating the greenhouse effect and improving CO_2 storage efficiency.(Okwen, Stewart et al. 2010, Castelletto, Teatini et al. 2013) Undoubtedly, several such projects have been implemented, and there are no known engineering problems that would prevent large-scale implementation of this form of CO_2 storage.(Kongsjorden, Kårstad et al. 1998, Kharaka, Cole et al. 2006) CCS can be implemented at a scale suitable for reducing the emissions of large point sources such as power plants, but high costs and concerns about the long-term containment of CO_2 in the storage reservoir have limited the global deployment of CCS.

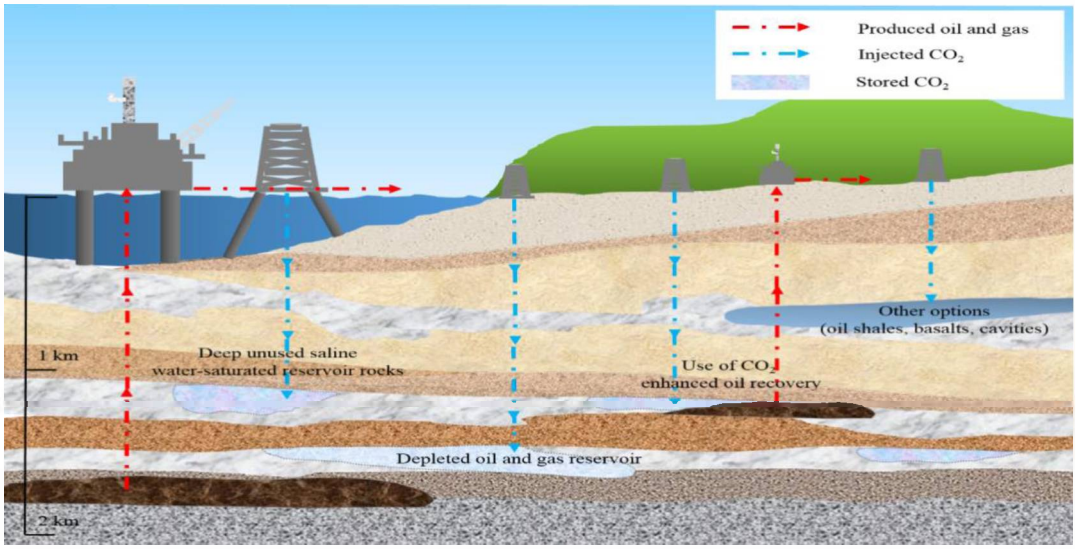

Figure 1. Options for storing CO_2 in deep underground geological formations

The subsurface is the Earth's largest carbon reservoir, where the vast majority of the world's carbon is held in coal, oil, gas, organic-rich shale, and carbonate rocks. Geological storage of CO_2 has been a natural

occurrence during the process of chemical weathering of surface terrains and the influence rates of erosion and element fluctuation in the environment for hundreds of millions of years.(Navarre-Sitchler and Thyne 2007) Geological storage of anthropogenic CO_2 as a greenhouse gas mitigation option was first proposed in the 1970s, but little research was done until the early 1990s. In a little over a decade, geological storage of CO_2 has grown from a concept of limited interest to one that is quite widely regarded as a potentially important mitigation option. One of the major reasons is that geological storage could help to make deep cuts to atmospheric CO_2 emissions. However, for the potential to be realized, geological storage must be the technically safe, environmentally sustainable, and capable of being broadly applied.

For CO_2 geological storage, the CO_2 gas must first be compressed to be supercritical state depending on the rate that temperature (geothermal gradient) and density of CO_2 will increase with depth (over 1 km). Geological storage of CO_2 can be undertaken in a variety of geological settings in sedimentary basins. Within these basins, oil fields, depleted gas fields, deep coal seams, and saline formations are all possible storage formations. Various fluids such as unwanted chemicals, pollutants, and by-products of petroleum production have been injected on a massive scale into the deep subsurface for many years.(Wilson, Johnson et al. 2003) Natural gas has also been injected and stored in the subsurface on a large scale in many parts of the world for many years. Depleted oil and gas fields and deep saline formations are the most likely candidate sites for geologic storage. Both depleted oil and gas fields and deep saline formations use the several trapping mechanisms as described below.

There are four primary CO_2 trapping mechanisms in saline aquifer formations which are hydrostratigraphic trapping, residual gas trapping, solubility trapping, and mineral trapping. These trapping processes take place over many years at different rates from days to years to thousands of years, but in general, geologically stored CO_2 becomes more securely trapped with time. Demonstrations of various methods of geological storage of CO_2 are already being carried out in a range of projects of varying scale. Hydrostratigraphic trapping is the most dominant of the trapping mechanisms. Once injected, the supercritical CO_2 can be more buoyant than other liquids that might be present in the pore space. The CO_2 will therefore percolate up through the porous rocks until it reaches the top of the formation where it meets an impermeable layer like a cap-rock. With an artificial CO_2 storage site, the wells that were drilled for injection through the cap-rock would be sealed with solid physical plugs made of steel and cement, a method which is already used extensively by the natural gas storage industry. Residual gas trapping happens very quickly as the porous rock acts like a tight, rigid sponge. As the supercritical CO_2 is injected into the formation, it displaces fluid as it moves through the porous rock. As the CO_2 continues to move, fluid again replaces it, but some of the CO_2 will be left behind as disconnected - or residual - droplets in the pore spaces which are immobile, similar to water in a sponge. This is often how the oil has been held for millions of years. Solubility trapping involves CO_2 dissolusion in other fluids in its gaseous and supercritical state. This phase in the trapping process involves the CO_2 dissolving into the brine already present in the porous rock. The brine containing CO_2 is denser than the surrounding fluids and so will sink to the bottom of the rock formation over time, trapping the CO_2 even more securely. Mineral trapping is the final phase of trapping resulting from the fact that when CO_2 dissolves in water it forms a weak carbonic acid. Over a long time, however, this weak acid can react with the minerals in the surrounding rock to form solid carbonate minerals. This process can be rapid or very slow depending on the chemistry of the rock and water in a specific storage site, but it effectively binds CO_2 to the rock. Such geological formations have cap rocks on top of the porous sedimentary rocks that could contain CO_2. Above all, saline formations are very deep, widely dispersed, porous rocks containing unusable water already trapped in the rocks. These conditions meet all the

necessary criteria to provide long-term storage. Therefore, deep saline formations contain most of the global geologic storage capacity for CO_2 and are likely to become the most widely used type of geologic storage site.

DePaolo and Orr (2008) describe the basic science challenges in geosciences research, stating that understanding complex interactions between pressurized fluids and porous rock is the key prerequisite to the safe sequestration of CO_2. They addressed the importance of understanding processes at atomic scales (with clay interlayer as an example) to seismic-imaging scales (several kilometers) and mentioned that it is critical to develop a relevant methodology to measure such scale-dependent processes over millennia. Geologic sequestration begins when CO_2 at temperature and pressure is injected into a well. There are a number of relevant processes at the surface that are important in sequestration, particularly the properties of CO_2 and CO_2-laden mixtures as they are injected into the subsurface.

The dynamics of CO_2 injection is one of the most important considerations. As CO_2 exits the injection tubing, it enters the perforated well casing and moves into the targeted geologic formation. The pressure distribution in the accommodating formations, along with the injection pressure distribution in the well casing, affects the flow rate profile of CO_2 into the formation on a macro-scale. The displacement of water/brine from around the wellbore by CO_2 through the perforations determines the injectivity on the wellbore scale. The water/brine/CO_2 interfacial properties are significant in this process. Understanding of the fluid-rock interactions at the microscopic level is critical in establishing a consistent framework for going from the molecular to microscopic to near wellbore to macro scales.

The injection process never reaches steady state in a strict sense, even though from a practical standpoint, the injection rates may remain constant over extended periods of time. This is because the pressure in the formation continues to adjust, and readjust according to the operating conditions, and in response to dynamic changes occurring in the system. CO_2, being lighter than water, overrides the water and reaches the top of the formation. On a macro-scale, it is important to capture such a buoyancy-driven transport, since it affects all aspects of CO_2 trapping. The dissolution of CO_2 at the interface, creating a heavier fluid and causing density-driven instabilities has been studied (DePaolo and Orr, 2008; Riaz and Tchelepi, 2007; Ennis-King et al., 2005).

CO_2 injection will increase the CO_2 partial pressure and fugacity, which will promote CO_2 dissolution into reservoir fluids. CO_2 dissolution will decrease the pH of the residual brine and increase the concentration of bicarbonates. Other dissolved species also typically increase due to the dissolution of high-solubility carbonate minerals. Mineral dissolution/precipitation is more complicated because it strongly depends on the type of host rock, pH, and brine chemistry. Mandalaparty et al. (2011) showed that after an initial period of dissolution, carbonate re-precipitation is likely depending on the mineralogy and mix of cations present in the system. In addition, rates of fluid flow, such as in diffusion- and advection-controlled environments, also govern the rate of water-rock interaction. As the sequestration process continues, carbonic acid continually reacts with the minerals in place. Mineral reactions result in either dissolution or precipitation. This leads to the creation or reduction of pore space. Pore space dynamics are relevant in defining the ultimate capacity for CO2, and also affect pressure propagation/equilibration. Thus, the injectivity of CO_2 is also impacted. Superposition of the concentration gradients and heterogeneity in the aquifer makes prediction of these irreversible changes in the system challenging. Reactivity of caprock and other seals is particularly important, since this will lead to CO_2 leakage either into other formations or to the surface. Rock properties, including the in-situ stress state, evolve as these changes unfold. These changes in the

target formation and its environs are also important for several reasons. Stress, pressure or physical/mechanical property changes may lead to initiation or re-activation of fractures/faults or in the creation of new micro- and macro-features. This would lead to possible CO_2 leakage or induction of seismicity.

In this project we studied the reactive CO_2-brine-rock system experimentally for three different rock types – sandstone, limestone and dolomite. Reactive transport models were used to explain the data. A reactive transport model with geomechanical capabilities was developed at the Idaho National Laboratory.

Experimental Section

Before conducting the core flooding experiments, it was necessary to understand the composition of the core samples. The core samples were ground using a wire-saw to make powder samples. To determine these properties, X-ray diffraction (XRD) and inductively coupled plasma mass spectrometry (ICP-MS) were utilized. XRD was used to detect all relevant constituents found in the unreacted samples. For XRD analysis, the samples were mixed with deionized water (DI H_2O) and further ground in a micronizing mill until fine enough to pass through a 325 mesh screen. The solution was then applied to a glass slide using a pipette. Once the sample had dried, an XRD pattern was obtained.

Prior to ICP-MS analysis, unreacted core samples were digested using hydrofluoric acids for ICP-MS. Typically, 100 mg of solid are treated with 5 ml concentration of HNO_3 and 5 ml concentration of HF. The samples are dried, and the process repeats 2-3 times. As expected, the sandstone is primarily quartz, but contains iron, calcium, magnesium, and potassium. Limestone is dominated by the presence of calcium. Magnesium is the next most prominent cation present. Last, calcium and magnesium are distributed in dolomite as a similar component ratio. General core properties of unreacted sandstone, limestone, and dolomite cores are shown in Table 1.

Table 1. Mineralogical compositions of unreacted sandstone, limestone, and dolomite core used in the experiments

		Sandstone	Limestone	Dolomite
Composition (Based on XRD)	Kaolinite	2.51 %	-	-
	Oligoclase	1.52 %	-	-
	Clinochlore	1.08 %	-	-
	Illite	4.58 %	-	-
	Sanidine	4.20 %	-	-
	Calcite	-	99.34 %	-
	Quartz	86 %	0.49 %	0.32 %
	Dolomite	-	0.17 %	99.68 %
Elements (Based on ICP-MS)	Mg (mg/kg)	1034	3959	178764
	K (mg/kg)	1047	871	629
	Ca (mg/kg)	1703	497661	283987
	Fe (mg/kg)	4655	205	216

In the core flooding experiments with sandstone, limestone, and dolomite, each of the cores were approximately 7 inch in length and 1.5 inch in diameter. Originally, each of the sandstone, limestone, and dolomite cores were 8 inch in length. A 1 inch end section of each core was removed. These 1 inch core sections were analyzed using the helium porosimeter (Core Lab, Ultra-Pore 300) to provide the unreacted porosity. Before placing the cores in the core holder, they were wrapped with a heat shrinking material (FEP tubing) in order to isolate core pressure from the confining pressure. The core was then placed inside of the core holder and the core holder was secured inside of an oven.

For the batch reactor experiments, core plugs were taken from 1 inch cores consisting of sandstone, limestone, and dolomite. First, a 1 inch section of the 8 inch in length core was cut using a blade saw. After that, the 1 inch section was divided to two 1/2 inch sections. Multiple core plugs were taken from the one

of 1/2 inch sections of the core using a drill press (3/8 inch drill bit). Two additional experiments were carried out because the surface reactions on each core plug were expected to be quite slow and not very active in the batch reactors. To increase activity, one of the simplest methods is to increase the surface area. Adding fractured and powder samples enhanced reactivity and maximized reaction rates. The core plugs were crushed and ground to provide various forms with different surface areas. The additional experiment results allowed for comparisons according to the changes in shape and also surface area.

Core Flooding System

The core flooding apparatus used in these experiments is shown in Figure 2. The main components of the experimental apparatus were a dual syringe pump system (Teledyne Technologies International Corp, ISCO D-500 series) for continuous flow, a supercritical CO_2 pump (Supercritical Fluid Technologies, INC, SFT-10), a syringe pump (Teledyne Technologies International Corp, ISCO D-500 series) for confining fluid, a core holder (Harbert Engineering, Hassler Core Cell), a high temperature oven, a pressure transducer, a back-pressure regulator (EQUILIBAR, EB1HP1), and a gas regulator.

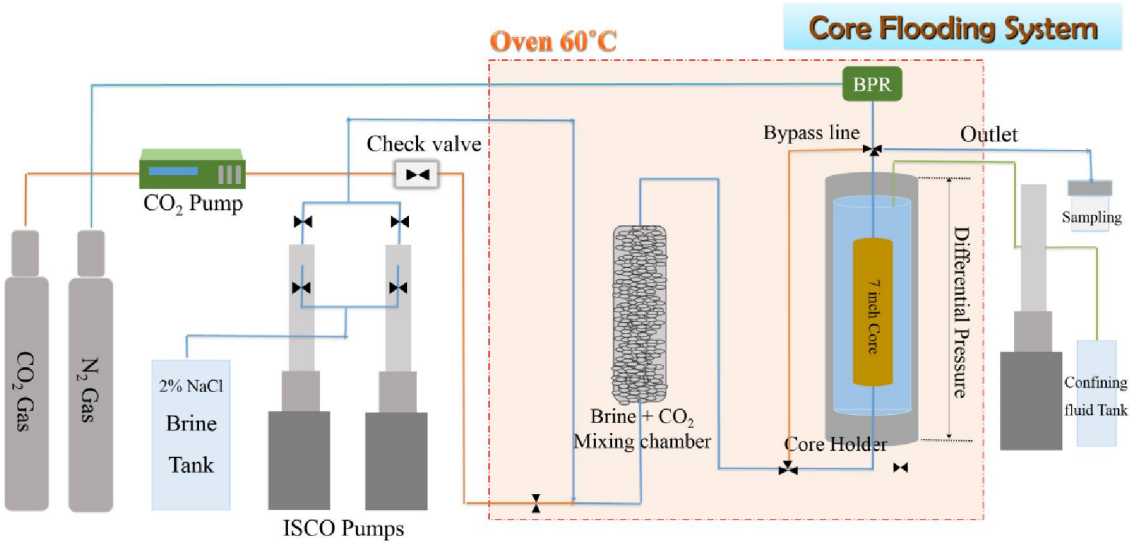

Figure 2. Schematic diagram of the core flooding system.

The confining pressure was set to 3000 psi for sandstone and limestone and 3500 psi for dolomite, and the temperature of the oven was set to 60 °C. A 2% NaCl brine solution was pumped from the dual syringe pump system through a 500 ml stainless steel mixing chamber within the oven and then into the core holder. A CO_2 cylinder was attached to a supercritical CO_2 pump capable of pressurizing the CO_2 to supercritical conditions and pumping it through the system at a constant flow rate.

The 500 ml stainless steel chamber was put in place in order to facilitate in the mixing and heating of the CO_2-brine mixture before entering the core holder. The back-pressure regulator was set to 2000 psi for sandstone and limestone, and 1500 psi for dolomite using an N_2 tank. The outlet from the back-pressure regulator was directed to a product-collecting container outside the oven.

The flow rate of brine remained constant for each of the sandstone, limestone, and dolomite experiments, being 0 ml/min (blank CO_2 run), 0.5 ml/min, and 1 ml/min. The CO_2 flow rates were different. For

sandstone core flooding experiments, three different CO_2 flow rates were tested – 2.82 ml/min, 1.41 ml/min, and 0 ml/min (blank brine run). For limestone and dolomite, the three different flow rates of CO_2 were – 1.41 ml/min, 0.71 ml/min, and 0 ml/min (blank brine run). The flow rates of 0 ml/min in among sandstone, limestone, and dolomite were chosen to represent a blank test to compare with other experimental results. The different flow rates were chosen to verify the hypothesis that brine with a higher CO_2 saturation would be more reactive.

Batch Reactor System

The batch reactor experiment was organized with four similarly constructed batch reactors. Each of these reactors had a pressure gauge with a maximum reading of 3000 psi, stainless steel fittings and tubing, and a valve with a maximum pressure of 3500 psi at 50 °C. The lower portion of the batch reactors consisted of tubing that was 1/2 inch in diameter and had a cap on the bottom end (Figure 3). This is where the sample of each rock type would presumably reside during the experiment. The valve was used as both an inlet and an outlet valve. The cap was removed from the bottom end of the 1/2 inch tubing and different rock types and forms were inserted into the bottom of the reactor, and then using a micropipette, 5 ml of brine was injected into the reactor submerging the rock samples in brine. The bottom cap was then secured and tightened. The valve cap was then removed to inject CO_2 into the reactor. The CO_2 pump outlet was attached to the reactor inlet where the valve cap was removed. The valve was opened and the reactor pressure reached the CO_2 tank pressure, which was 720-740 psi. A supercritical CO_2 pump was utilized. Prior to CO_2 injection, the pump had initially cooled for 20 minutes. After the pump was cooled, the CO_2 injection rate was increased to pressurize the reactor to around 830 psi for reactors with rock sample and to around 840 psi for the blank test.

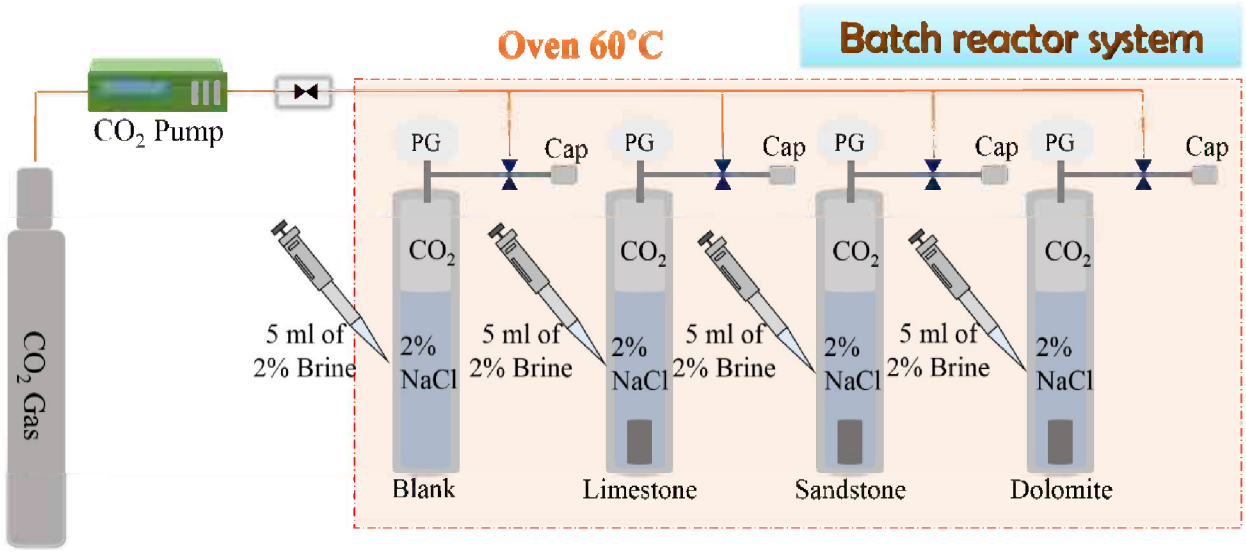

Figure 3. Schematic diagram of the batch reactor system

Once the reactors were pressurized, they were placed in an oven at 60 °C. The reactor pressure increased inside the oven due to the increased temperature. The pressure increase was gradual until reaching around 2400 psi. At this temperature and pressure, CO_2 entered a supercritical phase.

Within the oven, a small fan was inserted in order to keep the circulation of air constant. A thermometer was inserted into the top portion of the oven in order to easily read the internal temperature. A small rack was built in order to hold the reactors within the oven and preventing them from resting on the bottom of the oven where the main source of heat was generated.

After the two-week period was completed, the reactors were removed from the oven and cooled to room temperature. After being cooled, a small vial was placed over the opening of the valve and it was then opened, releasing the CO_2 gas and capturing the brine mixed inside of the vial. For the experiments with core plugs and fractured core samples, the effluent was separated simply by pouring it into a vial from the reactor. The rock samples were then set aside to dry. When performing the reaction with the powder samples, a filtration system was implanted in order to separate the samples from the liquid. This was done by rinsing the reactor free of the powder with an additional 60 ml of DI H_2O. The dilution rate was measured and used to convert the ICP-MS data accordingly.

Sample Characterization

X-ray Diffraction (XRD)

X-ray diffraction (XRD) analyses were done at the University of Utah Energy and Geosciences Institute (EGI). EGI performed on each sample using a Bruker D8 Advance X-ray diffactometer. Phase quantification using the Rietveld method was performed using TOPAS software, developed by Bruker AXS. The Rietveld method fits the peak intensities calculated from a model of the crystalline structure to the observed X-ray powder pattern by a least squares refinement. This is done by varying the parameters of the crystal structures to minimize the difference between the observed and calculated powder patterns. Because the whole powder pattern is taken into consideration, problems of peak overlap are minimized and accurate quantitative analyses can be obtained.

The following operating parameters were used when analyzing the bulk samples: Cu-K-α radiation at 40 kV and 40 mA, 0.02° 2θ step size, and 0.6 seconds per step, for bulk samples. Bulk samples were examined from 4 to 65° 2θ. The instrument is equipped with a lynx eye detector which collects data over 2.6 mm, rather than at a point, greatly increasing X-ray counts collected and decreasing acquisition time; and a rotating sample stage, which increases the mineral grain orientations encountered by the incident electron beam.

Quantitative Evaluation of Minerals by Scanning Electron Microscopy (QEMSCAN)

In order to compensate for the limits of XRD, Quantitative evaluation of minerals by scanning electron microscopy (QEMSCAN) analysis was conducted for the pre- and post- experiment core. The analysis was completed on a QEMSCAN 4300, which is built on a Zeiss Evo 50 SEM platform with four light elements BrukerX flash energy dispersive X-ray detectors. Energy dispersive X-ray spectral analysis (EDX) involves the interpretation of secondary X-ray spectra to determine elemental composition, and ultimately mineralogy. This instrument is currently iMeasure v.5.3 software for the data acquisition, and iDiscover v.5.3 for the spectral interpretation and data processing. The measurements were collected in field-scan mode, and X-ray data were collected every four on the polished thin sections. Prior to each analysis, standard instrument tuning was performed, including beam focusing, beam alignment, and calibration of the X-ray detectors and backscatter. A measurement procedure is entered and the analyses are automated. The QEMSCAN was operated using a accelerating voltage 20 kV and a specimen current of approximately 5 nA.

Inductively Coupled Plasma Mass Spectrometer (ICP-MS)

The determination of iron, calcium, magnesium, and potassium was performed using a quadrupole inductively coupled plasma mass spectrometer (Agilent, 7500ce) with a double-pass spray chamber; PTFE 100 µl/min nebulizer, platinum cones, and sapphire injector within a quartz shielded torch.(Carling 2012) The sample handling and chemistry was performed in laminar flow benches. An external calibration curve containing iron, calcium, magnesium, and potassium was freshly prepared from 1000 mg/l single elemental standard solutions in HNO_3 (Inorganic Ventures). Both the samples and the calibration solutions were prepared in 2.4 % HNO_3 (BDH Aristair Plus). Indium at a concentration of 20 ppb was added to calibration curve, samples, and blanks as internal standard. Samples were diluted 1:200 and run in the ICP-MS using 4 ml He/min in the collision cell. Silicon was determined on a separate run, with the samples diluted 1:2. Chloride was determined using an ion chromatograph (Metrhom 881).

Helium (He) Porosimeter

Samples for the helium porosimeter were prepared by cutting a 1 inch core section from the end of an 8 inch in length core with a 1.5 inch in diameter. This was done for twelve different 8 inch in length cores, four each for sandstone, limestone, and dolomite. The top and bottom of these 1 inch core sections were then leveled using a grinder. The average diameter and thickness of each core section was measured and a "caliper bulk volume" measurement was calculated. This measurement is based on the assumption that the core section is a cylinder. The core sections were exposed to an air stream in order to clear off excess dust and particles that resulted from using the grinder. A matrix cup connected to the helium porosimeter was then used to calculate the grain volume (GV) and calculate the pore volume (PV) and porosity (ϕ) of sandstone, limestone, and dolomite core sections. After measuring the grain volume of a core section, the porosimeter program then calculated the pore volume using the following equation:

$$Pore\ Volume = Bulk\ Volume - Grain\ Volume \qquad (2)$$

The computer program then calculated the porosity of the core section using:

$$\phi = \frac{Bulk\ Volume - Grain\ Volume}{Bulk\ Volume} = \frac{Pore\ Volume}{Bulk\ Volume} \qquad (3)$$

Before each use, the helium porosimeter was calibrated using five calibration disks with different volumes. A ten-point calibration was performed before analyzing each set of core sections. Each core section was measured for porosity five different times and the average porosity of each core section was then calculated.

Micro-Computed Tomography (Micro-CT)

Application of the computed tomography at the microscale level (microtomography) allows for the quantitative examination of porosity changes.(Miller 2003, Lin 2005, D. Garcia 2006) A Micro-CT (The XCT-400) was used for 7 inch limestone core samples. XCT-400 method is based on a 3D reconstruction from one-thousand 2D radiographs of the X-ray attenuation properties of various materials forming an

object.(Tiwari 2013) The optical system used in the experiment provides an optical resolution of 42 microns. Each data set is 1014×1024×1012 voxels. To measure porosity change in core plug samples, a Micro-CT (XCT-400) was also used. The optical system used in the experiment provides an optical resolution of 1.85 microns. The reconstruction provides 3D images of the X-ray absorption by the different materials in the sample. Each data set is 986×1005×968 voxels. Different magnification levels were utilized in analyzing the samples: 4X for core plugs. For 4X, 80 kV of voltage and 9 seconds of exposure time were used.

Surface Area Analysis (BET)

The BET surface area and porous structure of the various types and forms of core samples were determined by the single point BET/Nitrogen (N_2) method based on the quantity of gas that adsorbs as a single layer of molecules on the rock surface at a temperature of -196 °C using a Micrometric Tristar II. Approximately, 0.6 g of each sample was loaded into a glass sample tube. Immediately preceding surface area analysis, the samples were degassed at a minimum temperature of 100 °C for at least 4 hours on the degassing station. A mixture of 30 % N_2 / 70 % Helium (He) was used as a gas supply and analyses were carried out at atmospheric pressure and at liquid N_2 temperature.

Results and Discussion

Mineralogical changes in core flooding system

Core Analysis: X-ray Diffraction

X-ray diffraction (XRD) was used to detect mineralogy found in the unreacted and reacted sandstone core samples with different CO_2 injection rate in core flooding system. XRD spectra present a different intensity of mineralogy before and after the experiment, especially in quartz. However, the trends do not change significantly because there are no changes of crystallization and structure in the quartz.

In order to compare quantitative differences, one method is measure the unreacted dominate mineral intensity before and after the reaction. For the mineralogical composition of sandstone core samples (see Table 1), quartz is the dominant mineral. The quartz intensity in each sandstone core was determined before and after the reaction under different CO_2 flow rate conditions. The unreacted core includes around 86 % of quartz. The quartz does not react with supercritical CO_2 and brine solution. In XRD analysis, the mineralogical percentages are based on the relative amount of each mineral in the sandstone sample. This means when the quartz intensity is increasing relatively, the concentration of other minerals such as kaolite, illite, smectite are decreasing relatively; dissolving in the effluent. However, the intensities of the other minerals are not significant because the XRD analysis is more of a bulk measurement, and does not accurately detect the small changes.

Based on the XRD spectra of quartz (Figure 4), the quartz intensity is affected by the CO_2 injection rate. The unreacted sandstone and the brine without CO_2 intensities are similar around 25000. The brine with CO_2 at a low flow rate (1.41 ml/min) shows a higher intensity around 35000, and the brine with CO_2 at a high flow rate (2.82 ml/min) has the highest intensity around 40000. Concluding that at higher CO_2 flow rates the quartz intensity is increased further showing that reactive lower concentration minerals were dissolved.

XRD spectra (Figure 5 and Figure 6) of unreacted and reacted limestone and dolomite core samples were also taken. Due to the high quantities of calcite minerals in limestone and dolomite minerals in dolomite, the XRD spectra data showed the intensity of calcite remained relatively constant 99.34 % in limestone core samples and the intensity of dolomite remained relatively constant 99.28 % in dolomite core samples. Because of the limitations of XRD data as a bulk measurement the small changes in the calcite and dolomite intensities are not enough to make a conclusion for limestone and dolomite.

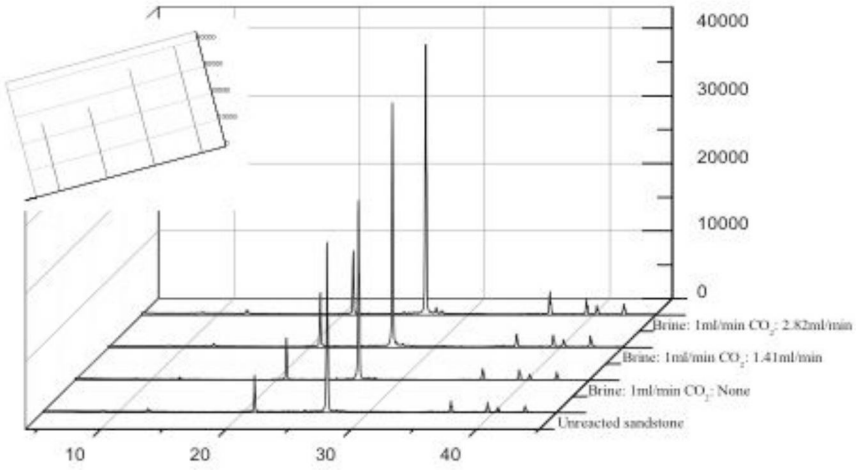

Figure 4. XRD Spectra lines of unreacted and reacted sandstone core samples under various CO_2 injection rate conditions

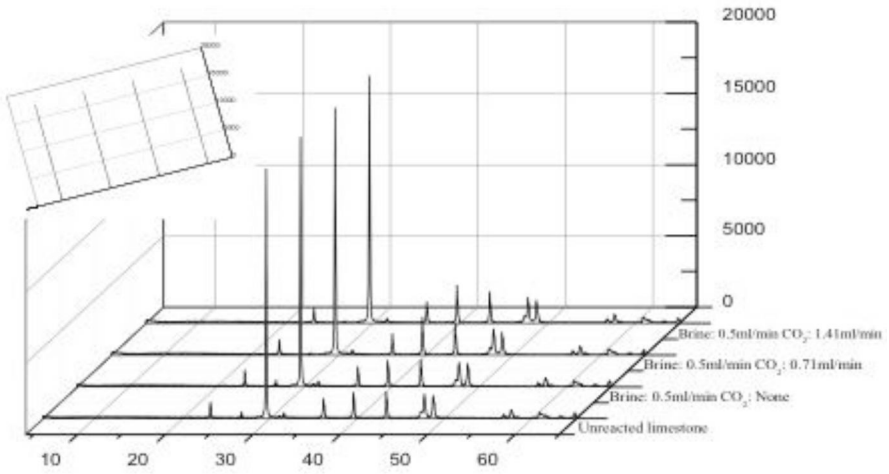

Figure 5. XRD Spectra lines of unreacted and reacted limestone core samples under various CO_2 injection rate conditions

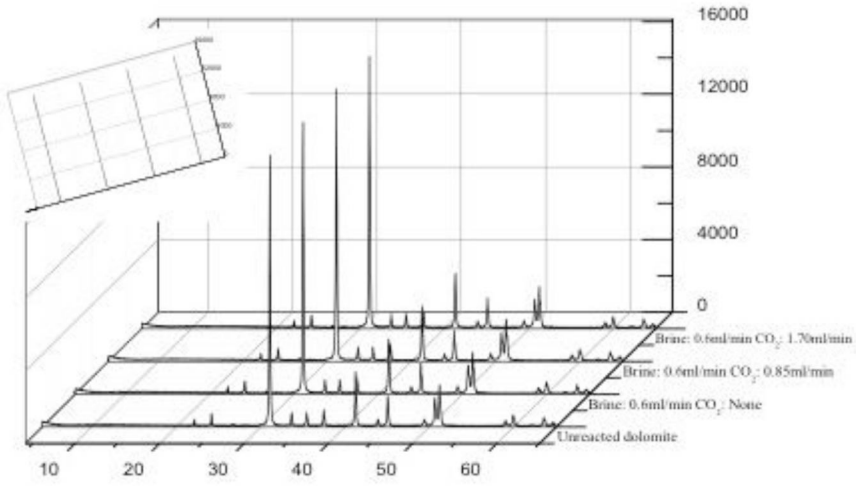

Figure 6. XRD Spectra lines of unreacted and reacted dolomite core samples under various CO_2 injection rate conditions

Core Analysis: QEMSCAN Imaging

In order to compensate for the limits of XRD, QEMSCAN analysis was conducted. For QEMSCAN analysis, each reacted core was divided into 21 sections making 63 sections in total or 63 total data points. Figure 7 contains an image of each core divided into 21 sections each. Sections 1-21 make up the blank core, sections 22-42 make up the low CO_2 flow rate core, and sections 43-63 make up the high CO_2 flow rate core.

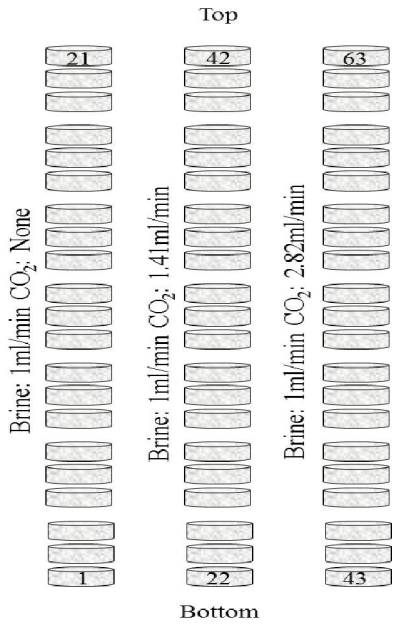

Figure 7. Sandstone post-experimental cores divided into 21 sections for QEMSCAN analysis. Sections 1-21 make up the blank core, sections 22-42 make up the low CO_2 flow rate core, and sections 43-63 make up the high CO_2 flow rate core

Figures 8-10 show mineral concentrations based on QEMSCAN results. The QEMSCAN analysis confirmed that quartz is the dominate mineral in sandstone with minor amounts of illite, kaolinite, smectite, chlorite, siderite, and ankerite. Overall, the mineralogical distributions in the rock are evenly distributed throughout.

A QEMSCAN of the unreacted sandstone core showed that the cores were comprised of approximately 6% by area illite, 3% by area kaolinite, 0.9 % and 0.8 % by area chlorite and smectite, and less than 0.2 % by area siderite and ankerite. The compositions of the unreacted core are represented by a solid line in each figure. After the reaction with brine and no CO_2 (Figure 8, left), QEMSCAN showed that illite concentrations at the bottom of the core decreased but not so much as it progressed up the core, meaning brine reacted initially with illite but less reaction took place further up the core. After the reaction, around 5% by area illite remained in the core. Kaolinite concentration remains relatively constant after the brine only experiment. The other minerals believed to be the iron source in sandstone are presented in Figure 8 (right). There are no significant concentration changes in these minerals after the brine only experiment. When brine and CO_2 are injected at 1 ml/min and 1.41 ml/min, respectively, the illite concentration decreased to around 4% throughout the entire core. Kaolinite concentration remains unaffected and the concentration stays around 3 % (Figure 9, left). Figure 9 (right), shows the iron containing minerals. Smectite concentration remains constant around 0.7 % and chlorite concentration is decreased more in the inlet section around 0.2 % and around 0.8 % at the outlet section. Ankerite and siderite are completely dissolved after the injection of brine and CO_2.

After the CO_2 injection flow rate was increased to 2.82 ml/min and brine injection rate remained at 1 ml/min, illite dissolution was increased. Illite concentration had decreased to around 3.7 %. Kaolinite concentration remained unchanged around 3 %, (Figure 10, left). Figure 10 (right) shows that smectite was slightly dissolved in this experiment. Smectite concentration decreased to around 0.6 %. Chlorite concentration decreased throughout the entire core. The trend is similar to the previous injection rate (CO_2 1.41 ml/min and brine 1 ml/min), but the overall concentration is slightly lower, 0.2 % at the inlet section and 0.5 % at the outlet section. At this flow rate, condition siderite and ankerite were completely dissolved as in the case of CO_2 injection of 1.41 ml/min and brine injection of 1 ml/min.

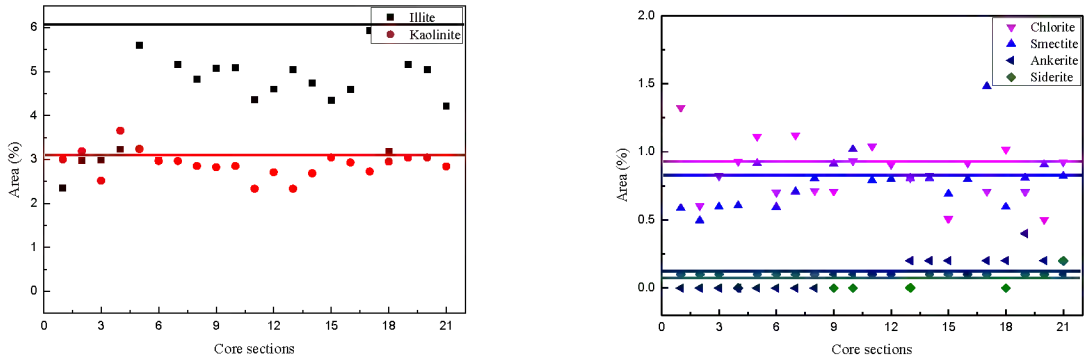

Figure 8. Illite, kaolinite, smectite, chlorite, siderite, and ankerite concentrations (Area %) of each reacted core section under brine only condition; acquired through QEMSCAN analysis

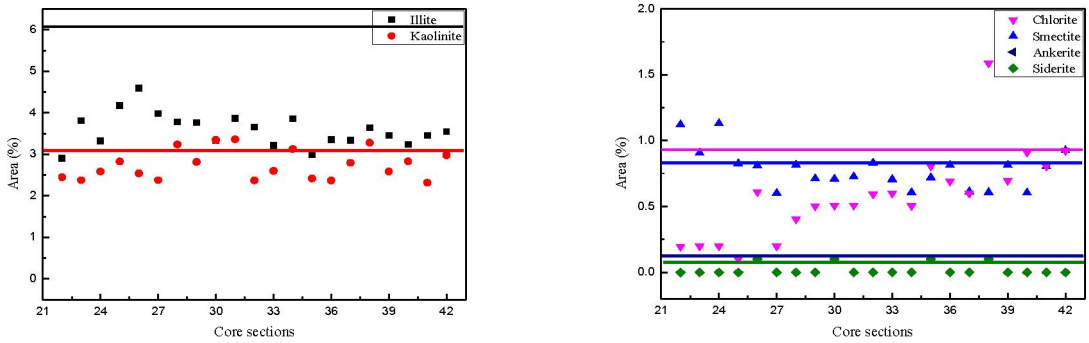

Figure 9. Illite, kaolinite, smectite, chlorite, siderite, and ankerite concentrations (Area %) of each reacted core section under 1 ml/min brine and 1.41 ml/min CO_2 injection conditions; acquired through QEMSCAN analysis

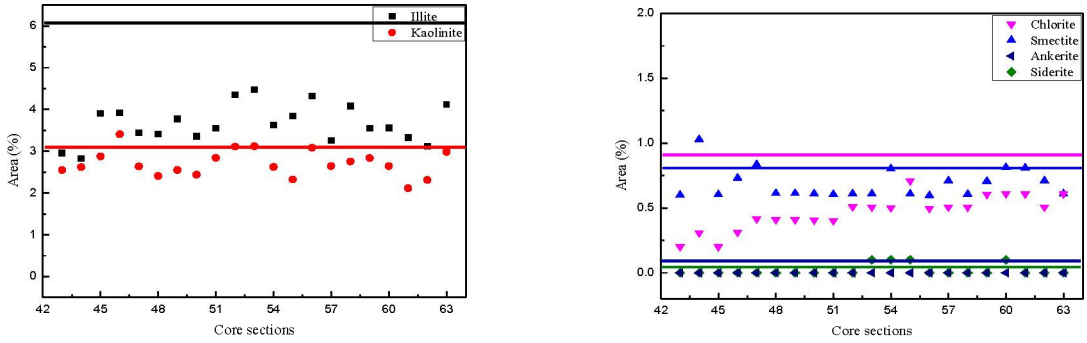

Figure 10. Illite, kaolinite, smectite, chlorite, siderite, and ankerite concentrations (Area %) of each reacted core section under 1 ml/min brine and 1.41 ml/min CO_2 injection conditions; acquired through QEMSCAN analysis

Effluent Analysis: ICP-MS

To begin the core flooding experiment, the brine was pumped through the system to the pressure set by the back-pressure regulator; the outlet line would remain dry. Once the pressure of the system reached target pressure about 1500 to 2000 psi, the first drops of effluent would pass through the outlet line and into the product collecting container. Post-experiment fluid samples were taken and analyzed to ensure that brine chemistry, component analysis, and concentration measurements between rock and brine were achieved.

In preliminary tests on a sandstone core, the product collecting container was changed once every day and a sample of this outlet fluid was then analyzed using ICP-MS. This preliminary data suggested that for most minerals, the content was high in the beginning of the experiment and decreased as time elapsed. To more fully understand how these mineral concentrations changed over injected pore volume, it was necessary to divide the samples into smaller increments and view the concentrations in a more continuous manner. It was hypothesized that most of the concentration changes would occur within a short span of time and after this time had elapsed the change in concentration would be slow. To ascertain this more continuous view of mineral concentration, the outlet container was changed as follows: every 1 hour for 24 hours, every 2 hours for 12 hours, every 4 hours for 12 hours, every 8 hours for 24 hours, and then every 24 hours for the remainder of the experiment. These results allow us to make conclusions about the mineralogical concentrations as experimental time proceeds.

pH values for all of the effluent samples were within the 5.2 to 5.6 range. Each of the collected fluids was analyzed using ICP-MS. The mineralogical concentrations of iron, calcium, magnesium, and potassium have been plotted over time for sandstone in Figure 11 for limestone in Figure 12 and for dolomite in Figure 13, respectively. In each of the mineral concentrations plotted, the blank test tends to have relatively low values for the elements throughout the time period with the exception of a few large spikes at the beginning of the experiments.

The results of the iron concentration in the sandstone experiments with low and high CO_2 flow rates are of particular interest (Figure 11(a)). It is seen from Table 1 that the iron concentration in sandstone was about 4655 ppm. The source of iron is a combination of minerals such as ankerite, siderite, smectite, and illite. Both of the flow rates exhibit the same trends in their iron concentrations, although the concentrations of iron in the higher CO_2 flow rate are higher at each point. The concentrations begin near zero and then increase rapidly until reaching a smooth peak. After reaching the smooth peak, the iron concentration begins to decrease but at a more gradual rate. Eventually, the rate of change in the iron concentration begins to taper off and the concentration begins to become steadier towards the end of the experimental time. Interestingly, the final iron concentration of each flow rate is approximately the same. From these results, it can be determined that the higher flow rate of CO_2 results in greater iron reactivity from the minerals within the sandstone core. This suggests that the decrease in pH that results from an increase in CO_2 concentration contributes to the greater dissolution of iron in sandstone.

Sandstone does contain some calcite, which is the source of the calcium cations. Figure 11(b) show the trend is an increase in calcium concentration at the beginning of the experiment and then a continual decrease until it reaches a steady concentration towards the end of the experiment. The result for the higher flow rate of 2.82 ml/min is especially interesting because the final concentration that it reaches is near zero, whereas the steady concentration for the lower flow rate of 1.41 ml/min is quite a bit higher at around 50

ppm. The changes in effluent concentrations for the different flow rates are a result of the competing reaction (dissolution) and transport phenomena. The magnesium concentrations in the sandstone effluent samples initially decrease rapidly in concentration until approaching a much lower rate of change (Figure 11(c)). When both magnesium concentrations level off, the concentration of magnesium from the higher CO_2 flow rate remains higher than the magnesium concentration from the lower flow rate. This indicates a lower rate of dissolution of magnesium containing minerals. The potassium concentrations in the sandstone effluent samples peak quickly and decrease to low ppm values, again indicating dissolution process (Figure 11(d)).

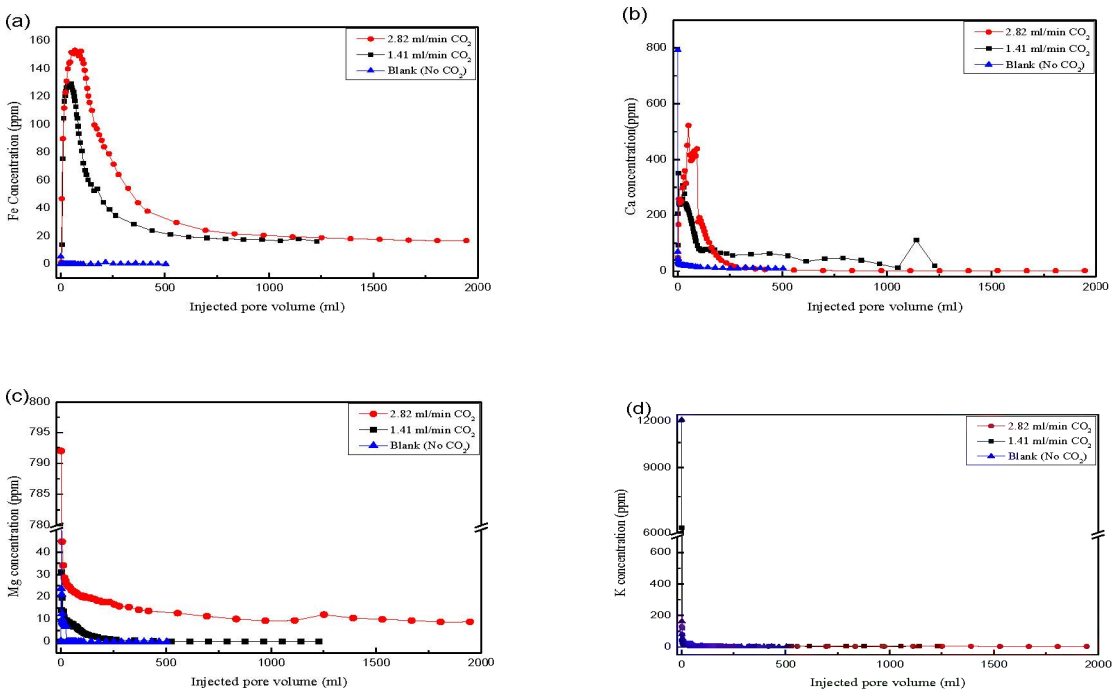

Figure 11. Concentration of iron, calcium, magnesium, and potassium ions as measured by ICP-MS in the effluent for sandstone flooding experiments

Effluent concentrations of iron, calcium, magnesium, and potassium, for limestone are shown in Figure 12, respectively. The iron concentration in the limestone effluent samples is much lower when compared to the sandstone effluent samples (Figure 12(a)). Concentration differences of iron at the two different CO_2 flow rates are not significant. The limestone core is mainly calcite, based on the XRD analysis, and does not include a high percentage of iron based minerals.

Predictably, the calcium concentrations in the limestone effluent samples are much higher (Figure 12(b)). The concentration of calcium increases rapidly with both the high CO_2 and low CO_2 flow rates. The experiment with high CO_2 flow rate was stopped after around 48 hours. This was due to excessive dissolution on one edge of the core at the core holder inlet. Due to the dissolved section of the core, the confining fluid began to generate a small pinhole within the heat shrinking tube at this location. Once the confining pressure had penetrated the heat shrinking tube, the confining pressure and core pressure began to equalize. When this occurred the experiment could not properly proceed under the desired conditions.

When comparing the first 36 hours of the low CO_2 and high CO_2 flow rates, it is apparent that the higher CO_2 flow rate results in a large concentrations of calcium in the limestone effluent samples.

This effect is similar to the iron concentrations in that it suggests that the pH of the working fluid affects the reactivity of the minerals. The concentration of calcium in the effluent does appear to be stable at around 600 ppm, even for higher CO_2 flow rate. This would be in contrast to the results of the sandstone calcium concentrations that display lower concentrations of calcium in the high CO_2 flow rate effluent samples towards the end of the experiment. This is attributed to the much higher concentration of calcium in limestone and a relatively low calcium concentration in sandstone.

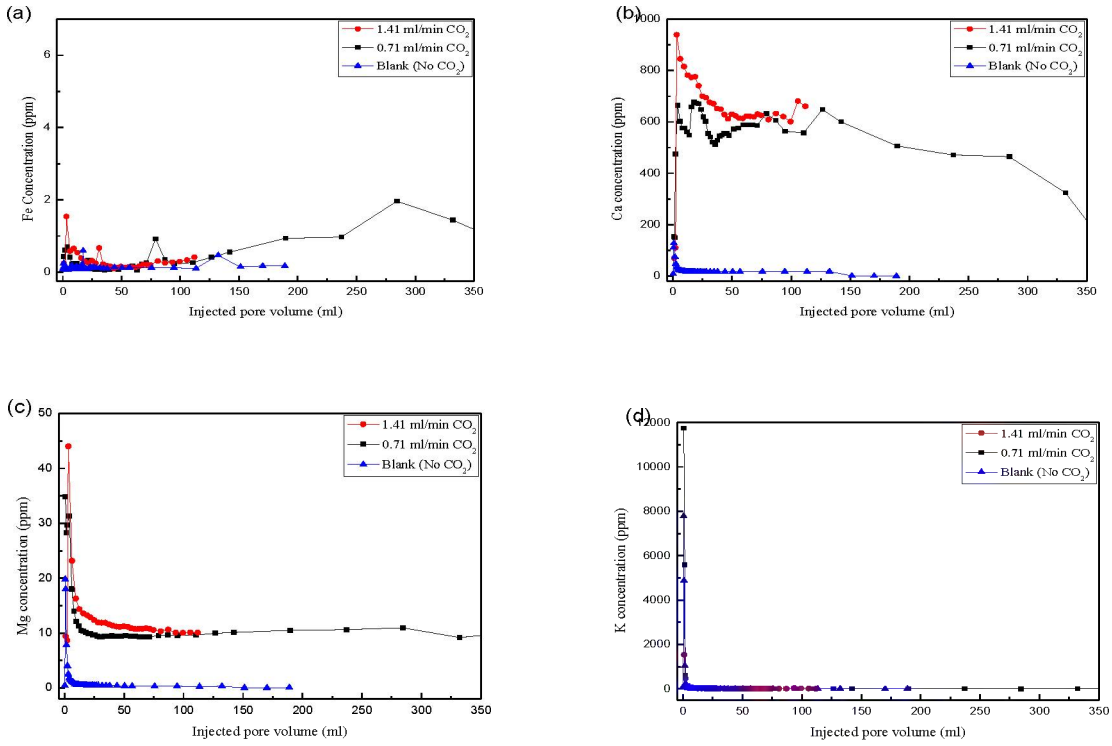

Figure 12. Concentration of iron, calcium, magnesium, and potassium ions as measured by ICP-MS in the effluent for limestone flooding experiments

In the limestone samples, the magnesium concentrations for both the low and high CO_2 flow rates remain quite similar throughout the first 36 hours (Figure 12(c)). As time progresses, the concentrations begin to approach a steady concentration with the concentration with the high CO_2 flow rate being only slightly above the magnesium concentration with the low CO_2 flow rate. The concentration of magnesium in the unreacted limestone sample was higher than that of the magnesium concentration in the unreacted sandstone sample. Figure 12(d) shows concentrations of potassium peak early in limestone floods as well, and decrease to low ppm values within 24 hours. The steady concentrations are attained more rapidly than in the sandstone floods.

Dolomite contains a significant amount of calcium and magnesium as a similar component ratio. Concentrations of iron, calcium, magnesium and potassium for dolomite are shown in Figures 13. The iron concentration in the dolomite effluent samples is similar when compared to the limestone effluent samples

(Figure 13(a)). Concentration differences of iron at the two different CO_2 flow rates look like significant, but actual value is a couple of ppm difference. It is because the dolomite core is mainly dolomite mineral ($CaMg(CO_3)_2$) based on the XRD analysis, and does not include a high percentage of iron based minerals.

Predictably, the calcium concentrations in the dolomite effluent samples are much higher (Figure 13(b)). The concentration of calcium increases rapidly with both the high CO_2 and low CO_2 flow rates. The experiment with high CO_2 flow rate was stopped after around 240 hours. This was due to excessive dissolution on bottom of the core at the core holder inlet similar to the limestone core flooding experiment. A pinhole was generated in the heat shrinking tubing similar to the pinhole generated in limestone, but unlike limestone, there was no wormhole created in the dolomite cores. The pinhole was possibly created due to the size of the pores on the exterior of the dolomite cores increasing the chances of a pinhole developing in the tubing. When comparing between low and high CO_2 flow rates, it is apparent that the higher CO_2 flow rate results in a large concentrations of calcium in the dolomite effluent samples. The higher CO_2 injection rate means that more fluid passes through the core facilitating greater reaction opportunity within the core. The concentration of calcium in the effluent is initially around 400 ppm but decreases to 300 ppm where it appears to be stable at higher CO_2 flow rate. At lower CO_2 flow rate, calcium concentrations begin slightly above 300 ppm then decreasing to just above 200 ppm where the concentration stabilizes. This result is similar to that of limestone, where the calcium concentration began high then decreased to a stabilized value. Also the concentrations of calcium in limestone and dolomite from the ICP-MS data are consistent with the XRD data such that limestone is almost completely comprised of calcium and the composition of dolomite is almost even values of calcium and magnesium. Therefore, the concentration of calcium in limestone is nearly double the concentration of calcium in the dolomite effluent samples.

The magnesium concentrations and calcium concentrations follow a similar trend (Figure 13(c)). The trend is that the concentration begins high and stabilizes to a lower value. The difference being the magnesium concentration is lower than the calcium concentration. This is because of the ratio of calcium and magnesium in dolomite. This result is consistent to the calcium and magnesium ratio from the XRD data. Concentrations of potassium peak early in dolomite effluent as well, and decrease to low ppm values within 24 hours (Figure 13(d)). The potassium concentrations are essentially the same in each of the effluent samples.

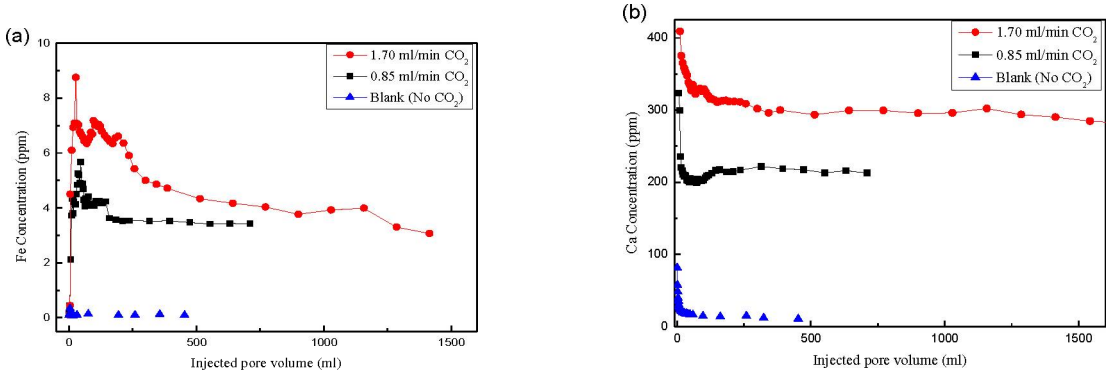

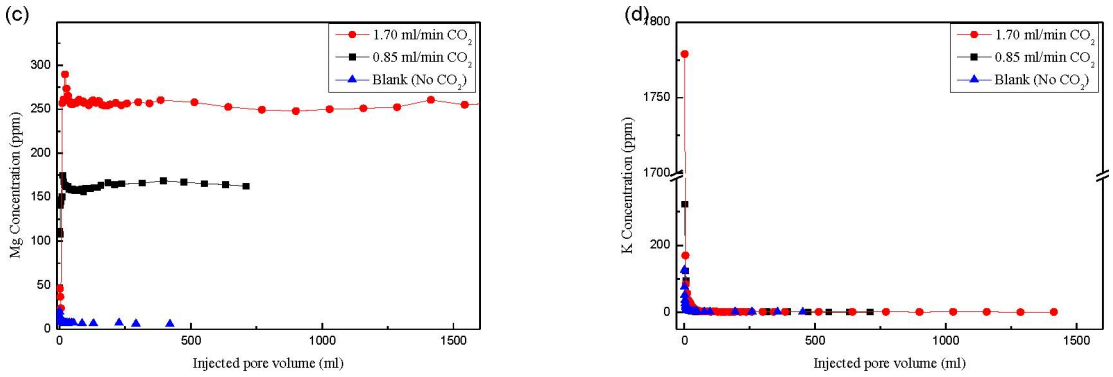

Figure 13. Concentration of iron, calcium, magnesium, and potassium ions as measured by ICP-MS in the effluent for dolomite flooding experiments

Higher CO_2 injection rates led to higher levels of mineral dissolutions. The cores were analyzed using XRD to measure the intensity of dominate minerals. In sandstone, quartz intensity showed a difference. However, in limestone and dolomite cores, there was not a noticeable intensity change. Dissolution of minerals was a significant result in the experiments based on the QEMSCAN data. Ankerite and siderite were the main iron bearing reactive minerals in sandstone and they dissolved almost completely in the two-week experiment. ICP-MS data showed effluent peaks of the key cations such as iron, calcium, and magnesium. The level of iron dissolution in sandstone – even over short durations was higher than expected – may have major implications in practical sequestration scenarios. As expected, calcite was mainly dissolved in limestone core and calcium and magnesium were dissolved from dolomite mineral in dolomite core. The dolomite mineral composition ratio was $(Ca_{0.6}Mg_{0.4})CO_3)_2$ based on the ICP-MS results.

Petrophysical changes in core flooding system

Core Analysis: Porosity Measurements

Originally, each of the sandstone, limestone, and dolomite cores measured 8 inch in length. However, the end of a 1 inch section of these cores was removed and both the top and bottom of this 1 inch section were made flat using a grinder. These 1 inch core sections were then analyzed using the helium porosimeter. The average porosity of the four sandstone, limestone, and dolomite core sections make up the "average porosity of unreacted sandstone, limestone, and dolomite," respectively.

The porosity measurements were made using the helium porosimeter described earlier. In general, each core section was measured for porosity five different times and the average porosity of each core section was then calculated. The average porosity values are stated as the porosities for pre reaction core samples.

After the core flooding experiments were completed, each of the four sandstone and five limestone, and three dolomite cores were then cut into seven equal sections each measuring under 1 inch. The top and bottom of each of the core sections were made flat using a grinder, with the exception of the inlet and outlet sides of the core. The porosity of each core section was then determined using the helium porosimeter. Before analysis in the helium porosimeter, the core sections were exposed to an air stream and lightly brushed (not including the inlet/outlet sides) in order to clear off excess dust and particles that resulted from using the grinder and saw.

Helium porosimeter data show the porosity change of the sandstone, limestone, and dolomite cores after core flooding experiments (Figures 14-16), respectively. Four core flooding experimental conditions were set up brine without CO_2, CO_2 only after saturating the core with brine, and brine and CO_2 flowing together. A higher porosity implies greater pore volume and thus a greater amount of mineral dissolution. After helium porosimeter analysis, brine without CO_2 and CO_2 only after saturating the core with brine showed no significant porosity changes. The experiments with brine and CO_2 flowing together showed much higher porosity changes. To compare the porosity change, the porosities of the seven 1 inch core sections was averaged and compared with the unreacted core porosity. In the core flooding experiments, there appears to be a porosity reduction in some sections of the cores followed by mild dissolution. This is believed to be due to two possibilities. One of the believed possibilities after the minerals partially dissolved and precipitated in sections. Izgec et al. also observed dissolution followed by precipitation in carbonates. The other possibility is rock heterogeneity.

Mineral dissolution appears during core flooding experiment with all different core samples (see Chapter 4). Also, in all cases, the porosity at the inlet is greater than the porosity at the outlet. This results shows that the reactivity is greater at the inlet due to the fresh brine and CO_2 solution continuously reacting with the core after that the mixing fluid has some reacted minerals proceeding up the core decreasing reactivity. Especially, dissolution does not significantly appear in sandstone under the brine without CO_2 and CO_2 only after saturating the core with brine conditions, 0.18 % and 0.12 %, respectively (Figure 14). When brine and CO_2 were injected together, the porosity change is greater than the previous conditions but only slightly: 0.60 % for 1.41 ml/min CO_2 flow rate and 1.01 % for 2.82 ml/min CO_2 flow rate. The greater porosity change under the higher CO_2 flow rate condition is consistent with the ICP-MS data results, showing more reactivity at higher CO_2 flow rates.

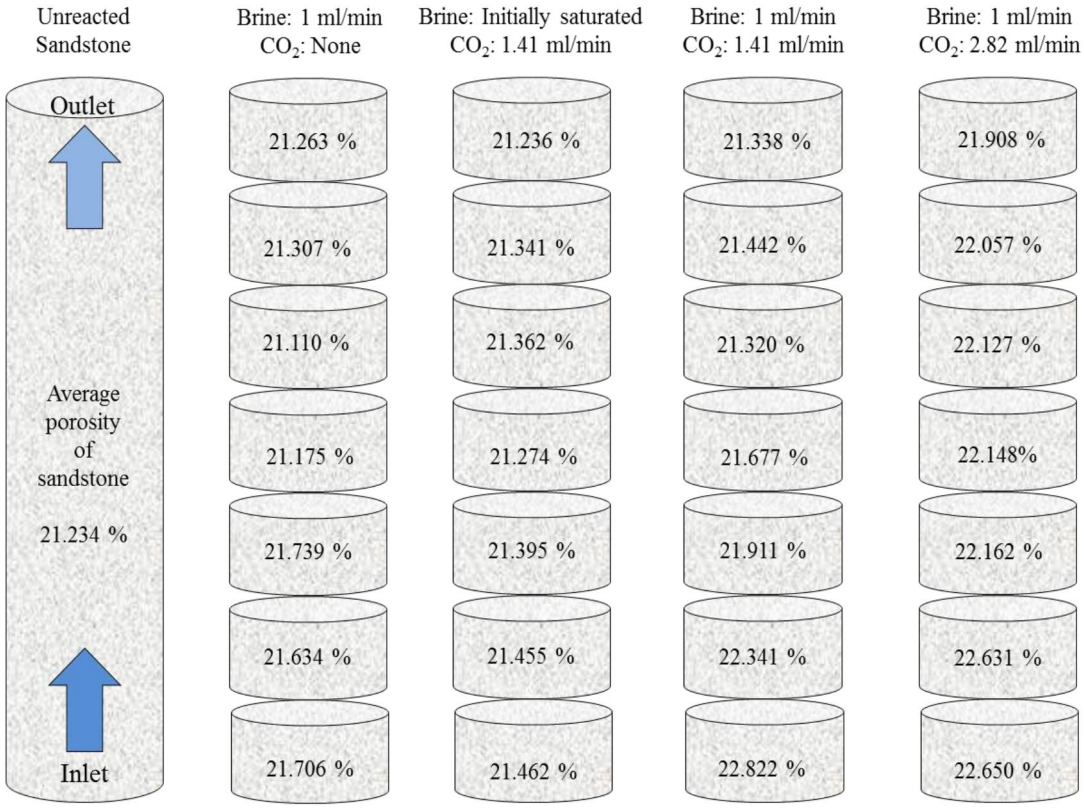

Figure 14. Porosity changes of different sections in sandstone using He porosimeter

In limestone, the porosity increase is consistent in all the experiments indicating the expected dissolution (Figure 15). Also, in all cases, the porosity at the inlet is greater than the porosity at the outlet as in the sandstone core samples. Little dissolution appears in limestone under the brine without CO_2 and CO_2 only after saturating the core with brine conditions, 0.70 % and 0.55 %, respectively. When different ratio of brine and CO_2 were injected together, the porosity change is much greater. When the injection rate of brine is 0.5 ml/min and CO_2 is 0.71 ml/min, the porosity change is 5.46 %. The high increase is due to the high dissolution in the bottom section of the core. As in the sandstone, the reactivity is much greater at the inlet and this section in the limestone was almost completely dissolved at this flow ratio. The residence time is increased at this flow ratio, therefore the fluid can react with the inlet section longer. When average core porosity is calculated without the bottom section, the porosity change is around 1.12 %. When the CO_2 injection rate is increased to 1.41 ml/min (brine remains at 0.5 ml/min), the porosity change is 1.59 %. Under these injection conditions, the inlet core section was also partially dissolved but not the extent of the previous core. When brine injection rate is increased to 1 ml/min (CO_2 remains at 1.41 ml/min), the porosity change is 2.79 %. Under these injection conditions, the residence time increases and the reactive fluid is able to penetrate up the core further causing a greater overall porosity change. With the comparison of the inlet sections, there is an increase in porosity change as the mixing flow rates decrease. This evidence shows that the increase in residence time with the inlet core section translates to a greater reactivity with this section as mixing flow rate decreases. These porosity changes correlate with the ICP-MS data results, showing more reactivity at higher brine and CO_2 flow rates.

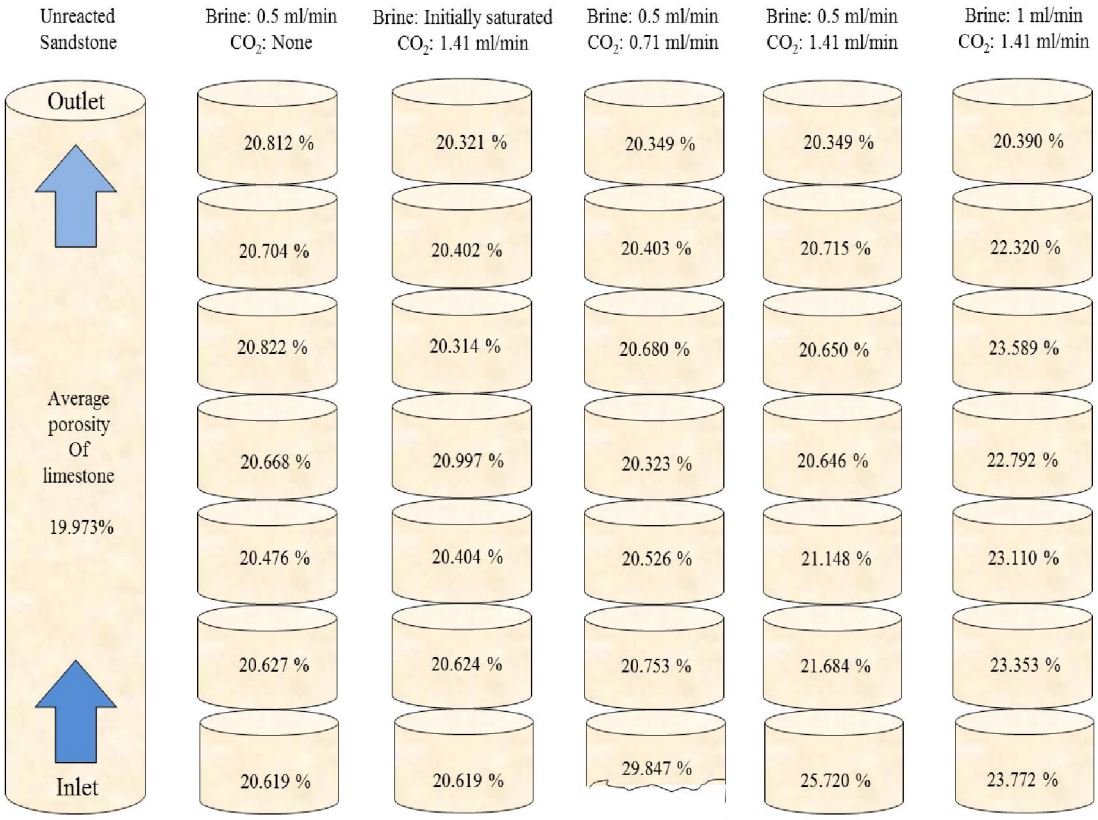

Figure 15. Porosity changes of different sections in limestone using He porosimeter

During preliminary experiments at the same injection conditions as the sandstone and limestone experiments, it was discovered that the core pressure nearly reached the pressure of the confining fluid. The increased pressure is caused by the low porosity within dolomite compared with sandstone and limestone. Due to safety issues, the experiments could not be run at these conditions; therefore, different injection conditions were selected. The injection rates selected go as followed: brine 0.6 ml/min for every experiment, CO_2 at 0 ml/min, 0.85 ml/min, and 1.70 ml/min. In the dolomite experiments, there is not a CO_2 only after saturating the core with brine result because a dolomite core with a consistent mineralogical composition was unavailable. In dolomite, in all cases, the porosity at the inlet is greater than the porosity at the outlet, like in the other two rock samples. The porosity increase is consistent in all the experiments indicated in Figure 16.

Dissolution does not significantly appear in dolomite under the brine without CO_2 condition; the porosity change is 0.42 %. When brine and CO_2 were injected together, the porosity change is greater than 1.58 % when the CO_2 flow rate is 0.85 ml/min and 2.52 % when the CO_2 flow rate is 1.70 ml/min. Similar to the limestone cores, the inlet sections of dolomite were also greatly dissolved. This dissolution is due to the rate at which the reactive fluid is passing through the core. As more fresh reactive fluid passes through the core section, more of that section is dissolved. The greater porosity change under the higher CO_2 flow rate condition is consistent with the ICP-MS data results, showing more reactivity at higher CO_2 flow rates.

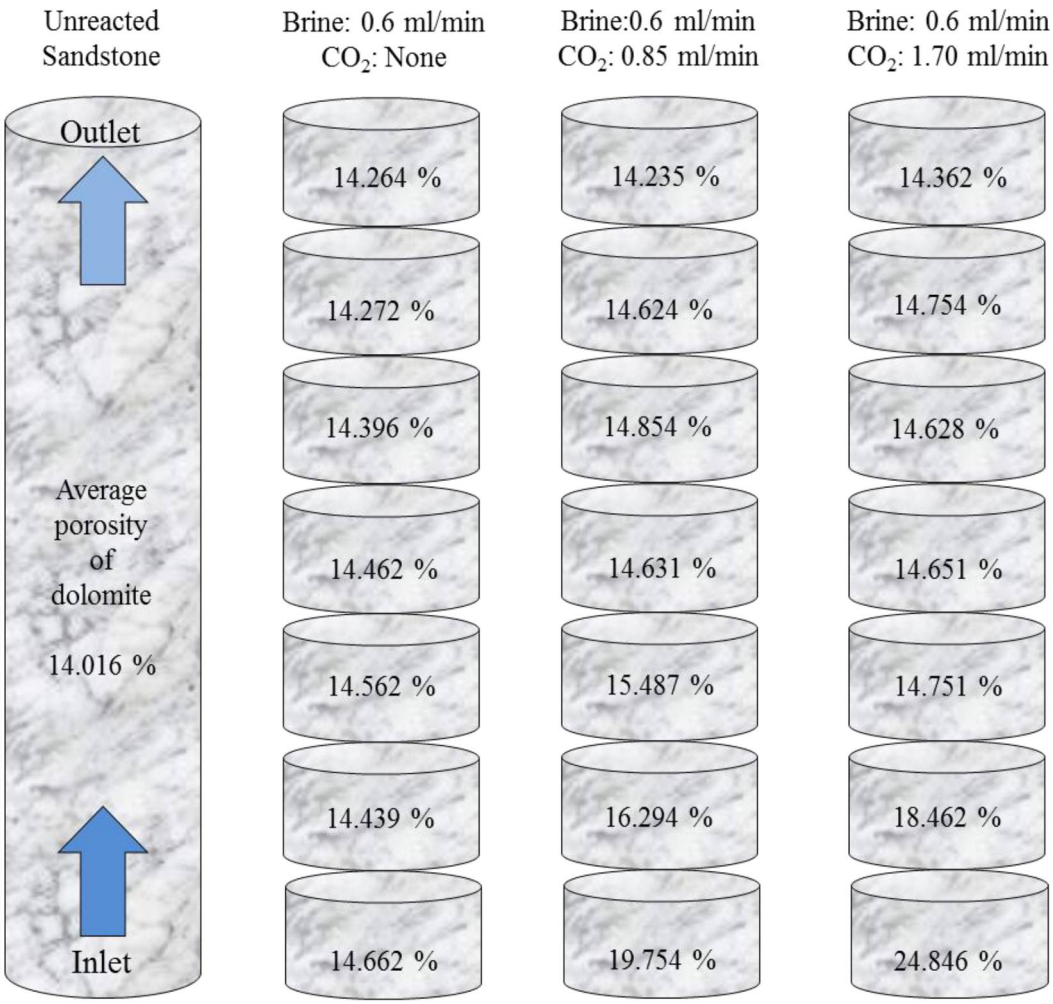

Figure 16. Porosity changes of different sections in dolomite using He porosimeter

Core Analysis: Permeability Calculation

Comprehensive fluid flow studies were conducted through a single fracture to investigate the validity of cubic law.[144] Idealized fracture models were constructed by assuming that the fracture planes had contact area and roughness. The flow in a fracture is usually characterized by the classical cubic law equation, equation (4).

$$Q = 5.11 \times 10^{6} \left[\frac{d\Delta P w^{3}}{L\mu}\right] \quad (4)$$

This equation neglects the matrix permeability compared to the fracture permeability. As a result, the classical cubic law does not account for any flow occurring through the matrix and assumes that the flow occurs entirely through the fracture. This assumption holds for low permeability reservoirs.

When fluid was injected through 7 inch in length different cores at fully saturated and at steady state conditions, pressure difference between injecting and producing ends is automatically recorded. According to Darcy's law, equation (5), permeability can be calculated by:

$$k_m = \frac{\mu Q L}{A \Delta P} \tag{5}$$

where μ is the viscosity of the fluid, Q is the volumetric flow rate of the fluid, L is the length of the core, A is the cross-sectional area, ΔP is the pressure difference between the inlet and outlet of the core. When water was injected through the fractured core, the average pressure difference due to the presence of fracture was obtained. According to Darcy's Law, average permeability in the fractured core can be calculated by, equation (6):

$$k_{avg} = \frac{\mu Q L}{A \Delta P_{avg}} \tag{6}$$

Table 2 shows the different core properties and the results obtained from experiments with different cores and the calculated permeability values, respectively. The viscosity of the fluid was assumed to be the same as pure water because the brine concentration was low. Matrix permeability was calculated using equation (6). The average differential pressure was calculated by averaging the differential pressure over each time step. The permeability changes are shown in Figures 17-19. Unreacted core permeability of sandstone, limestone, and dolomite is around 90 mD, 150 mD, and 25 mD, respectively. After the reaction, permeability changes in sandstone (Figure 17) are 0.21 % for the brine only experiment, 0.76 % for the 1 ml/min brine + 1.41 ml/min CO_2 experiment, and 1.43 % for the 1 ml/min brine + 2.82 ml/min CO_2 experiment. Permeability changes in limestone (Figure 18) are 1.06 % for the brine only experiment, 1.48 % for the 0.5 ml/min brine + 0.71 ml/min CO_2 experiment, 1.72 % for the 0.5 ml/min brine + 1.41 ml/min CO_2 experiment, and 3.42 % for the 1 ml/min brine + 1.41 ml/min CO_2 experiment. In the limestone experiments, a wormhole was generated causing the rapid increase in permeability over a short time period,

Table 2. Different core properties and experimental flow rate conditions

	Length	Diameter	Fluid
Sandstone	17.78 cm	3.81 cm	1 ml/min brine
Sandstone	17.79 cm	3.80 cm	1.41 ml/min CO_2 + 1 ml/min brine
Sandstone	17.78 cm	3.80 cm	2.82 ml/min CO_2 + 1 ml/min brine
Limestone	17.73 cm	3.80 cm	1 ml/min brine
Limestone	17.76 cm	3.82 cm	0.71 ml/min CO_2 + 0.5 ml/min brine
Limestone	17.77 cm	3.81 cm	1.41 ml/min CO_2 + 0.5 ml/min brine
Limestone	17.74 cm	3.81 cm	1.41 ml/min CO_2 + 1 ml/min brine
Dolomite	17.83 cm	3.81 cm	0.6 ml/min brine
Dolomite	17.86 cm	3.81 cm	0.85 ml/min CO_2 + 0.6 ml/min brine
Dolomite	17.82 cm	3.81 cm	1.70 ml/min CO_2 + 0.6 ml/min brine

less than 3 days. Permeability changes in dolomite (Figure 19) are 0.51 % for the brine only experiment, 1.69 % for the 0.6 ml/min brine + 0.85 ml/min CO_2 experiment, and 2.41 % for the 0.6 ml/min brine + 1.70 ml/min CO_2 experiment.

Core Analysis: Micro-CT Imaging

Analysis via Micro-CT was performed on the unreacted and reacted 7 inch in length limestone cores, but not for the 7 inch in length sandstone and dolomite cores. The Micro-CT machine was only capable of supplying the necessary amount of energy to penetrate the limestone cores with a 42 micron resolution. The energy required to penetrate the sandstone and dolomite cores was too great and thus could not be accomplished within a reasonable resolution. Four different scans of each core were taken - inlet, outlet, and two in between. Due to the angle limitations of the scanning device, a continuous scan of the entire core was not possible and small gap exists between each scanned section. The angle limitation also results in a distorted image on both ends of the scan due to the lower energy exhibited at both of the extremes of the angle range. Most of these distortions are not displayed for simplicity; however, the effect can be seen at both ends of each scan as per the rounded edges and solid coloring. The four different scans were taken at the same location for each reacted and unreacted core. The images have been displayed so as to properly see the porosity of each core section. Micro-CT scans a surface generating a 2D raw image. The 2D raw images from Micro-CT were very dark and difficult to interpret. The brightness quality of the 2D raw images was improved using MIPAV software. After brightness was improved in all the images, they became much easier to interpret. Nothing more was altered other than the brightness of the images. The enhanced 2D images were then stacked on top of each other in order to generate a 3D image using different software called Drishti v2.4. Micro-CT detects the solid portions of each surface, but in the core flooding experiments, the dissolved portions are of more interest. Therefore, using Drishti v2.4 again, a negative image was created in order to show the portions of the limestone that were dissolved. The negative image was created by changing the settings to display the solid portions of the core as vacant, and the vacant core sections to display a solid.

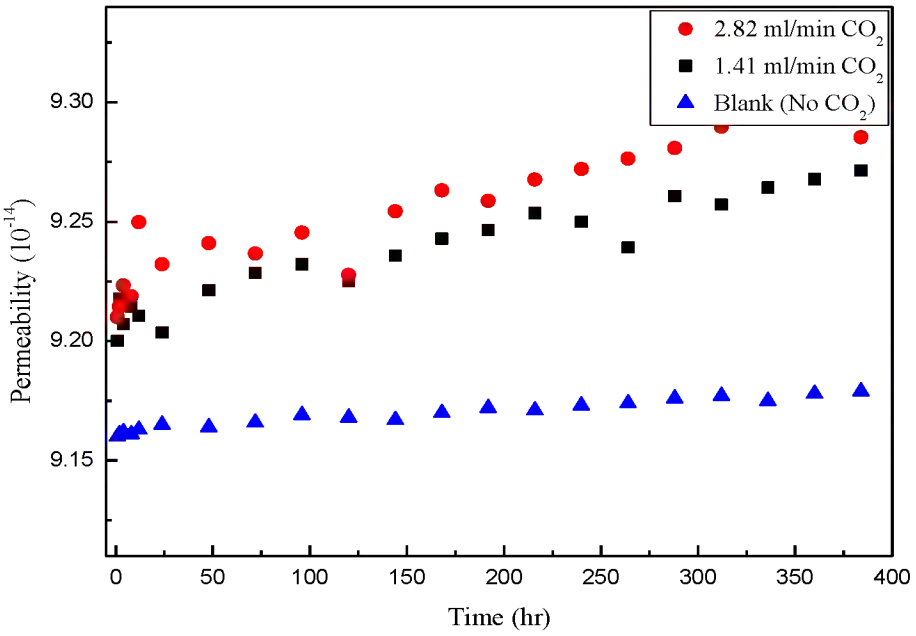

Figure 17. Permeability change in sandstone at different experimental conditions

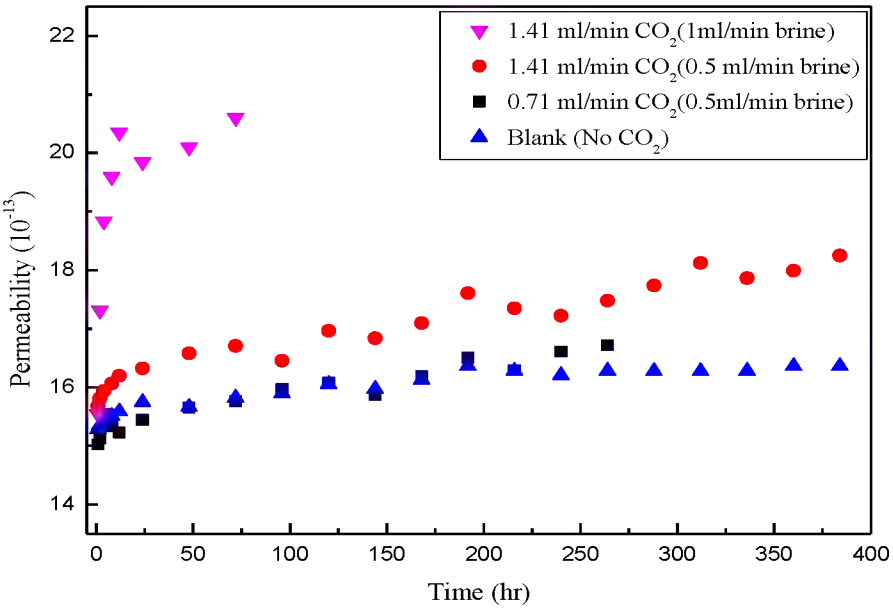

Figure 18. Permeability change in limestone at different experimental conditions

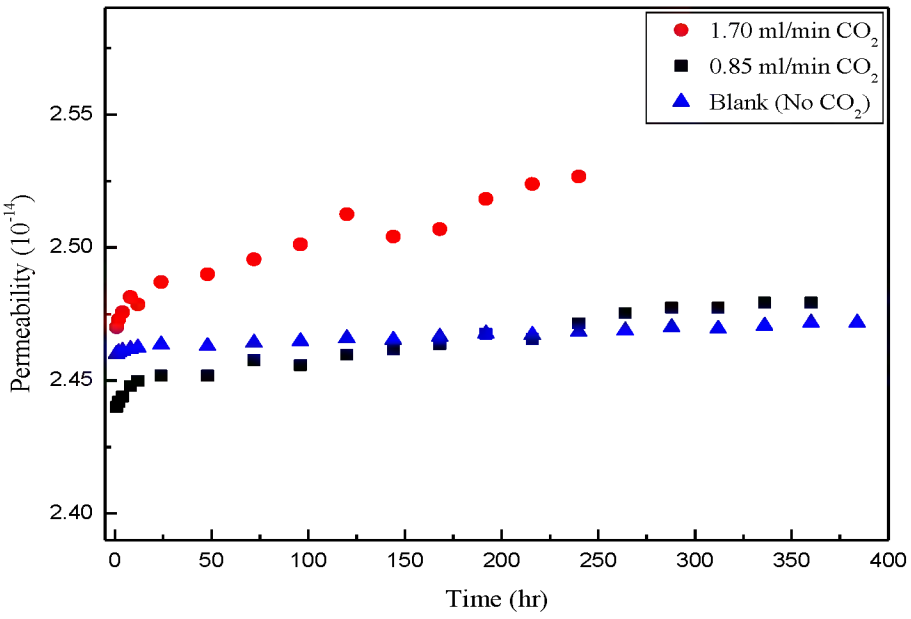

Figure 19. Permeability change in dolomite at different experimental conditions

Micro-CT images of limestone pre- and post-flood samples with different flow conditions are shown in Figures 20. In preliminary testing, a limestone core was flooded with 1.41 ml/min of CO_2 and 1.0 ml/min of brine in order to match the flow rate of the sandstone experiment. However, this resulted in wormhole generation within the limestone core after about two days, ending the experiment. The Micro-CT results of the unreacted and reacted cores in Figure 20(e) show the wormhole generation in the first and third sections and an expansion of the pre-existing wormhole in the second section. It was determined that in order to prevent such a rapid development of a wormhole, the overall flow rate would need to be decreased. Thus, the flow rate of brine was reduced to 0 ml/min and 0.5 ml/min for brine, and 0.71 ml/min and 1.41 ml/min for CO_2.

It is observed that the pore morphology is practically unchanged for the experimental runs with only brine and with CO_2 only with the core initially saturated with brine (Figure 20(a) and (b)). Notice that the pore density is uniform throughout the core sections. Dissolution porosity is apparent in Figure 20(c) - the experiment conducted at low flow rates. Dissolution patterns and beginnings of the generation of wormhole type structures are evident for the experiment at the higher CO_2 flow rate (Figure 20(d)). And finally, Figure 20(e) shows a fully developed wormhole. The existence of a small wormhole in the second core section obviously affected the growth of the wormhole in that section. Channeling of the CO_2-brine mixture through that section possibly resulted in the creation or acceleration of a wormhole in the first part of the core as well. The different flow rates show development in the dissolution of limestone. A low CO_2 flow rate demonstrated complete dissolution at the inlet, a high CO_2 flow rate demonstrated moderate dissolution at the inlet and a developing wormhole-like structure, and high CO_2 and brine flow rates demonstrated only a wormhole structure.

In analyzing the Micro-CT images, it can be seen that there is a general trend of increasing porosity between unreacted and reacted cores. The qualitative results of the Micro-CT are also consistent with the quantitative results of the helium porosimeter. Both Micro-CT results and helium porosimeter results show that the porosity is the greatest at the inlet and decreases as the distance from the inlet increases.

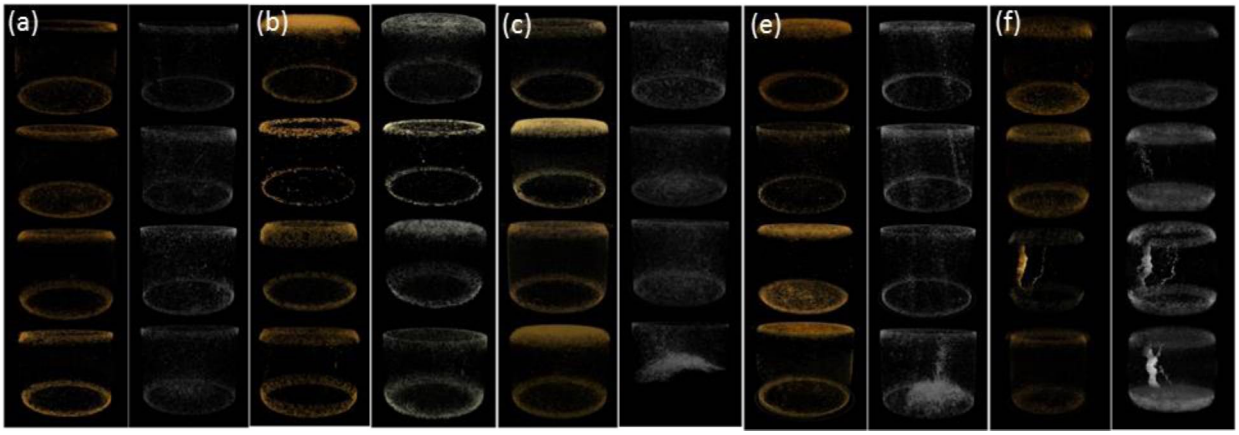

Figure 20. The image of different sections of a Limestone core using Micro-CT pre- and post- 2% NaCl brine and supercritical CO_2 experiments using the core flooding system (a) 0.5ml/min brine only, (b) initially saturate brine + 0.71 ml/min CO_2 (c) 0.5ml/min brine + 0.71 ml/min CO_2, (d) 0.5ml/min brine + 1.41ml/min CO_2, and (e) 1ml/min brine + 1.41ml/min CO_2

Mineralogical changes in batch reactor system

Reaction Pressure

The initial batch reactor pressures were determined to be around 830-840 psi. After the reactors were filled with CO_2, the batch reactors were placed in the oven at 60 °C. Upon being inserted into the oven, the pressure of the reactors gradually rises until reaching target pressure around 2400 psi. The batch reactor experiments were successively completed for a two-week period. The pressure was recorded throughout the two-week period in order to detect drastic changes in pressure. If the pressure of any one reactor fell below the 2000 psi mark, it would then be removed from the oven, cooled to room temperature, refilled with CO_2, and reinserted into the oven.

Table 3 shows the pressure of each batch reactor on each day of the experiment. Notice the gradual decrease in pressure over the initial couple of days. This pressure drop is likely due to the CO_2 being dissolved in the brine and reaching equilibrium. After the first few days, the pressure continued to slowly decrease; this pressure drop is due to the mineralogical reactions with carbonate taking place. When the pressure leakage happened very rarely, the reactor was refilled with CO_2 again. The target pressure was tried to match when the reactor was removed. Sometimes, the pressure was stable or increased compared with previous dates; possible discrepancies are the temperature fluctuation within the oven and the pressure gauges used are not digital and subject to reading error.

Table 3. The reactor pressure profiles according to different sample types and forms

Core plug samples	Initial	1st	2nd	3rd	4th	5th	6th	7th	8th	9th	10th	11th	12th	13th	14th
Blank	842	2450	2400	2370	2350	2350	2350	2350	2350	2350	2300	2350	2350	2350	2350
Sandstone	830	2340	2320	2300	2300	2280	2280	2250	2250	2240	2240	2220	2200	2200	2200
Limestone	833	2350	2300	2300	2300	2280	2250	2250	2250	2200	2180	2150	2100	2080	2080
Dolomite	835	2400	2350	2350	2360	2320	2300	2300	2300	2300	2300	2300	2320	2300	2300
Fracture samples	Initial	1st	2nd	3rd	4th	5th	6th	7th	8th	9th	10th	11th	12th	13th	14th
Blank	840	2450	2400	2380	2360	2360	2360	2350	2350	2350	2300	2350	2350	2350	2350
Sandstone	834	2400	2350	2350	2300	2300	2300	2280	2250	2250	2240	2220	2200	2180	2150
Limestone	832	2350	2300	2300	2250	2250	2250	2250	2240	2240	2220	2220	2200	2200	2200
Dolomite	836	2400	2350	2350	2350	2330	2320	2320	2300	2300	2280	2280	2260	2260	2250
Powder samples	Initial	1st	2nd	3rd	4th	5th	6th	7th	8th	9th	10th	11th	12th	13th	14th
Blank	841	2450	2400	2380	2380	2360	2360	2360	2350	2350	2300	2350	2350	2350	2340
Sandstone	836	2420	2400	2350	2300	2280	2280	2250	2250	2240	2230	2200	2180	2160	2150
Limestone	832	2350	2300	2250	2250	2200	2200	2150	2140	2140	2120	2100	2100	2050	2050
Dolomite	831	2350	2300	2300	2280	2260	2250	2250	2220	2220	2200	2200	2280	2260	2250

Mineralogy Changes: ICP-MS

Before studying effects of different surface area of core (different forms), mineral dissolution patterns were determined and plotted by cation concentration over time (Figure 21).

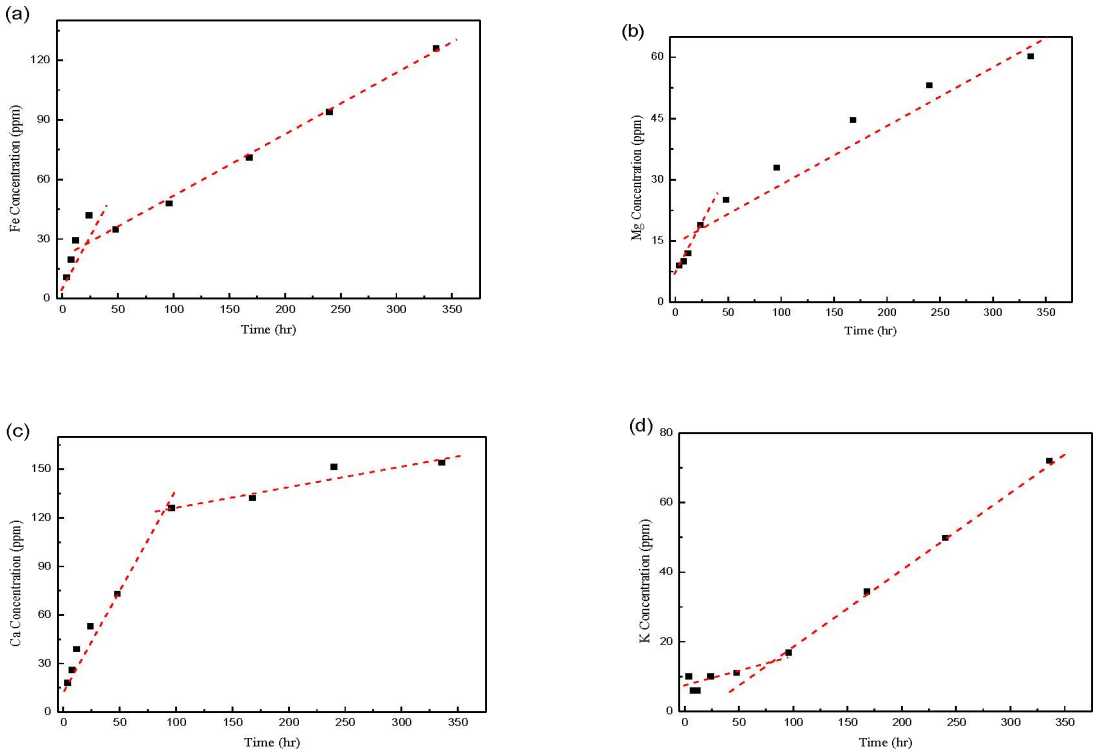

Figure 21. Concentration of iron, magnesium, calcium, and potassium ions as measured by ICP-MS in the effluent for sandstone time step batch experiments

Iron (Figure 21(a)) and magnesium (Figure 21(b)) concentrations before 48 hours and after 48 hours show different dissolution rates; this is believed to be caused by the rapid dissolution of ankerite minerals. In the iron case, siderite mineral dissolution also affects the iron concentration profile by the slow dissolution rate, as in the core flooding experiments. The calcium concentration profile (Figure 21(c)) is similar to that of iron and magnesium, but the profile change did not occur until 96 hours. The extended time of rapid dissolution is caused by simultaneous dissolution ankerite and calcite minerals. The slow concentration change after 96 hours is believed to be the dissolution of remaining calcium containing minerals. The potassium concentration profile (Figure 21(d)) shows a completely different pattern. In these sandstone samples, illite is the only possible potassium containing mineral. As was also found in the core flooding experiments, the potassium ion concentration profile is also very different than the other elemental profiles.

Mineralogy Changes by Different Surface Area: ICP-MS

Upon completion of the experiment, each of the collected fluids was analyzed using ICP-MS. The data set is shown in Table 4. For most of the experiments, there was little change in the concentration of sodium from the relatively high values, because of the 2% NaCl brine. The concentrations of sodium in each sample were slightly different although the same concentration of brine was used. The error range is less than 5% which is acceptable for these experiments.

These results are likely related to operational error, such as dilution, and other contaminants. In the blank test, the concentrations of minerals such as magnesium, aluminum, and iron throughout the experiment were slightly over the ICP-MS detection limit. This suggests some possible evidence for reactor corrosion. To minimize the reactor corrosion effect, the reactors were replaced after a couple experiments.

Based on Table 4, most of elements concentrations are increased, when surface area of the sample is increased matching the purposed hypothesis, which is that mineral reactivity is affected by surface area changes. Magnesium exhibits a trend of increasing concentration as the surface area of the sample is increased. This is especially true in the case of sandstone and dolomite, but the effect is less in that of limestone. Illite and ankerite dissolution would be the source of the magnesium concentration increase in sandstone; in dolomite, magnesium is one of the main elements in the dolomite mineral and the obvious cause of the magnesium concentration increase. In limestone, there are very few minor minerals containing magnesium. This magnesium concentration change is consistent with the core flooding experiment results.

Aluminum and silica did not display a significant change in concentration in the limestone and dolomite core forms (core plug, fractured, powder). In these two rocks, minerals containing aluminum and silica are present in small quantities and are primarily unreactive. In sandstone, there is a large concentration difference in aluminum concentration when compared with limestone and dolomite, especially in powder samples. Two possible sources of silica are quartz and illite. Quartz is unreactive with the CO_2 and brine solution; therefore, illite would be the primary source of silica in the effluent. Potassium similarly shows little changes by the different forms during the experiment. The concentrations are also relatively similar in each rock type (sandstone, limestone, and dolomite).

Table 4. ICP-MS results for core plug, fractured core, and powdered core after two-week batch experiment at 60 °C and over 2000 psi

	Na (mg/kg)	Mg (mg/kg)	Al (mg/kg)	Si (mg/kg)	K (mg/kg)	Ca (mg/kg)	Fe (mg/kg)
LoD	2	0.004	0.06	0.06	7	13	0.05
Core plug samples							
Blank	7024	0.68	0.64	0.22	<7	<13	1.92
Sandstone	7108	60.2	27.2	3.8	72	154	126
Limestone	7024	24	2.43	1.16	64	571	0.08
Dolomite	7188	302	0.87	5.04	80	428	0.08
Fracture samples							
Blank	7096	0.82	<0.06	0.25	<9	<13	1.14
Sandstone	7103	109	64.9	8.4	140	204	192.1
Limestone	7028	29	1.39	3.07	96	708	0.07
Dolomite	7097	444	0.15	2.37	137	543	0.08
Powder samples							
Blank	7018	0.74	0.32	1.68	<4	<13	1.53
Sandstone	6904	167.2	98.5	17.2	211	384	271.44
Limestone	7103	28.4	1.32	2.32	163	1226	0.07
Dolomite	7062	705	0.36	8.46	190	960	0.06

Calcium has the same trend, in that it tends to increase with surface area. Dolomite and limestone show the greatest changes. The main minerals found in limestone and dolomite are primarily made up of calcium. Sandstone shows relatively small changes in calcium concentration. The main reactive mineral containing calcium in sandstone is ankerite which is found at a low concentration. The concentration of iron in each of the reactors seems to be consistent with the concentrations of iron in the dolomite and limestone samples. However, iron concentration in sandstone is quite interesting. Each of the samples with sandstone results in large concentrations of iron, indicating dissolution of iron containing minerals. Based on the core flooding experimental results and simulation, these minerals are mainly ankerite and siderite. However, the dolomite and limestone samples show comparatively low amounts of iron concentration. The total mineralogical changes in the batch experiments are lower than those found in the core flooding experiments and simulation results. In the core flooding experiments, reactive fluid was continuous injected. However, in batch experiments, the rock samples were contained in the same fluid over the two-week period. The different fluid conditions caused different dissolved element concentrations.

Mineralogy Changes by Different Surface Area: QEMSCAN

QEMSCAN was used to obtain better understanding of mineralogical change in the batch experiments with different core plugs as was done for the core flooding experiments. The QEMSCAN images of unreacted and reacted different core plugs are presented in Figures 22-24. The QEMSCAN analysis confirmed that calcite, dolomite, and quartz were the dominant minerals in the rocks, with minor amounts of alkali feldspar, illite, plagioclase, kaolinite, and other lower amounts of various minerals.

Figure 22(left) shows the surface image and the mineralogical composition of the unreacted sandstone core plug. Quartz is the main mineral with a composition around 77.83 % by area. Illite is the second most dominant at 5.74 % by area. After the two-week batch experiment, Figure 22(right) shows the image and mineralogical composition of the reacted sandstone core plug. The two most dominant mineral compositions are compared, quartz concentration increased to 84.50 % by area, and illite concentration decreased to 3.84 % by area relatively. The reactive minerals like illite dissolved during the batch experiment causing unreactive mineral concentration such as quartz to increase, confirming the XRD observation. Also, the background surface area is increased meaning the porosity has increased.

Figure 23(left) shows the surface image and the mineralogical composition of the unreacted limestone core plug. Calcite is the main mineral with a composition around 99.08 % by area. After the two-week batch experiment, Figure 23(right) shows the image and mineralogical composition of the reacted limestone core plug. Calcite concentration did not changed significantly, less than 0.3 %; the reacted calcite concentration is 98.80 % by area. QEMSCAN uses mineralogical surface percentages based on relative amounts of minerals on the sample. In the case of limestone, although, calcite is dissolved it still remains in high percent (nearly 100 %) relative to the other minerals, but the background area percentage has significantly increased from 14.58 % to 23.54 %. Based on the background area percentage increase, it concluded calcite has dissolved. Figure 24(left) and (right) show the unreacted and reacted dolomite core plug, respectively. The result is very similar to the limestone result and the background area percentage change is what shows that dolomite has dissolved. The background area percent changed from 12.91 % to 15.07 %. When compared, limestone and dolomite surface area percentage limestone (Calcite) is more reacted with CO_2 and brine than dolomite.

Comparison of the XRD and QEMSCAN data indicates broad agreement between the two techniques because of differences in sampling location (i.e., the analyses are collected on adjacent rock surfaces but are still not exactly the same piece of material). In both QEMSCAN and XRD analysis, the mineralogical percentages are based on relative amounts of each mineral in the sample. This makes comparing absolute mineralogical amounts between samples and analytical methods difficult. In addition, the QEMSCAN percentages are based on a surface area, whereas, XRD represents volumetric mass fractions, and the analytical techniques are different.

The QEMSCAN images also show the pore surface area (background area) of the samples. This surface area is represented as the background in the images. Due to the 2D nature of the images, the pore surface area is approximated as the area of the blank regions of the sample image. These surface area approximations can be loosely compared with the surface area results from the BET analysis.

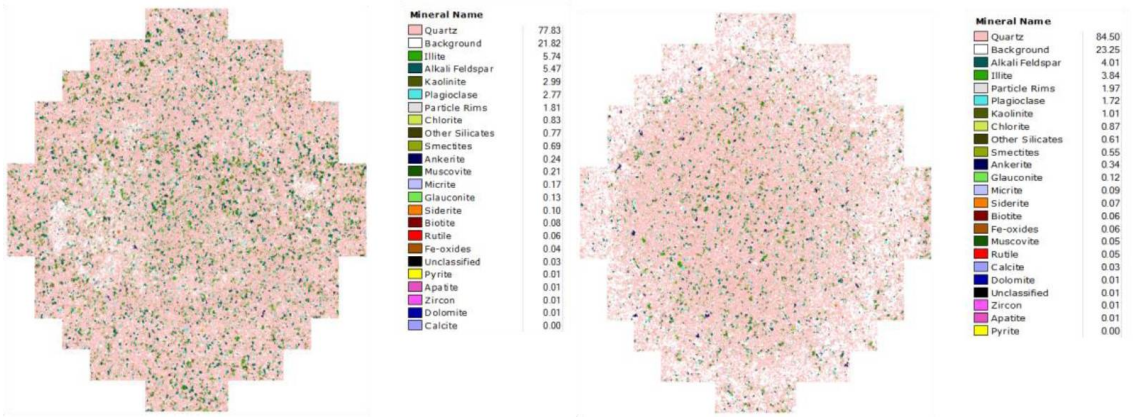

Figure 22. QEMSCAN result of unreacted and reacted sandstone core plug

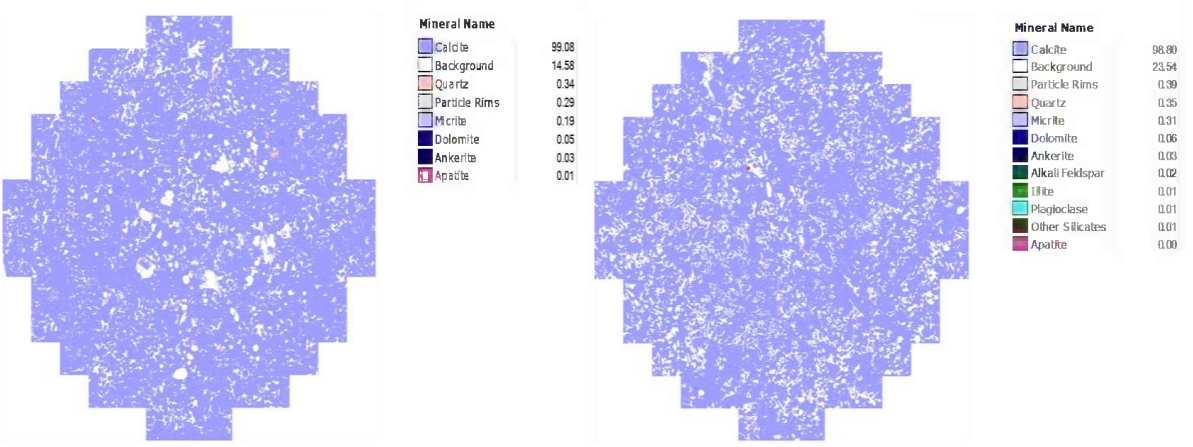

Figure 23. QEMSCAN result of unreacted and reacted limestone core plug

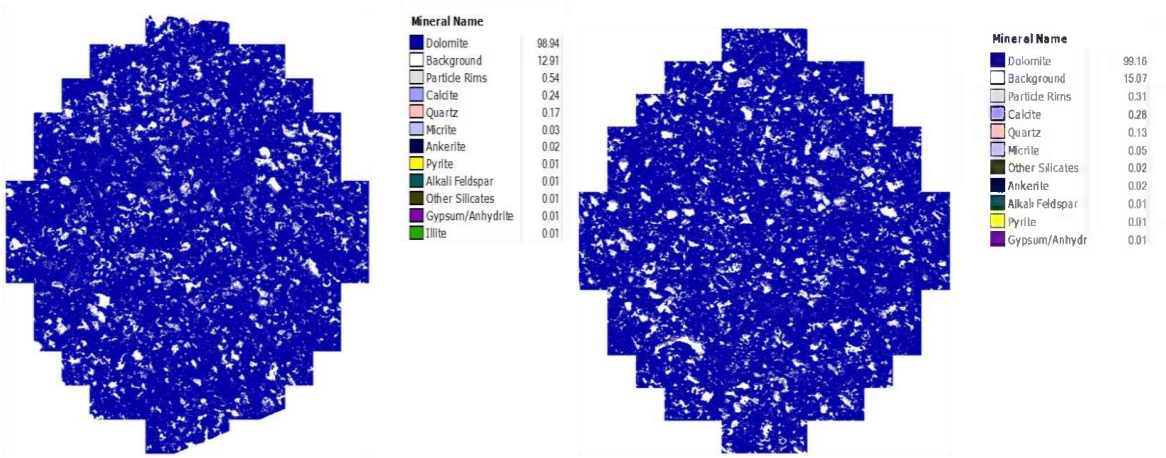

Figure 24. QEMSCAN result of unreacted and reacted dolomite core plug

Petrophysical changes in batch reactor system

Core Analysis: Micro-CT Imaging

Analysis via Micro-CT was performed on the unreacted and reacted sandstone, limestone, and dolomite core plugs samples only (1/2 inch in length and 3/8 inch in diameter), but not for fracture and powder samples. The Micro-CT machine was capable of supplying the necessary amount of energy to penetrate all the core plugs with a 1.85 micron resolution which was impossible for all the 7 inch cores. The three different core plug scans were taken at the same location for each unreacted and reacted core plugs. Figures 25-27 show the Micro-CT images of sandstone, limestone, and dolomite. Again, by converting to a negative image and showing the void portion of each core plug, the reactivity of each core sample is more readily determined. Figures 25-27 shows a cross section, a solid portion, and a void portion of the unreacted and reacted sandstone, limestone, and dolomite core plugs. Notice the definite porosity change at the circled sections, indicating mineral dissolution within the core. In the cross section 2D images, the spots marked by A, B, and C indicate specific spots on the surface. These markers do not have any other purpose other than to indicate the same spots on the unreacted and reacted surface images.

Figure 25 shows the Micro-CT images for sandstone. In the cross-sectional 2D images, the porosity change is easily recognized in the circle area. In the 3D solid image, it is difficult to see mineral dissolution; the images show some differences, but it is hard to see what happened. The 3D negative image shows more clearly the dissolution of minerals within the sandstone core plug, but it is impossible to determine which minerals are dissolved. Based on the previous experiments, the dissolved mineral is thought to be ankerite or reactive clay minerals.

In limestone, Figure 26, the cross-sectional 2D images, the porosity change is easily recognized in the circle area. The reaction expanded the pore size of already existent pores. In the 3D solid image, there are many pore changes on the surface of the core plug, indicating mineral dissolution on the surface. The negative 3D image is cloudier after the reaction, which was also shown in the 7 inch length limestone sample used in the core flooding experiment. The images from the batch experiments are much different than the images from the core flooding experiments. In the batch experiments, the fluid penetration is all particle diffusion, but in core flooding, there is flow through the core. The flow through the core caused mineral dissolution to occur in the core at a much higher reaction rate than in the batch experiments.

Figure 27 shows the dolomite Micro-CT images. In the cross section 2D image, it is hard to detect any porosity change. It is believed that the permeability is much lower than that of sandstone and limestone. Therefore, the fluid does not penetrate the inside of the core as easily. The solid 3D image shows that the surface of the dolomite core plug is dissolved. The 3D negative image shows mineral dissolution on the surfaces of the core plug.

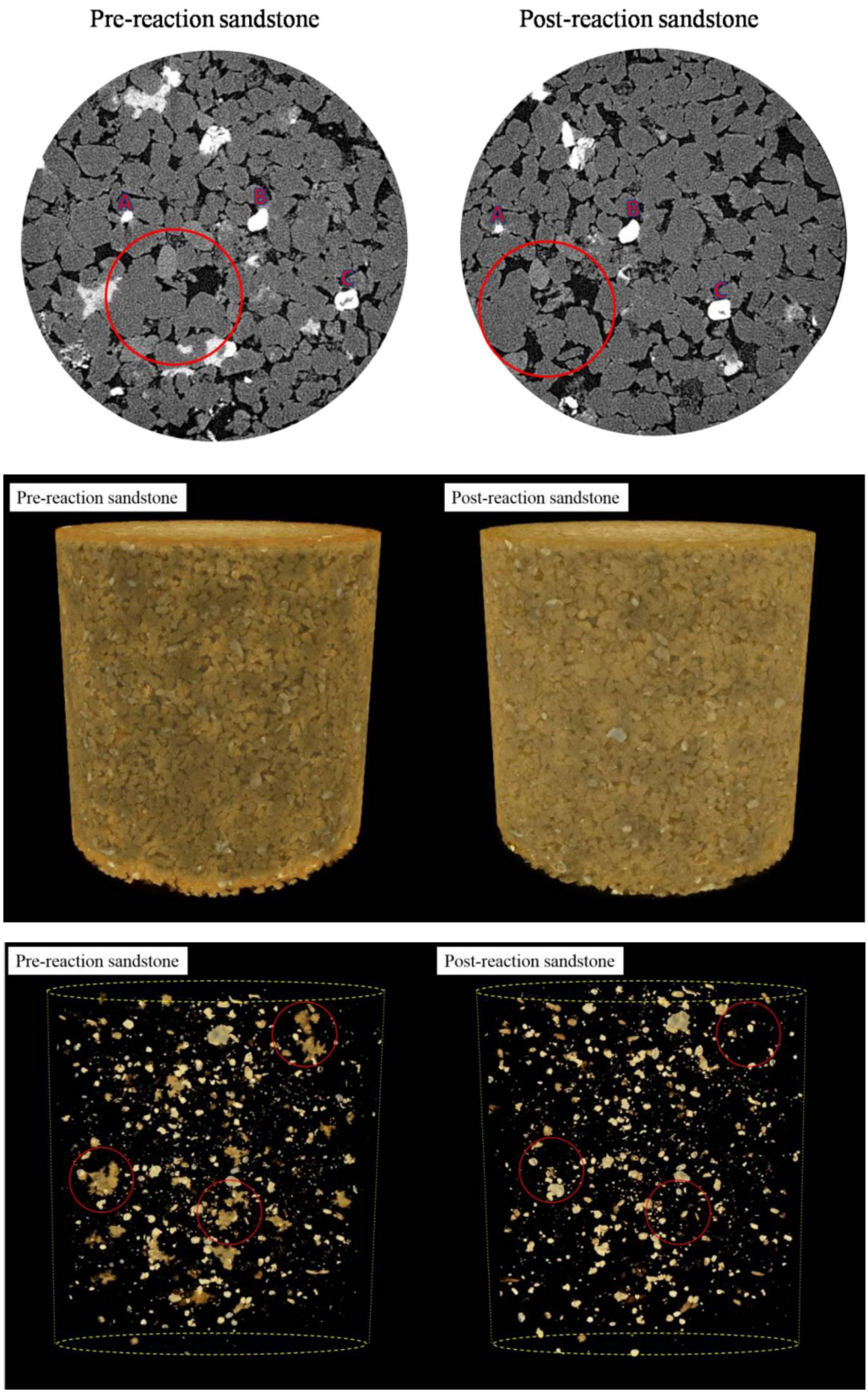

Figure 25. Micro-CT images of sandstone pre- and post-reaction in a batch reactor system

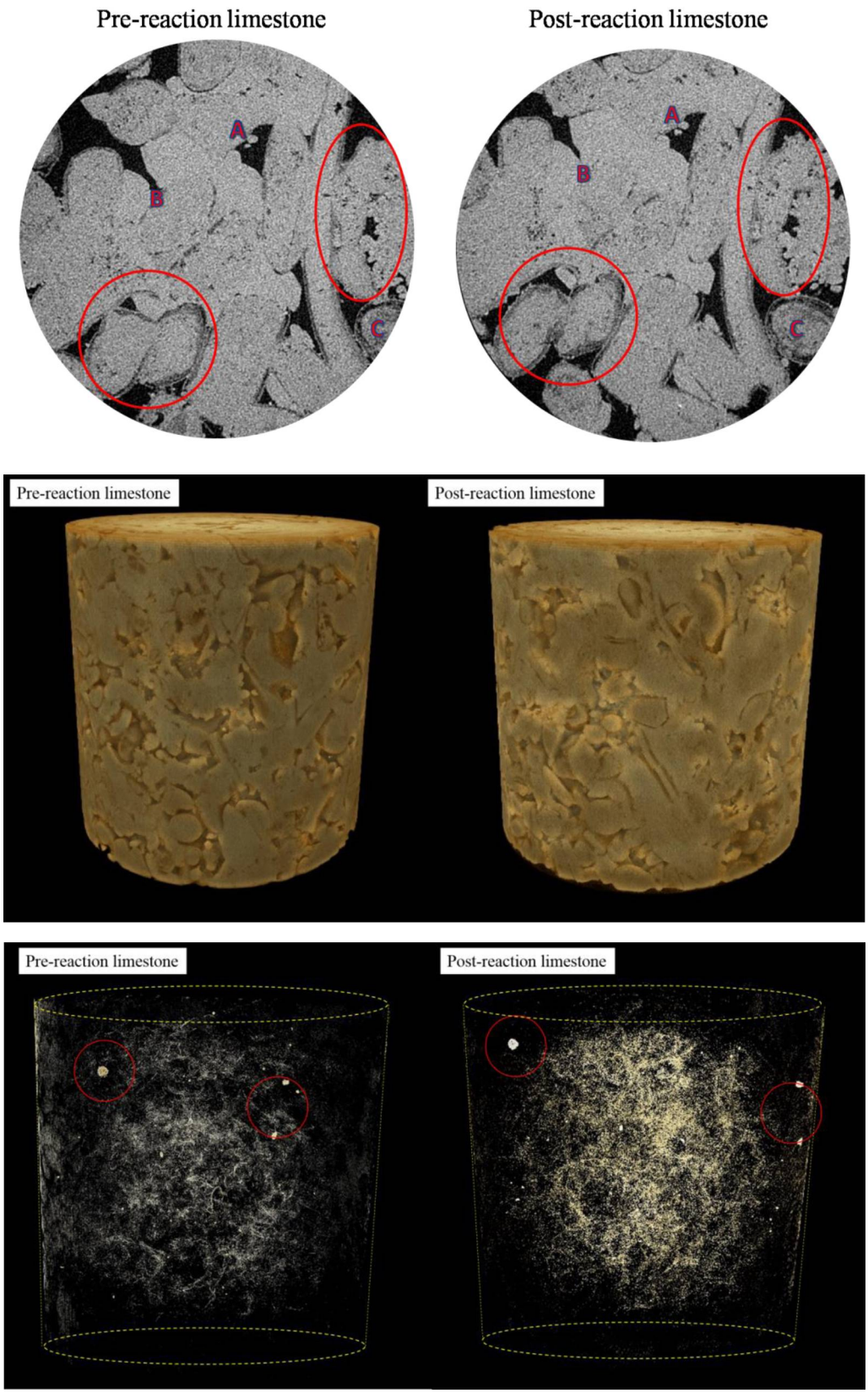

Figure 26. Micro-CT images of limestone pre- and post-reaction in a batch reactor system

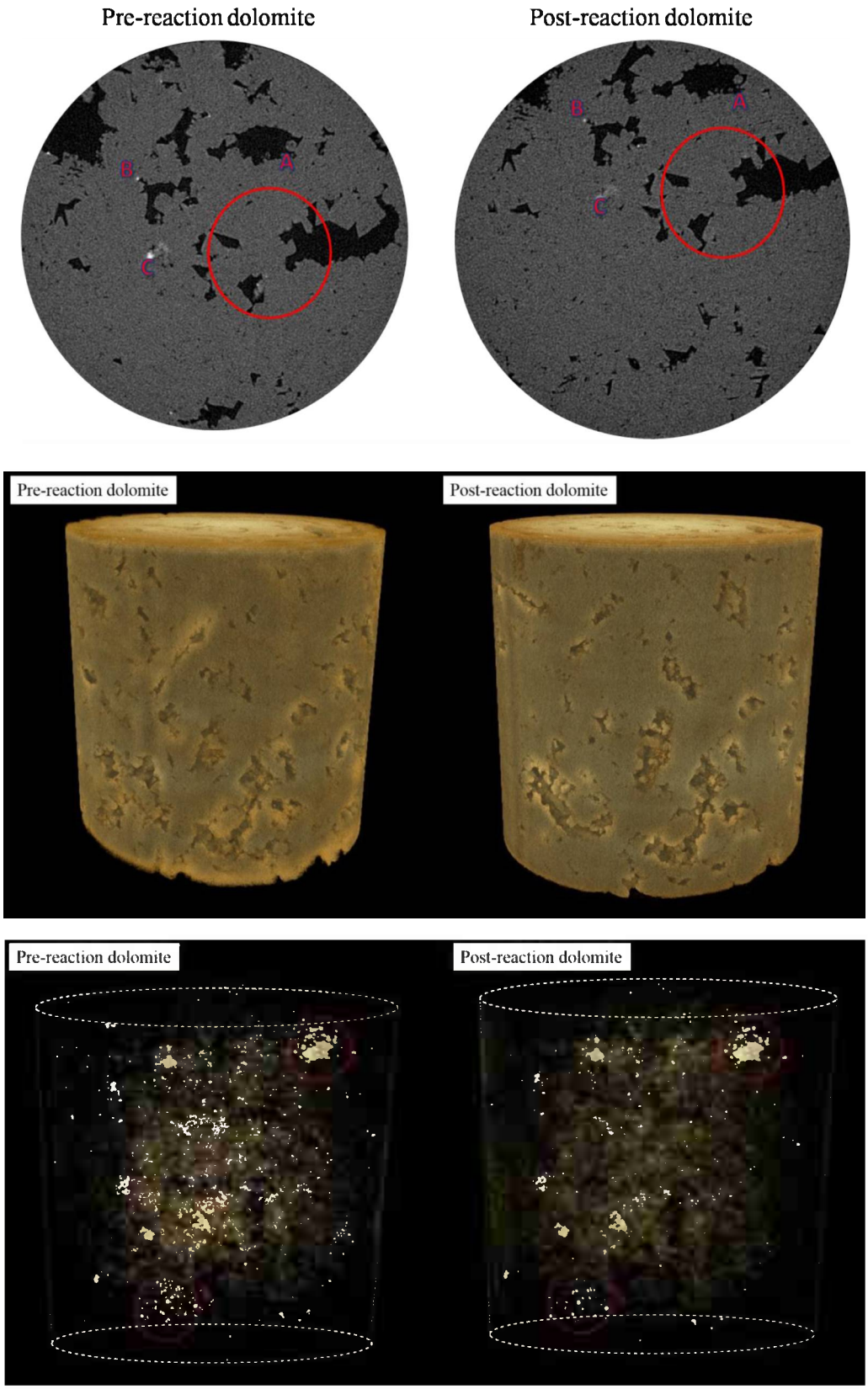

Figure 27. Micro-CT images of dolomite pre- and post-reaction in a batch reactor system

Core Analysis: Surface Area and Pore Volume

In the post-experiment sample images of QEMSCAN, surface area change is very prominent in the edges of the samples. Also, visible porosity changes in Micro-CT results reveal some minor changes in the fluid-rock interface area over the two-week period. These are some of the evidence that CO_2-related reactions are present to some extent in all studied samples. However, one of the weak points in the Micro-CT analysis is that the surface areas cannot be accurately distinguished on the 2D and 3D images, and the surface area represents the whole surface area of the void mineral interface. The surface area increase is related to the pore volume and pore size decreases. These changes are explained by a decrease in mineral mass/concentration and an increase in the pore volume as porosity increases. Qualitative observations of the Micro-CT images show that pore size increases with reaction time in the sandstone and limestone samples (Figure 25 and Figure 26). However, it can also be seen that the dolomite sample is relatively unreactive and show little to no changes in pore size. Because the Micro-CT results are only a qualitative analysis of surface area, the changes in surface area were measured using the BET. Micro-CT software does exist that could calculate the pore volume based on each slice of the Micro-CT analysis. However, the exterior surface of the core plug would not be adequately measured due to the parameters of the software.

Surface area values for both unreacted and reacted samples according to the BET results were very low, naturally reflecting the low surface areas of the component minerals. Based on Table 5, the unreacted samples have different surface area range; 0.8269 to 1.0953 m^2/g in sandstone, 0.3235 to 1.4086 m^2/g in limestone, and 0.0023 to 1.2132 m^2/g in dolomite; reacted samples have little spacious gap compare with unreacted samples; 1.0888 to 1.4838 m^2/g in sandstone, 0.3558 to 1.5845m^2/g in limestone, and 0.0026 to 1.7099 m^2/g in dolomite. These characteristics result in a small difference in the sandstone surface area due to homogeneity, and large differences in the dolomite and limestone surface areas due to heterogeneity.

When comparing the surface areas before and after the reaction, it can be seen that the surface area increases after the reaction with the least amount of surface area change being 7.45 % and the greatest amount of surface area change being 40.94 %, relatively. The surface area generally increases after the reaction, and the pore size generally decreases after the reaction. The reduced pore size range is from the lowest reduction being 3.49 % and the greatest reduction being 56.89 %. These results imply that despite the very low surface areas, there appears to be a trend that may reflect the dissolution observed during the reaction. This also suggests that the reaction occurs on the core surface, where it generates new pores. The implications of the data infer that the generation of new pores is more dominant than the expansion of existing pores, thus resulting in a lower average pore size and a greater surface area.

If the reactions were to be continued for more than the two-week period, it is speculated that the pore size would increase and the surface area would decrease. This would be the result of new pores being generated and connecting to each other, as well as increased dissolution of the rock. To sum up, the reactions occur primarily on the surface of the minerals, and then secondary pores - new small pores - are generated by the reactions.

Table 5. Summary of BET results for the core samples regarding different types and forms

	Surface area (m^2/g)			Pore volume (cm^3/g)						Pore size (Å)					
	Before	After	Variation	BJH Adsorption			BJH Desorption			BJH Adsorption			BJH Desorption		
				Before	After	Variation	Before	After	Variation	Before	After	Variation	Before	After	Variation
Core plug samples															
A 103 II Sandstone	0.8926	1.1095	24.3%	0.003105	0.003447	11.01%	0.006651	0.010389	56.20%	205.146	178.477	-13.00%	284.877	193.789	-31.97%
B 101c II Limestone	0.3235	0.3558	9.98%	0.001996	0.002202	10.32%	0.005659	0.004957	-12.40%	467.950	412.815	-11.78%	507.039	516.123	1.79%
B 109 II Dolomite	0.0023	0.0026	13.04%	0.000276	0.000392	42.02%	0.004264	0.006208	45.59%	758.470	618.912	-18.40%	1108.067	1041.231	-6.03%
Fracture samples															
A 103 I Sandstone	0.8269	1.0888	31.67%	0.004035	0.003462	16.55%	0.010786	0.005411	99.33%	202.368	157.662	-22.09%	424.687	183.089	-56.89%
B 101c I Limestone	0.2740	0.3260	18.98%	0.002172	0.002379	9.53%	0.011667	0.014070	20.60%	665.902	559.280	-16.01%	838.847	844.428	0.67%
B 109 I Dolomite	0.0550	0.0591	7.45%	0.000182	0.000316	73.62%	0.001307	0.002872	119.73%	1056.849	677.555	-35.89%	1040.645	1004.298	-3.49%
Powder samples															
A 103 I Sandstone	1.0953	1.4838	35.47%	0.004544	0.006392	40.67%	0.013551	0.009903	-26.92%	188.044	206.468	9.80%	453.838	275.288	-39.34%
B 101c I Limestone	1.4086	1.6845	19.58%	0.006417	0.008594	33.93%	0.009659	0.019082	-49.38%	230.183	318.434	-27.71%	328.629	521.676	-37.01%
B 109 I Dolomite	1.2132	1.7099	40.94%	0.005749	0.011135	93.69%	0.011996	0.018627	55.28%	251.649	240.143	-4.57%	458.214	419.728	-8.40%

Modeling Section

Reactive Transport Modeling of the core floods

For simulating the process of flow, manufacture-provided porosity value was verified against helium (He) porosimeter measurement. Permeability value was verified using the pressure drop data obtained during the blank test where only 2% brine was injected into the core and no reactions took place. Values of 0.21 and 45 mD have been used in the model for porosity and permeability, respectively.

The experimental conditions of confining pressure and temperature represents a brine aquifer at the depth of approximately 3000 ft or 1000m, which is consistent with some of the potential CO_2 storage site selections (Gaus 2005, Carroll, McNab et al. 2013). Under these conditions, free CO_2 will stay in supercritical form. As supercritical CO_2 phase is modeled as gas phase in the simulator, and excessive CO_2 is injected, constitutive relationships for relative permeability and capillary pressure are provided for multiphase flow calculations. Van Genuchten-Mualem model (van Genuchten 1980) is used for relative permeability of liquid.

$$k_{rl} = \begin{cases} \sqrt{s^*}\left\{1-\left(1-[s^*]^{1/\lambda}\right)^{\lambda}\right\}^2 & if\ s_l < s_{ls}, \\ 1 & if\ s_l \geq s_{ls} \end{cases} \quad (1)$$

where $s^* = (s_l - s_{lr})/(s_{ls} - s_{lr})$ is scaled saturation of liquid, s_{lr} is the residual saturation, s_{ls} is the saturated liquid saturation, and λ is the shape factor that converts an arbitrary shape of grains into to spheres. For gas relative permeability, Corey (Corey 1954) is used.

$$k_{rg} = \begin{cases} (1-\tilde{s})^2(1-\tilde{s}^2) & if\ s_{gr} > 0 \\ 1 - \ k_{rl} & if\ s_{gr} = 0 \end{cases}. \quad (2)$$

Here, $\tilde{s} = (s_l - s_{lr})/\left(1 - s_{lr} - s_{gr}\right)$ is scaled saturation of gas, s_{gr} is the residual saturation of gas.

As for the capillary pressure between gas and liquid, we employ the van Genuchten function:

$$P_{cap} = -P_0\left([s^*]^{-1/\lambda} - 1\right)^{1-\lambda}, \quad (3)$$

where P_0 is the strength coefficient and has the unit of pressure. Parameter specifications were chosen to be representative of conditions that may be encountered in brine formations at a depth of order 1 km (Xu 2003) and their values are listed in Table 6.

Table 6. Multiphase flow parameters

Relative Permeability	s_{lr}	s_{ls}	λ	s_{gr}
	0.3	1.0	0.457	0.05
Capillary Pressure	s_{lr}	s_{ls}	λ	P_0 (kPa)
	0.0	0.999	0.457	19.6

For geochemical reactions, initial mineral composition was determined by Quantitative Evaluation of Minerals by Scanning electron microscopy (QEMSCAN) on the unreacted core. QEMSCAN creates phase assemblage maps of a specimen surface scanned by a high-energy accelerated electron beam along a predefined raster scan pattern. Low-count energy-dispersive X-ray spectra (EDX) are generated and provide information on the elemental composition at each measurement point. The elemental composition in combination with back-scattered electron (BSE) brightness and x-ray count rate information is converted into mineral phases (Gottlieb 2000). Seven slices of unreacted core were analyzed with a scanning resolution of 4 μm × 4 μm. The average of measured areal distributions are the input of mineral volume fractions. The mineralogy data and volume fraction values are shown in Table 7. It is worth noting that void fraction is also measured and it is consistent with the porosity value used in the model. The modeled minerals occupy 98.1% of the total volume and they are selected due to their significant amount and/or the ability to be accommodated by the simulator.

Table 7. Modeled mineralogical composition of the sandstone

Mineral	Initial Volume Fraction (%)	Modeled Mineral
Quartz	65.26	quartz
K-feldspar	3.49	k-feldspar
Illite	2.79	illite
Kaolinite	2.07	kaolinite
Plagioclase	1.86	oligoclase
Smectite	0.6	smectite-ca
Chlorite	0.65	chlorite
Muscovite	0.17	muscovite
Rutile	0.1	not modeled
Siderite	0.06	siderite
Fe-oxides	0.06	hematite
Ankerite	0.08	ankerite
Glauconite	0.04	not modeled
Pores	21.0	porosity
Total	98.1	

In TOUGHREACT simulator, flow-transport and reactions are solved sequentially. As the injected fluids are distributed uniformly across the bottom of the core and material properties of the core are uniform, the flow process is modeled as one-dimensional flow in a homogeneous medium. Along the z direction, the model domain is discretized into a uniform structured grid of 60 cells for the length of 7 inches or 18 cm. The flow at the bottom boundary is at constant mass flow rate for all 3 components: 1.65×10^{-5} Kg/s of water, 1.65×10^{-5} Kg/s of CO_2 and 3.33×10^{-7} Kg/s of salt; and the top outlet is at constant pressure of 2000 psi or 1.38E7 Pa. Flow process reaches steady state relatively fast, thus the time step sizes are determined by the chemical processes. Time step size starts at 18 s and is allowed to increase to a maximum of 1800 s.

The chemical reactions induced by CO_2 injection are described in general by Wawersik et al. (Wawersik 2001). First, CO_2 dissolves in water to produce the weak carbonic acid. The dissolved bicarbonate species react with divalent cations to precipitate carbonate minerals. Formation of Ca, Mg, and Fe(II) carbonates are expected to be the primary means by which CO_2 is immobilized. For our system, based on the

mineralogy of the core, 12 primary species are identified to describe the geochemical system that is solved following the primary species solution method (Xu and Pruess 1998). Minerals dissolution and precipitation reactions are expressed in terms of the primary species with stoichiometric coefficients (Table 8).

Table 8. Stoichiometric matrix for mineral reactions.

	h2o	h+	ca+2	mg+2	na+	k+	fe+2	sio2(aq)	hco3-	alo2-	cl-	o2(aq)
quartz	0	0	0	0	0	0	0	1	0	0	0	0
k-feldspar	0	0	0	0	0	1	0	3	0	1	0	0
illite	0.4	1.2	0	0.25	0	0.6	0	3.5	0	2.3	0	0
kaolinite	1	2	0	0	0	0	0	2	0	2	0	0
plagioclase	0	0	1	0	4	0	0	14	0	6	0	0
smectite-Ca	0.52	0.96	0.145	0.26	0	0	0	3.97	0	1.77	0	0
chlorite	8	-8	0	2.5	0	0	2.5	3	0	2	0	0
muscovite	0	2	0	0	0	1	0	3	0	3	0	0
siderite	0	-1	0	0	0	0	1	0	1	0	0	0
hematite	2	-4	0	0	0	0	2	0	0	0	0	0.5
ankerite	0	-2	1	0.3	0	0	0.7	0	2	0	0	0

All mineral dissolution and precipitation are considered to be kinetically controlled. A general form of rate law (Lasaga 1984) is used

$$r_n = k_n A_n \left(1 - {\Omega_n}^{\theta}\right)^{\eta} \qquad n = 1, \ldots, N_q, \qquad (4)$$

where positive values of r_n indicate dissolution and negative values precipitation, k_n is the rate constant which is temperature dependent, A_n is the specific reactive surface area, Ω_n is the kinetic mineral saturation ratio defined as $\Omega_n = K_m^{-1} \prod c_j^{\nu} \gamma_j^{\nu}$, the ion activity product divided by the equilibrium constant K_m, θ and η are exponents determined from experiments, usually taken equal to 1. Ion activity coefficients are estimated using the Debye-Huckel equation since our system is at relatively low ionic strength. The kinetic rate constant k_n in Eq. (4) only considers the best-studied mechanism in pure H_2O at neutral pH. Dissolution and precipitation of some modeled minerals are catalyzed by H^+ (acid mechanism) and OH^- (base mechanism). As a more general form of the kinetic rate constant, it is

$$k = k_{25}^{nu} exp\left[\frac{-E_a}{R}\left(\frac{1}{T} - \frac{1}{298.15}\right)\right] + {k_{25}}^{H} exp\left[\frac{-{E_a}^{H}}{R}\left(\frac{1}{T} - \frac{1}{298.15}\right)\right] a_H^{n_H}$$

$$+ {k_{25}}^{OH} exp\left[\frac{-{E_a}^{OH}}{R}\left(\frac{1}{T} - \frac{1}{298.15}\right)\right] a_{OH}^{n_{OH}}. \qquad (5)$$

Table 9 lists the values of the kinetic parameters used in the simulations. Specific reactive surface areas are assigned representative values for two mineral groups: clay minerals and non-clay minerals. Clay minerals have a higher surface area and non-clay minerals a lower one. Reaction rate constants at 25 °C for the selected minerals are taken from literature (Xu 2003, Gaus 2005).

Table 9. Specific reactive surface areas and kinetic rate constants at 25 °C of minerals.

	Reactive Surface area (cm^2/g)	k^{nu} (mol/m^2 s)	k^{H} (mol/m^2 s)	k^{OH} (mol/m^2 s)
quartz	9.8	1.02E-14		
k-feldspar	9.8	3.89E-13		
illite	151.6	1.66E-13	1.05E-11	3.02E-17
kaolinite	151.6	6.92E-14	4.90E-12	8.91E-18
plagioclase	9.8	1.45E-13	2.14E-11	
smectite-Ca	151.6	1.66E-13	1.05E-11	3.02E-17
chlorite	9.8	3.02E-13	7.76E-12	
muscovite	151.6	1.40E-13		
siderite	9.8	1.26E-09	1.46E-04	
hematite	12.9	2.51E-15	4.07E-10	
ankerite	9.8	1.26E-09	6.46E-04	

Porosity changes in matrix are the results of volume changes due to mineral precipitation and dissolution. Using the option of cubic porosity-permeability relationship, changes in permeability are computed:

$$kp/kp_i = (\phi/\phi_i)^3, \qquad (6)$$

where kp_i and ϕ_i are initial permeability and porosity, kp and ϕ are the final values.

Metal cation concentration evolution in the effluent

Temporal evolution of total iron concentration in effluent has been used to calibrate the kinetic parameters in the model. In contrast to what was previously hypothesized in (Xu 2010), illite is not the main source of iron. From the two iron sources of siderite and ankerite identified, we obtained the total iron concentrations with time at the outlet as shown in Figure 28. Solid line is the simulation output while the circles are the ICP-MS measurements. The peak experimental value was used to calibrate the total mineral content and the acidic mechanism kinetic rate constant of siderite. Calibrated mineral volume fractions for ankerite and siderite are 0.06% and 0.05%, and they are very close to measured data of 0.08% and 0.06% as listed in Table 7. Comparted to the kinetics used in literature (Xu 2003, Gaus 2005), the only calibrated value of $k_{25}{}^{H}$ for siderite, 1.46E-4, is about 4.4 times smaller. The model is able to capture the general trend of a rapid increase to the peak value within the same time frame on the order of hours and then a more gradual decrease. Ankerite dissolution also produces magnesium and calcium. Similar trends in Mg and Ca concentration evolution are predicted, as a drastic increase followed by a drop to a steady value by the model as shown in Figure 28. Discrepancy between simulation and experiment are approximately 50%. The overestimation of Mg and underestimation of Ca may indicate that solid solution is present and various ratios among the bivalent cations could occur in the same mineral of ankerite. Readers are referred to (Reeder and Dollase 1989) for more information on ankerite solid solution.

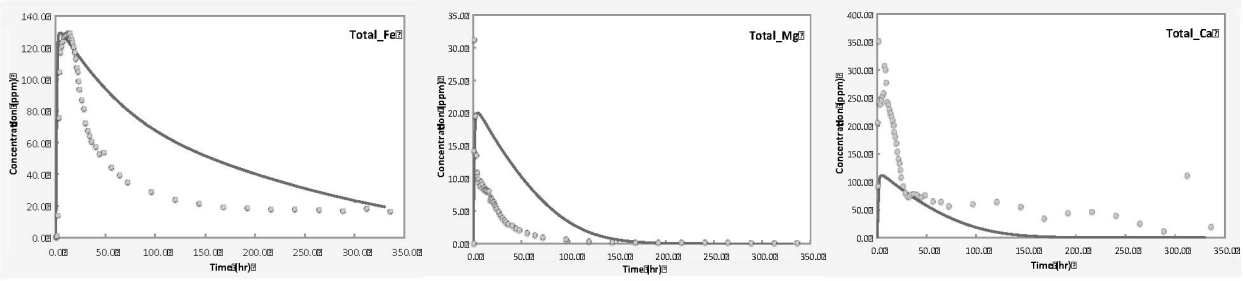

Figure 28: Comparison between simulation and experimental results for major metal cation concentration change with time at outlet.

Mineralogy Alteration in the Core

Considerable amount of dissolution took place for siderite and ankerite during the two-week period. Ankerite is completely dissolved and 85% of total volume of siderite has been washed out. Dissolution of the two source minerals takes place at different rates along the core, faster at inlet and slower towards outlet (Figure 29) as pH increases from inlet to outlet (Figure 30). For both minerals, the volume fraction line for the near-inlet location (z = -0.151 m) sits on top of that for the near-outlet location (z = -0.029 m) throughout the simulation period. CO_2 sequestered in mineral form is calculated by transforming the difference in the volume fraction of carbon-containing minerals per volume of medium back to the mass of gaseous phase CO_2. Minimum carbon sequestered in mineral phase is calculated predicted to be -1.47 Kg/m^3 at the inlet of the core, indicating carbon release from dissolution of minerals.

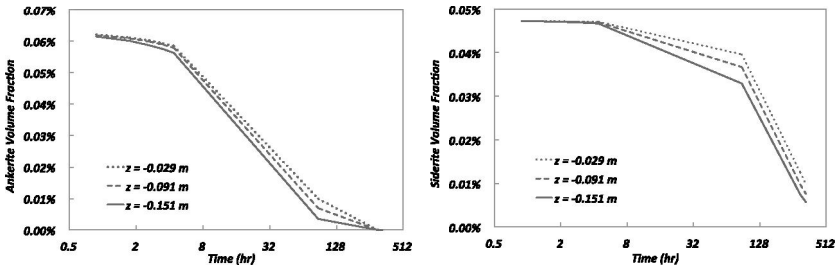

Figure 29: Simulation results of ankerite and siderite content change with time at different locations in the core.

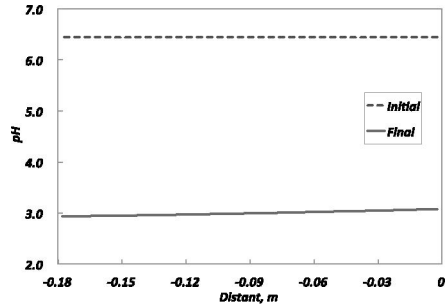

Figure 30: Initial and final pH distribution along the core

Porosity and permeability changes

As a result of mineral dissolution, porosity and permeability increases throughout the core. Porosity and permeability changes were calculated according to cubic law. Due to the mineral kinetic rate distribution, more significant changes take place towards the inlet than towards the outlet. Maximum amount is predicted to be 0.5% and 1.5% for porosity and permeability, respectively. Figure 31 shows the comparison between initial and final values of porosity and permeability distribution in the core. Compared to the porosity measurements after reactions in (Kweon 2015), no porosity decrease was observed in the simulations. In addition to the measurement error of porosimeter, a possible explanation is that a more complex relationship between mineral dissolution/precipitation and reaction affinity than what Eq. (4) proposes exists. Additional model may be needed such as the combined surface complexation model and transient state theory proposed

by (Schott 2009) to fully capture the reactions that are indeed taking place on the surfaces. The other consideration is the heterogeneity was not incorporated in the model.

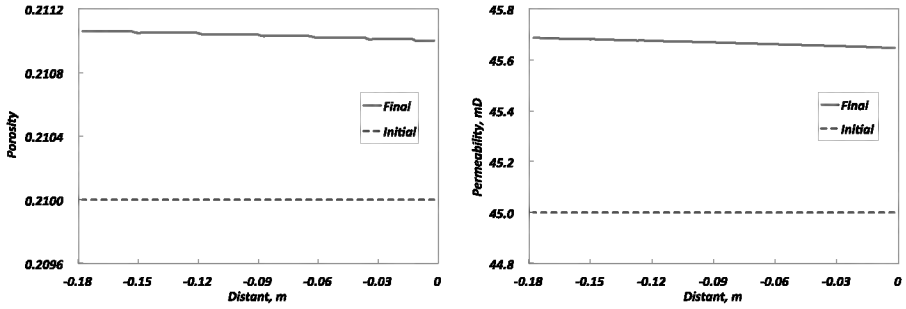

Figure 31: Predicted porosity and permeability changes along the core for initial and final values.

System behavior at larger spatial scale

Observations made in the core flooding experiments with limited size have shown that dissolution is the dominating process and high levels of metal cations are generated. The implications we gathered from these observations are that the metal cations could be important sources for carbonate minerals further downstream. Hence, with the calibrated model, we also carried out simulations of the behavior of our system at extended spatial scale to investigate the possibility of mineral precipitation and carbon fixation. A new one dimensional model is constructed with the length 10 times longer than the dimension of the sandstone core, or 1.8 m, and is discretized with the interval of 0.3 m along z direction. Fluids are injected at the bottom of the domain. Same boundary conditions are used, i.e., injection rate, composition of injection fluid. Using the calibrated kinetic parameters and mineral composition, we have simulated the injection process for 640 hours, or 26.6 days, which is equivalent to 50 pore volumes of fluid injection. We found that ankerite and siderite remain the two dissolving minerals. As shown in Figure 32, ankerite is under continuous dissolution conditions throughout the simulated time. It completely disappears at the end of the simulation. For siderite, dissolution takes place initially along the whole length of the core (line for time = 2.4 days in Figure 33). Starting at 3.7 days, kinetics of siderite reactions transits from dissolution at the bottom to precipitation at the top of the domain. This trend continues until the 12th day. As time progresses the transition point moves towards downstream. The reprecipitated mineral eventually dissolves. Predicted porosity and permeability changes at the end of the simulation are plotted in Figure 34. Compared to the shorter domain at the same 50 pore volumes (or 2.67 days), values of porosity and permeability are both higher in the longer domain simulation. This is because of the same reaction kinetics and the longer absolute reaction time in this case. It is also noted that the difference between the inlet and outlet properties is larger for the longer domain. At 50 pore volumes, difference between inlet and outlet permeability is 0.179 mD for 1.8 m domain and 0.139 mD for 0.18 m domain. This may be interpreted as that the mineral reprecipitation contributed to inhibiting flow and transport thus reduced the residence time of reacting fluid downstream while increased it upstream.

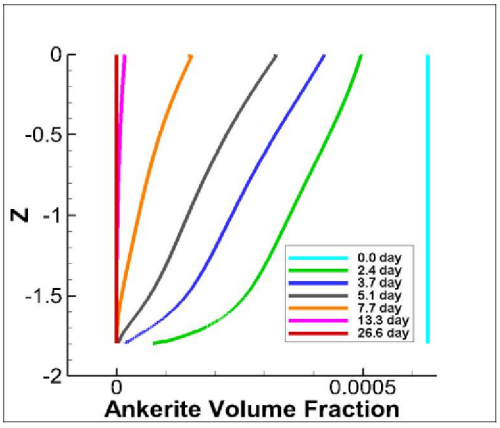

Figure 32: Temporal changes in spatial distribution of ankerite along the core in z direction.

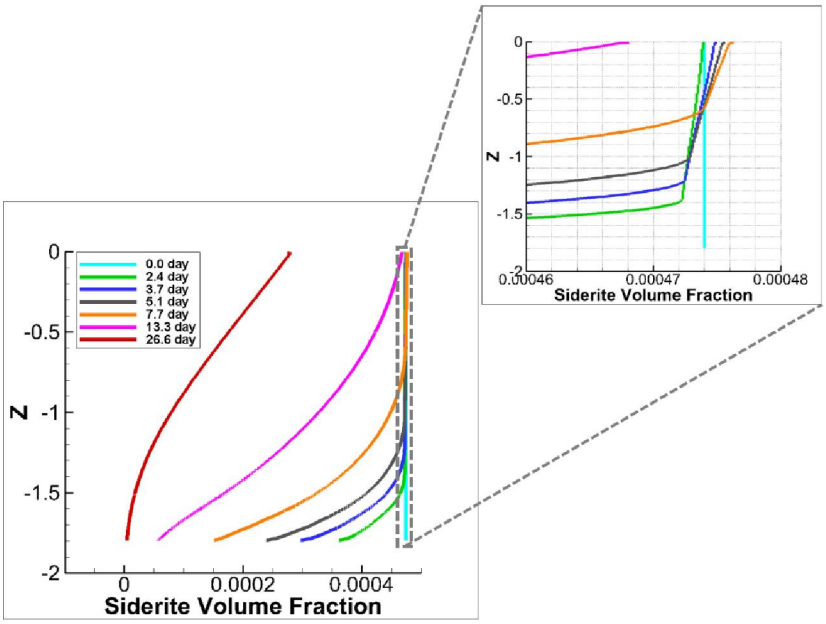

Figure 33: Temporal changes in spatial distribution of siderite with time, and the insert shows details of siderite reprecipitation in the downstream region (navy, black and orange lines for 3.7, 5.1 and 7.7 days).

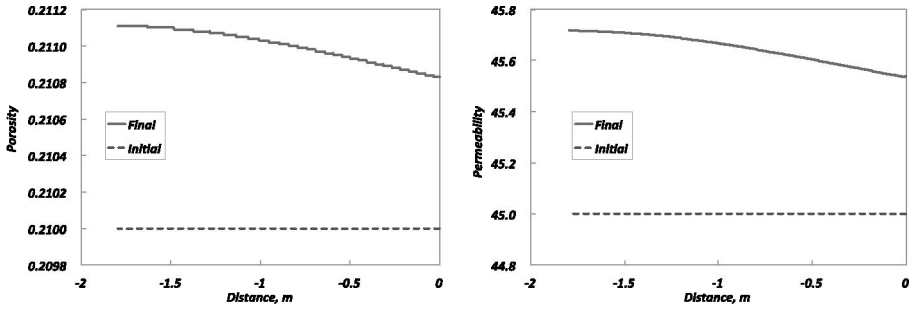

Figure 34: Simulated porosity and permeability changes along the core for initial and final values at larger spatial scale.

Batch Experiment Modeling

In order to interpret the mineral dissolution and precipitation kinetics, many scientists and researchers developed expressions that described the dependence of mineral dissolution. A general form of rate expression in equation (1) was written to express the dependence of rate upon solution chemistry by the widely used expression:

$$r = kA\left[1 - \left(\frac{Q}{K}\right)^{\theta}\right]^{\eta} \qquad (1)$$

where r is the reaction rate, k is the rate constant which is temperature dependent, A is the specific reactive surface area, K is the equilibrium constant for the mineral-water reaction, and Q is the reaction quotient. The parameters θ and η must be determined by experiment.

All mineral and solution equilibriums were computed using EQ3/6 v8.0a. For an example, illite solubility is expressed by the reaction,

$$\text{Illite} + 8H^{+} = 0.25\ Mg^{2+} + 0.6\ K^{+} + 2.3\ Al^{3+} + 3.5\ SiO_2\ (aq) + 5\ H_2O \qquad (2)$$

In EQ3/6 v8.0a, the reactants and products accommodate the mass balance of all derived dependent species and solution complexes that may form under the defined conditions. Therefore equation (2) simply provides a means of evaluating the distance from equilibrium from pure ordered illite:

$$Q = {a_{Mg^{2+}}}^{0.25} {a_{K^{+}}}^{0.6} {a_{Al^{3+}}}^{2.3} {a_{SiO_2}}^{3.5} {a_{H_2O}}^{5} {a_{H^{+}}}^{-8} \qquad (3)$$

Activity coefficients are computed using EQ3/6's "B-dot" function. In the case of minerals, data0.cmp obtains thermodynamic reference mineral data.

In order to understand the impact of surface area heterogeneity, heterogeneity on reactive transport processes has to be observed. One of the best points of comparison for the pore network model simulations was provided by L. Li et al. (2007).(Li 2007) The mineralogical composition assumed in that work was generally similar to the Berea sandstone in this study. It was verified that heterogeneity in the distribution of reactive surface area in the pore space could give rise to large deviations in effective reaction rates. Currently, pore scale observations of the surface area properties are available and the distributions are based on specific analytical instrument such as QEMSCAN for various rock samples including the Berea sandstone.

Mineral distributions of Berea sandstone have been measured by QEMSCAN to be converted to surface area values. An accurate conversion depends on a characterization of correlations between the geometric area of a mineral and the observations with BET adsorption specific to those minerals which were unavailable for this work. Lai et al. (2015)(Lai 2015) provided a first order estimate of what this conversion might look like based on surface area measurements of various mineral groups reported in the literature.

$$A_{BET} = \beta A_{geom} \qquad (4)$$

where the average roughness factor, β, of BET surface area, A_{BET}, to QEMSCAN derived geometric surface area for Berea sandstone, A_{geom}. The calculation for the roughness factor was reported in P. Lai et al. (2015). This roughness factor can be thought to be made up of contributions from the surfaces of specific minerals,

$$\beta = f_{qtz}\beta_{qtz} + f_{clay}\beta_{clay} + f_{fsp}\beta_{fsp} + f_{other}\beta_{other} \quad (5)$$

where f_i is the fraction of the geometric surface areamade up of mineral group i, $\sum_i f_i = 1$ and β_i are roughness factors following the same relationship as shown in equation (4).

Mineralogy Changes by Reaction Time and Different Reactive Surface Area: ICP-MS

Solution analysis of the effluent are shown in Figure 35, and computed saturation states are presented in Table 10. Before studying the effects of the different surface areas of the core samples (different forms), mineral dissolution patterns were determined and plotted by cation concentration over time with the Berea sandstone core plug sample. Four major elements are compared with the simulation results; (a) iron, (b) magnesium, (c) calcium, and (d) potassium. The scattered data points display the experimental ICP-MS data, and the solid line represents the simulation data. The steady state dissolution rates are too slow for quantification within the time frame of the experiments.(Lee 2015) Iron (Figure 35 (a)) and magnesium (Figure 35 (b)) concentrations before 48 hours and after 48 hours show different dissolution rates; this is believed to be caused by the rapid and complete dissolution of ankerite minerals, as explained by Kweon (2015). Additionally, in the case of iron, siderite mineral dissolution also contributes to the initially steep

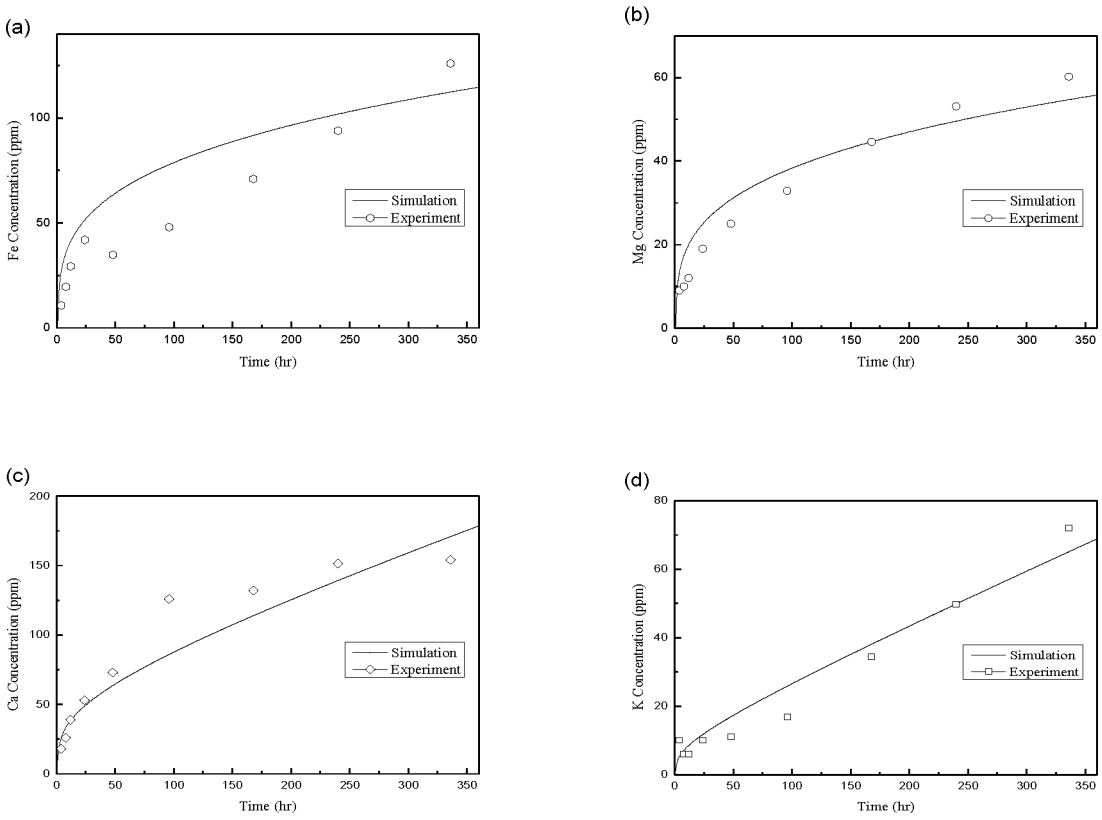

Figure 35. Concentration of (a) iron, (b) magnesium, (c) calcium, and (d) potassium ions as measured by ICP-MS in the effluent for Berea sandstone time step batch experiments compared with simulation results

iron concentration profile. Relative to the other iron source minerals (ankerite and siderite), chlorite and smectite are slowly and steadily dissolved. The dissolution rates of chlorite and smectite are affected by reactive surface area. Because of this phenomena, the iron concentration increases steadily. On the other hand, the slope of the magnesium cation concentration is relatively low since ankerite is the main contributor initially. The calcium concentration profile (Figure 35 (c)) differs slightly compared to that of iron and magnesium. During 48 hours, the profile identifies similar trends due to ankerite dissolution. The extended time of rapid dissolution is caused by simultaneous dissolution of additional calcite minerals. As is well known, calcite is a very active mineral for dissolution. The potassium concentration profile (Figure 35 (d)) shows a completely different pattern. Unlike the aforementioned cations, smectite affects potassium concentration in the beginning rather than ankerite. After 48 hours, other potassium source minerals such as illite, alkali feldspar, and muscovite are constantly dissolving.

Table 10. Saturation state data, T = 60 ºC

	K_{25}	Ea (kJ/mol)	Area (cm^3/g)			Log K	Ref.
			Core plug	Fracture	Powder		
Illite	1.00E-13	22	2.854	3.081	3.781	5.5551	Arvidson and Luttge(2010)
Alkali feldspar	1.78E-10	51.7	27.201	29.363	36.031	-0.9610	Arvidson and Luttge(2010)
Plagioclase	1.00E-12	30	13.775	14.869	18.246	2.6839	Baccar, et al. (1993)
Chlorite	1.00E-9.91	25.1	0.413	0.446	0.547	55.7725	Smith, et al. (2013)
Smectite	8.08E-14	28	0.343	0.370	0.455	13.4522	Elliott and Matisoff(1996)
Ankerite	1.26E-09	62.76	1.193	1.288	1.581	1.3314	Arvidson and Luttge(2010)
Muscovite	1.00E-13	22	0.104	0.113	0.138	8.8387	Arvidson and Luttge(2010)
Micrite	1.50E-06	41.9	0.845	0.913	1.120	1.3330	Arvidson and Luttge(2010)
Siderite	1.00E-09	62.8	0.497	0.537	0.659	-0.8309	Arvidson and Luttge(2010)

$Illite + 8\ H^+ = 0.25\ Mg^{2+} + 0.6\ K^+ + 2.3\ Al^{3+} + 3.5\ SiO_2\ (aq) + 5\ H_2O$

$Alkali\ feldspar + 4\ H^+ = Al^{3+} + K^+ + 2\ H_2O + 3\ SiO_2\ (aq)$

$Plagioclase + 8\ H^+ = Ca^{2+} + 2\ Al^{3+} + 2\ SiO_2\ (aq) + 4\ H_2O$

$Chlorite + 16\ H^+ = 2.3\ Al^{3+} + 3\ SiO_2\ (aq) + 5\ Fe^{2+} + 12\ H_2O$

$Smectite + 8\ H^+ = 0.025\ Ca^{2+} + 0.1\ Na^+ + 0.2\ Fe^{3+}\ 0.2\ K^+ + 0.5\ Fe^{2+} + 1.15\ Mg^{2+} + 1.25\ Al^{3+} + 3.5\ SiO_2\ (aq) + 5\ H_2O$

$Ankerite + 2H^+ = Ca^{2+} + 0.3\ Mg^{2+} + 0.7\ Fe^{2+} + 2\ HCO_3^-$

$Muscovite + 10\ H^+ = K^+ + 3\ Al^{3+} + 3\ SiO_2\ (aq) + 6\ H_2O$

$Micrite + H^+ = Ca^{2+} + HCO_3^-$

$Siderite + H^+ = Fe^{2+} + HCO_3^-$

Upon completion of the experiments with different surface areas, each of the collected effluent samples were analyzed using ICP-MS. This data set is shown in Table 11. Sodium is used as a standard cation to check the accuracy of ICP-MS analysis because the 2 wt. % NaCl brine was used for all of the experiments. In the blank test, the concentrations of minerals such as magnesium, aluminum, and iron were slightly above the ICP-MS detection limit. This suggests possible evidence for 316 stainless steel reactor corrosion. To minimize the reactor corrosion effect, the reactors were replaced after a few experiments.

As shown in Table 11, most of the cations' concentrations are increased when the BET surface area of the sample is increased, matching the proposed hypothesis. Magnesium exhibits a trend of increasing concentration as the BET surface area of the sample is increased. As mentioned earlier, illite, chlorite, smectite, and ankerite dissolution would be the source of the magnesium concentration increase in the Berea sandstone. There is a large concentration difference in aluminum concentration when compared with silica, especially in powder samples. Most minerals have an aluminum source except ankerite, micrite, and siderite. Based on surface area effect theory, alkali feldspar and plagioclase are the most major mineral sources for aluminum from Table 10. Silica displays a narrow change in concentration by increasing reactive surface area from core plug to powder samples. There are many possible sources of silica such as quartz, illite, alkali feldspar, plagioclase, chlorite and smectite. Quartz is a dominant mineral in the Berea sandstone but is unreactive with the CO_2 and brine solution. Therefore, illite and alkali feldspar are the primary source of silica in the effluent because of their higher volume fraction and surface area compared with other minerals.

Table 11. ICP-MS results for core plug, fractured, and powder samples after two week batch experiment at 60 °C and over 2000 psi

	Na (mg/kg)	Mg (mg/kg)	Al (mg/kg)	Si (mg/kg)	K (mg/kg)	Ca (mg/kg)	Fe (mg/kg)
LoD	2	0.004	0.06	0.06	7	13	0.05
Blank	7024	0.68	0.64	0.22	<7	<13	1.92
Core plug	7108	60.2	27.2	3.8	72	154	126
Fracture	7103	109	64.9	8.4	140	204	192.1
Powder	6904	167.2	98.5	17.2	211	384	271.44

Potassium, calcium, and iron each show similar increases in concentration with increasing surface area. The main reactive minerals containing potassium in the Berea sandstone is illite, alkali feldspar, smectite, and muscovite. Whereas, plagioclase, smectite, and ankerite are the main calcium-containing minerals found in the Berea sandstone. Illite and alkali feldspar have a relatively high volume fraction and surface area when compared to smectite and muscovite; therefore, illite and alkali feldspar have the greatest effect on the concentration of potassium. Plagioclase, smectite, and ankerite contribute to increasing calcium concentrations due to the high volume fraction and surface area presented by plagioclase and high reactivity for smectite and ankerite. The iron concentration in the Berea sandstone shows interesting results which are similar to previous core flooding experiment results. Each of the sandstone effluent samples shows large concentrations of iron, indicating dissolution of iron containing minerals. Based on our previous core flooding experimental and simulation results, these iron-containing minerals are mainly attributed to chlorite, smectite, ankerite and siderite.(Kweon 2015) Carroll et al. (2013) touched only on dissolution reactions with iron-containing clay minerals in sandstone under CO_2 storage conditions. Whereas, it can be

seen that not only clay minerals such as chlorite and smectite, but also carbonate minerals such as ankerite and siderite, influence iron concentrations in this study.

The total mineralogical changes in the batch experiments are lower than those found in the core flooding experiments and simulation results, Kweon (2015). In the core flooding experiments, reactive fluid was continuously injected. However, in the batch experiments the rock samples were contained in the unchanged fluid over the two week period. The different fluid conditions caused different dissolved element concentrations. In the non-flowing environment of the batch system, reactivity of mineral dissolution is affected by reactive surface area changes. However, measuring the true reactive surface area presents significant challenges. Therefore, the reactive surface area is regarded as being the geometric surface area in this study. In order to calculate the geometric surface area, the roughness factor (β) was applied. By means of the roughness factor (β), correlations between the geometric area of a mineral and the BET surface area of that mineral, were generated.

In Figure 36, four major elements are also compared with the simulation results; (a) iron, (b) magnesium, (c) calcium, and (d) potassium, respectively. The scattered data points without lines are the batch experimental ICP-MS data, and the solid and dotted lines are the simulation data according to different

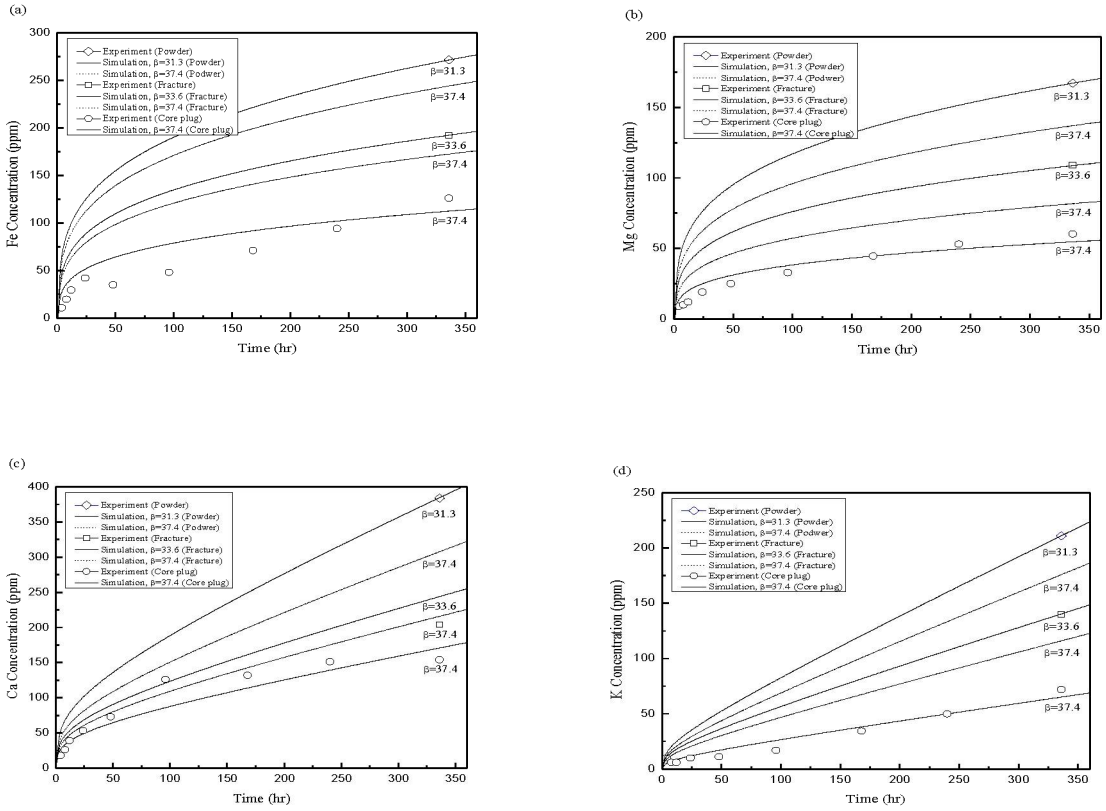

Figure 36. Concentration of (a) iron, (b) magnesium, (c) calcium, and (d) potassium ions as measured by ICP-MS in the effluent for different reactive surface area of Berea sandstone time step batch experiments compared with simulation results

reactive surface area. The several experimental data points were measured for the core plugs at several different times. Above all, roughness factor was calculated using the equation (4) standing on the basis of BET and QEMSCAN measurement. The measured A_{BET} and A_{geom} for the core plug sample were used to calculate an average roughness factor of 37.4 for the Berea sandstone. Due to the inability to obtain an A_{geom} value for the fractured and powder samples, this same roughness factor (37.4) was used for each sample type. A two week experiment was carried out for the powder and fractured sample and the final data points are contained in the Figure 36. These final experimental data points are slightly above the simulation results (solid line) using roughness factor, 37.4. The difference between the simulation results and these experimental data points for the powder and fractured samples may be, in part, caused by the assumption of using the average roughness factor in equation (4) that was calculated using the core plug sample. In order to find roughness factor for fracture and powder samples, geometric surface area was modified based on BET surface area and experimental data points. As shown in Table 12, the calculated roughness factors for fracture and powder samples are 33.6 and 31.3, respectively. The dotted lines are plotted by means of the calculated roughness factor value in Figure 36. Mineral dissolution trends and the final data points of effluent cation concentration were well matched when calculated roughness factors were used.

Table 12. Calculated values of roughness factor

	A_{BET} (cm^2/g)	β	A_{geom} (cm^2/g)	β_m*	A_{geom} (cm^2/g)
Core plug	8269	37.4	221.09	37.4	221.09
Fracture	8926	37.4	238.66	33.6	265.81
Powder	10953	37.4	292.86	31.3	350.11

* β_m : modified β value based on the dissolved mineral concentration using TOUGHREACT

Reactive Transport Modeling and Geomechanical Coupling

Over the past a few years, INL's has developed a number of pore-scale reactive flow simulators based on various methods, including level set, volume of fluid, phase field, smoothed particle hydrodynamics and dissipative particle dynamics. All those pore-scale codes had been applied to study the detailed single- and multi-phase flow dynamics in pores, and some methods were extended to study pore geometry evolutions due to mineral precipitation and dissolutions (only with simple chemistry A+B=C), and the feedbacks of pore geometry changes to the changes of permeability and porosity.

Specifically interesting to this project is to using INL's pore-scale codes to study pore/fracture geometrical evolutions under different flow rates of CO2 bearing fluids, typically measured by Peclet number (Pe) and mineral dissolution (or precipitation) rates, measured by Damköhler number (Da). So we applied the reactive flow code based on level set method to track the pore geometry changes due to calcite precipitation. Figures 37 and 38 shows two example pore-scale reactive flow simulations that involves mineral precipitation and dissolution.

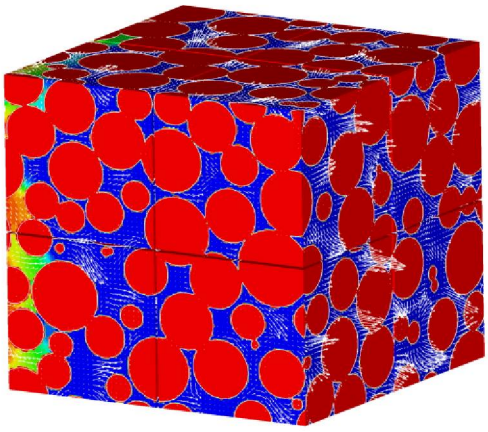

Figure 37. MPI-based parallel pore-scale reactive flow simulation using level set method. Pore/mineral interfaces and their spatial-temporal evolutions are tracked using level set method.

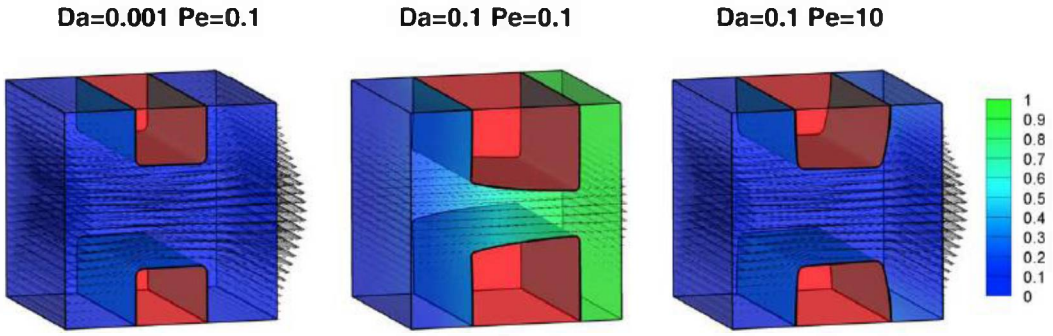

Figure 38. Comparison of pore throat geometry changes due to mineral dissolution under various flow rates and dissolution rates. Both the flow velocity field (black arrows) and the reactant concentration field.

Figure 39. shows the changes of permeability as functions of reduced porosity due to mineral precipitation. Surprisingly, different combinations of flow and reaction rates lead to permeability-porosity curves that all obviously significantly deviate from the widely used power law permeability-porosity curve. These pore-scale simulation results clearly demonstrate the importance to appropriately incorporate pore-scale geochemical process into continuum reservoir models.

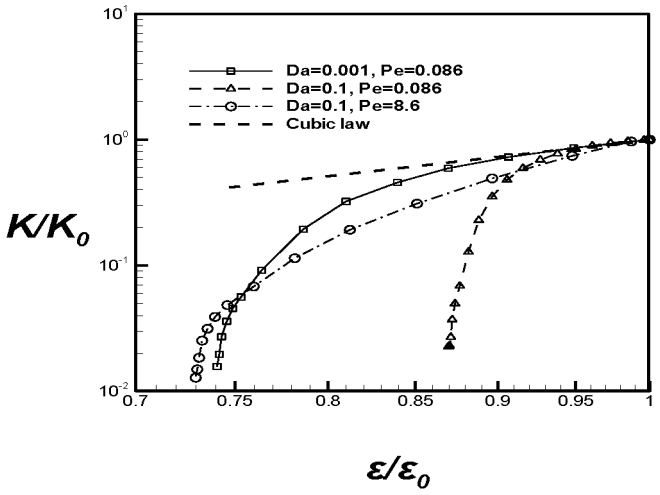

Figure 39. Simulated permeability-porosity reduction curves due to mineral precipitation under various combinations of flow and reaction rates

Development of continuum scale fully coupled, fully implicit reactive transport model for strong coupling between flow and rocks

The new permeability-porosity constitutive relationships due to mineral dissolution/precipitation were implemented in a continuum scale reactive transport model and is used to simulation core flooding experiments (Figure 40) at various flow rates and reaction kinetics. The new reactive transport solves all partial-differential algebraic equations (PDAEs) simultaneously, avoiding decoupling errors from the conventional operator-splitting approach (such as the TOUGHREACT code). The new fully coupled reactive transport model is particularly suitable for CO2 bearing reactive flow simulations. The data collected from the ongoing core flooding experiments was compared with model predictions.

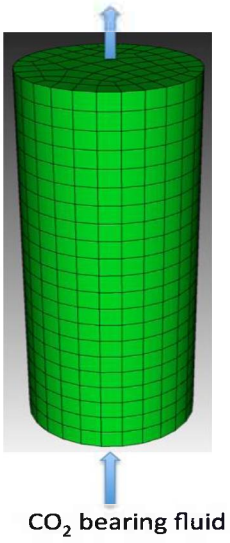

Figure 40. Column reactive transport simulations.

Geomechanical response of fractured reservoir in response to fluid injections.

A discrete element model (DEM) developed at the INL was coupled to the flow model in order to simulate the near wellbore geomechanical response due to fluid injection, and to evaluate the effects of activations of natural fractures to the wellbore injectivity. Unlike the conventional continuum geomechanics models that typically use empirical failure criteria and post-failure mechanical and hydraulic constitutive models, the DEM model explicitly model fracture initiations and follow on propagations. The natural fractures at different orientations, with different mechanical strengths and permeability (depending on the degree of cementations) can be conveniently represented in the DEM model. More importantly, the post-failure (such as slipping and dilation openning of natural fractures) mechanical behaviors and permeability changes are the emerging behaviors of the model itself, instead of using empirical constitutive relationships. Figure 41 shows an example simulation using the DEM model coupled with flow. The injection well is located in the middle and intersecting natural fractures. It is obvious that the injection has led to both slipping and dilation openings of natural fractures near injection well, which in turn significantly changes fracture network permeability and wellbore injectivity.

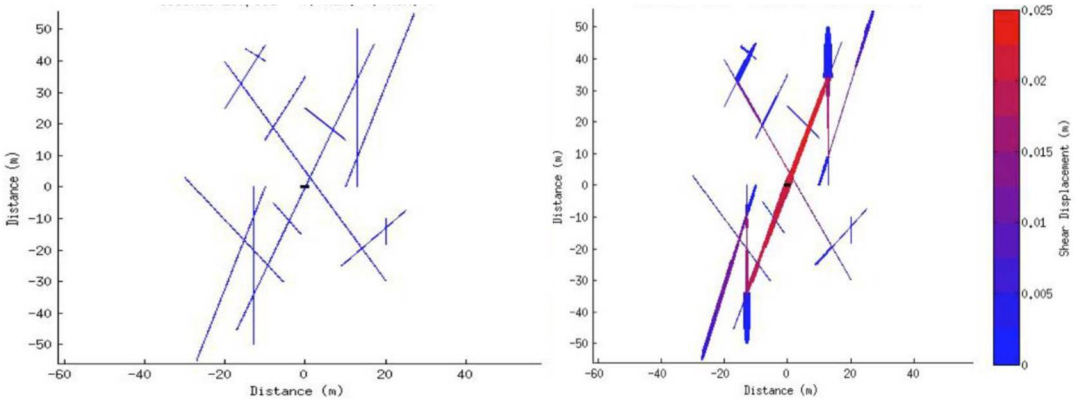

Figure 41. (left) initial natural fracture network; (right) slipping and dilation opening of the natural fractures during fluid injection. The line thickness is scaled with fracture aperture. Along each fracture, the red color indicates amount of shear displacement (slipping), and the blue color indicates dilation opening of the fracture.

INL's discrete element model (DEM) for reservoir geomechanical simulations was extended by incorporating natural fractures into the DEM model. The extended DEM model was then applied to study near wellbore geomechanical response of a fractured reservoir induced by fluid injection. Figure 42 shows the model setup for this study.

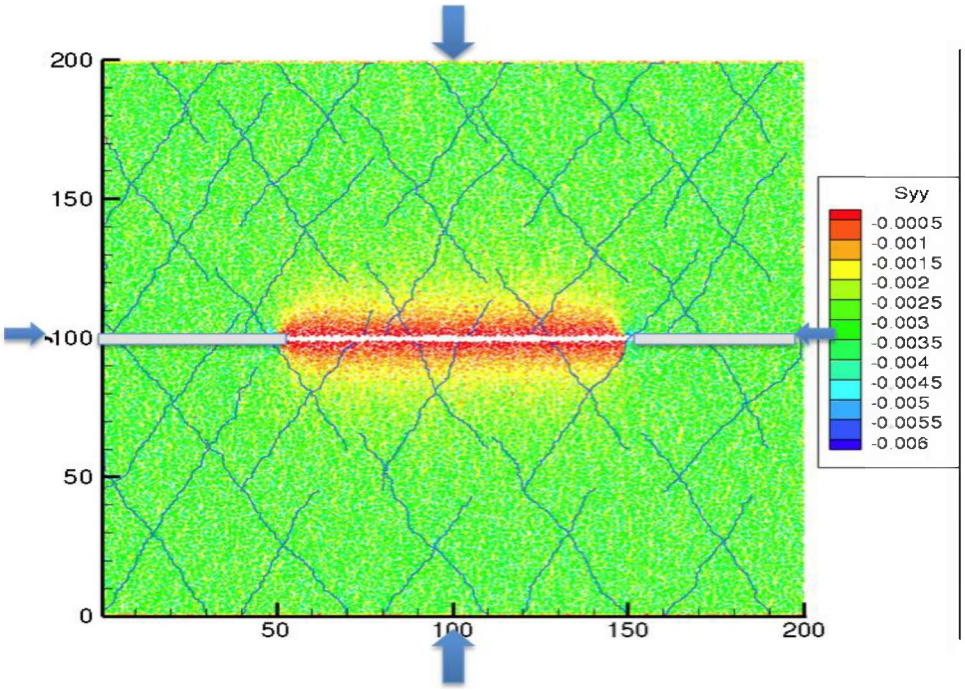

Figure 42. Synthetic fractured reservoir with a horizontal injection well. The injection interval was assumed to be open borehole intersected by the fractures. The rest of the borehole is cased. The color scales with the vertical stress. Fractures are colored by their initial permeability

Figure 43 shows the fluid pressure field and geomecahnical response of the fractured reservoir shortly after the injection was started. After the injection was started, most of injected fluid goes into the nearby fractures connected with the injection wellbore. The fractures immediately adjacent to the wellbore are undergoing stress changes and exhibit local dilatational openings, but without apparent changes of overall fracture network permeability.

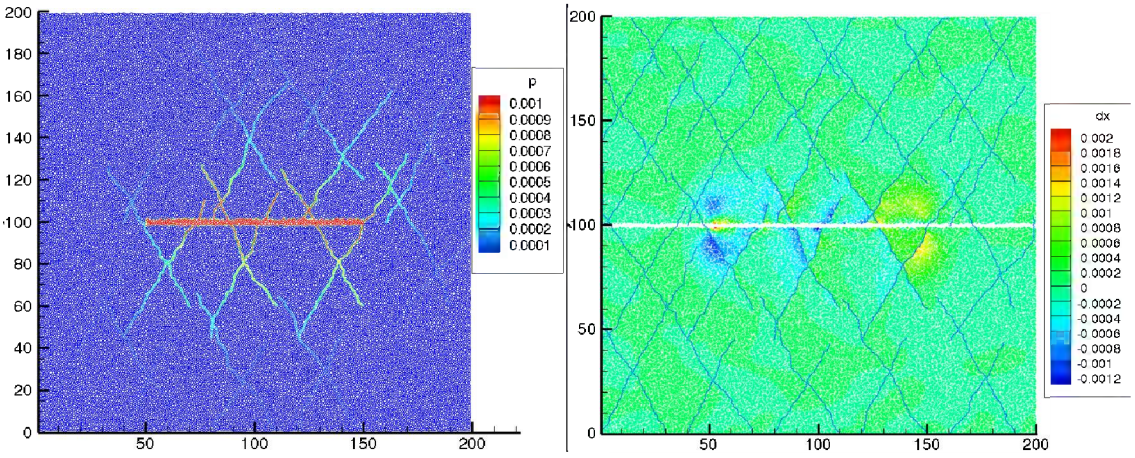

Figure 43. (Left)- fluid pressure distribution shortly after the injection was started; (right) – Horizontal displacement field and fracture network colored by fracture permeability.

Figure 44 shows the fluid pressure field and geomecahnical response of the fractured reservoir long after the injection was started and fluid flow injection approached steady state. Fluid moves into more fractures. A large portion of the fracture network has undergone significant deformations and the network permeability has increased significantly.

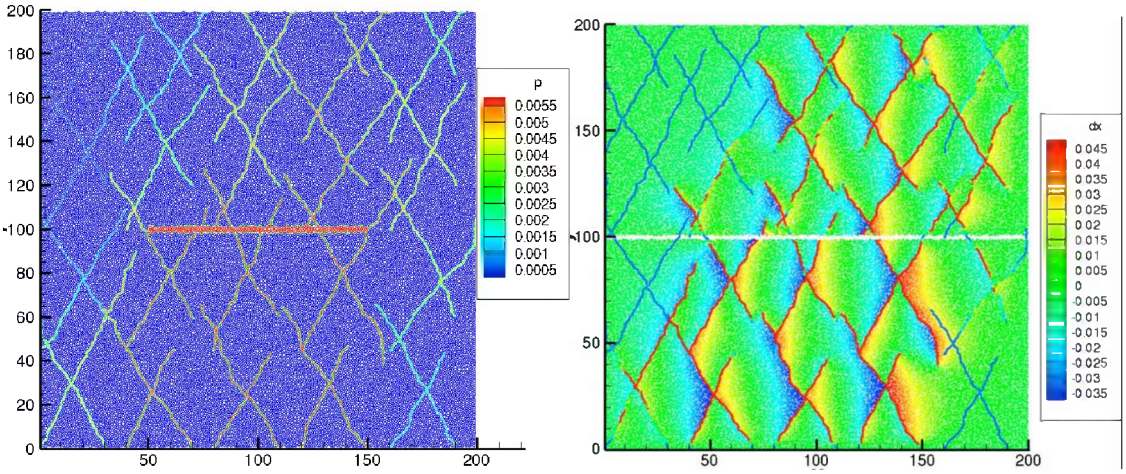

Figure 44. (Left)- fluid pressure distribution long after the injection was started (still below fracturing pressure; (right) – Horizontal displacement field and fracture network colored by fracture permeability.

Figure 45 shows the final horizontal and vertical stress fields as the flow approached steady state. It's clear at the stress concentrations are observed near tips of some natural fractures, where hydraulic fractures are likely to propagate when the fluid pressure reaches fracturing pressure if the injection rate further increases.

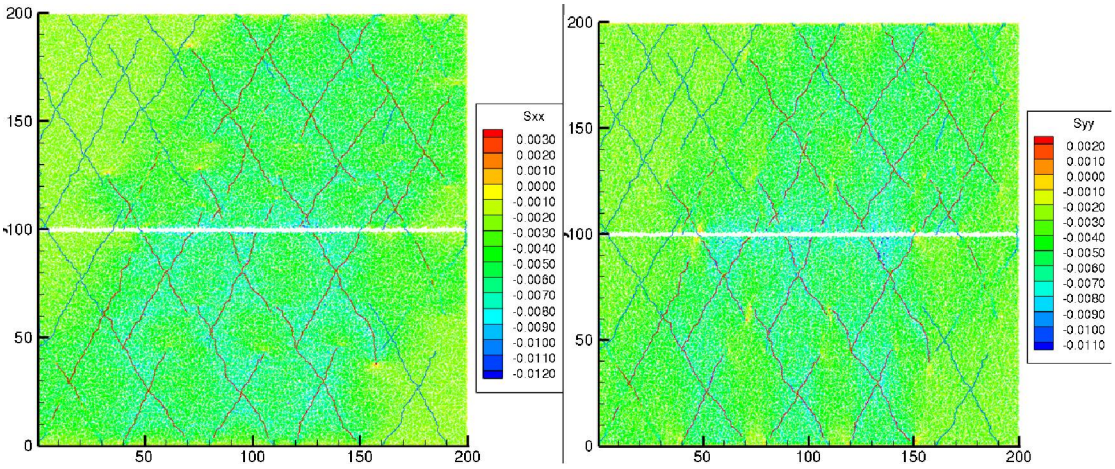

Figure 45. (Left) final horizontal stress field and (right) final vertical stress field.

Unlike the conventional continuum geomechanics models that typically use empirical failure criteria and post-failure mechanical and hydraulic constitutive models, the DEM model explicitly model fracture initiations and follow on propagations. The natural fractures at different orientations, with different mechanical strengths and permeability (depending on the degree of cementations) can be conveniently represented in the DEM model. More importantly, the post-failure (such as slipping and dilation opening of natural fractures) mechanical behaviors and permeability changes are the emerging behaviors of the model itself, instead of using empirical constitutive relationships.

CONCLUSIONS

To better understand mineralogical and petrophysical changes near wellbore host rocks during CO_2 injection, core flooding experiments were designed and set up to model reservoir conditions. Core flooding experiments were performed during which mixtures of CO_2 and brine at different flow rates were injected through near homogenous sandstone, limestone, and dolomite cores at 2000 psi and 60 °C. Mineralogical changes after two weeks of injection have the potential to cause significant petrophysical and subsequent structural changes in sandstone, limestone, and dolomite formations under carbon dioxide sequestration conditions. This was the original hypothesis that was validated using high pressure core floods in this work. Iron chemistry plays an unexpectedly larger role in sequestration in sandstone formations. Dissolution of ankerite and siderite leads to large iron effluent concentrations. A reactive transport model such as TOUGHREACT may be used to explain the complex interconnected reactions with flow. Both simulation and experiment demonstrated the same trend in mineral dissolution, a rapid increase to the critical point and then stabilization. However, some of the flow rate effects observed in the experiments could not be reproduced in the model. In limestone and dolomite, calcium and magnesium bearing minerals dissolve, leading to formation of large dissolution zones, including wormholes. The beginnings of the generation of wormhole type structures were evident at the lower brine and CO_2 flow rate. And finally, a fully developed wormhole was created in limestone when exposed to higher brine and CO_2 flow rates. Similar to the limestone cores, the inlet sections of dolomite were also greatly dissolved. Porosity and permeability changes are small – of the order of 1-2% and similar values result from TOUGHREACT.

Batch experiments were set up and performed at high pressure (2,400 psi) and temperature (60 °C) for two weeks under various experimental conditions to simulate reservoir conditions for CO_2 storage. These experiments showed similar trends in iron in sandstones, and calcium and magnesium in limestone and dolomite. As the surface areas increase by using fracture and powder samples, reactivities increased leading to larger cationic concentrations in brine. Approximate morphology of the reacted volume is viewed using QEMSCAN and Micro-CT for batch samples. Reactions appear to be uniform throughout the volume for limestone and dolomite, whereas they appear to be limited more to the surface in sandstone. When the brine concentration was increased, CO_2 solubility was affected causing slower mineral dissolution rates.

Toughreact simulations were able to capture the general trends in experimental results, but could not reproduce all elements of the data. Reactive transport and geomechanical models were built at Idaho National Laboratory. The geomechanical models showed that slipping and dilatational effects were important in the interaction of the injected fluids with natural fractures.

Sandstones are the most common target rock types for sequestration. Even though extensive dissolution is not expected for sandstone samples, dissolution of iron-bearing minerals (ankerite, siderite and chlorite) has been observed and studied in simulations of larger-scale injections. This study showed that iron bearing minerals do play an important role in sequestering carbon dioxide in sandstone formations and this needs to be carefully considered. The immediate implication of iron chemistry in injection of CO_2 in sandstone is the near wellbore injectivity, which would likely increase as dissolution proceeds. Some distance downstream of injection, increased iron concentration in the aqueous phase may lead to precipitation. These pore-level changes may induce geomechanical changes in the formation. These changes may lead to induction of fractures or fault reactivation. In limestones and dolomites, dissolution is extensive and may weaken the formation making it susceptible to failure. Simulation tools developed at the Idaho National Laboratory showed that tensile and shear failures are possible.

Papers and Presentations

Hyukmin Kweon, Christian Payne, Milind Deo, "Reactive and pore structure changes in carbon dioxide sequestration". **Ind. Eng. Chem. Res.**, 2015, 54 (16), pp 4552–4560

Luanjing Guo, Hyukmin Kweon, Milind Deo "Numerical Modeling Study of CO_2 Storage in Brine Aquifer in Ferric Iron-Bearing Sandstone". **Proceedings of the 5th International Symposium GeoProc2015**

Hyukmin Kweon and Milind Deo, "Study of Mineralogical and Petrophysical Changes regarding Different Rock Types and Physical forms under Reservoir Conditions". (In progress)

Ting Xiao, Hyukmin Kweon, Brian McPherson, Milind Deo, "Simulation of wormhole formation regarding to variable parameters in Indiana limestone". (In progress)

"Mineralogical and petrophysical changes in carbon dioxide sequestration". **Oral Presentation** at the US-Korea Conference 2016, Hyatt Regency DFW, Dallas, TX, USA, August 10-13, 2016 (Accepted)

"Selective recovery of precious metals mineral carbonation under different alkali concentrations from Great Salt Lake in a reactive CO_2 system". **Poster presentation** at the Annual Carbon Capture, Utilization & Storage Conference, Sheraton Tysons Corner, Tysons, VA, USA, June 14-16, 2016 (Accepted)

"Dissolution and Precipitation of minerals under different alkali concentrations in a reactive CO2 batch system". **Poster presentation** at 2016 Spring Meeting and 12th Global Congress on Process Safety, Hilton Americas and George R. Brown Convention Center, Houston, TX, USA, April 10-14, 2016

"Mineralogical and petrological changes in carbon dioxide sequestration". **Oral presentation** at the 6th Korea Carbon Capture and Sequestration International Conference, Maison Glad Jeju, Jeju-si, Jeju-do, South Korea, January 27-29, 2016

"Mineralogical Changes in Iron-bearing Sandstone with CO_2 injection". **Poster Presentation** at the US-Korea Conference 2015, Hyatt Regency Atlanta, Atlanta, GA, USA, July 29– August 1, 2015

"CO_2 Storage in Iron-Bearing Sandstone and Porosity and Mineralogical Changes under Flow Conditions". **Poster presentation** at the 14th Annual Carbon Capture, Utilization & Storage Conference, The Wyndham Grand, Pittsburgh, PA, USA, April 28-May 1, 2015

"Porosity and mineralogical changes in iron-bearing sandstone with CO_2 injection". **Oral presentation** at 2015 Spring Meeting and 11th Global Congress on Process Safety, Hilton Austin, Austin, TX, USA, April26-30, 2015

"Numerical Modeling Study of CO_2 Storage in Brine Aquifer in Ferric Iron-Bearing Sandstone". **Oral presentation** at GeoProc 2015, Salt Lake City Marriott University Park, Salt Lake City, UT, USA, February25-27, 2015

"Reactive and Pore Structure Changes in Carbon Dioxide Sequestration". **Oral presentation** at Energy, Utility & Environment Conference 2015,San Diego convention center, San Diego, CA, USA, February16-18, 2015

"Study of Petrophysical and Mineralogical Changes in Reactive CO_2 Systems". **Oral presentation** at the American Institute of Chemical Engineers Annual meeting, Atlanta Marriott Marquis & Hilton Atlanta, Atlanta, GA, USA, November16-21, 2014

"Mineralogical Changes regarding to CO_2 Concentration in a Reactive CO_2 System". **Poster presentation** at the Carbon Storage R&D Project Review Meeting, Sheraton Station Square, Pittsburgh, PA, USA, August12-14, 2014

"Study of Porosity regarding Different Rocks in Core-Flooding Systems". **Poster presentation** at the US-Korea Conference 2014, Hyatt Regency San Francisco Airport Hotel, San Francisco, CA, USA, August6-9, 2014

"Study of CO_2 sequestration regarding different rock types in batch and core-flooding systems". **Poster presentation** at the Air & Waste Management Association's 107th Annual Conference & Exhibition, Long Beach Convention Center, Long Beach, CA, USA, June 24-27, 2014

"Experimental Evaluation of Petrophysical and Mechanical Changes in a Reactive CO_2 system". **Poster presentation** at the Annual Carbon Capture, Utilization & Storage Conference, David L. Lawrence Convention Center, Pittsburgh, PA, USA, April 28-May 1, 2014

"Reactive Transport Simulations and Experiments of Carbon Dioxide Injection". **Poster presentation** at the Energy &Geoscience Institute Technical Meeting, Salt Lake City Marriott University Park, Salt Lake City, UT, USA, April 26- May 1, 2014

"Coupled Reactive Transport Model with Geomechanics to Mitigate Risks CO_2 Geological Storage". **Poster presentation** at Carbon Storage R&D Project Review Meeting, Sheraton Station Square, Pittsburgh, PA, USA, August 20 - 22, 2013

References

Bachu, S. (2008). "CO2 storage in geological media: Role, means, status and barriers to deployment." Progress in Energy and Combustion Science **34**(2): 254-273.

Bachu, S., Bennion, D. Brant (2009). "Chromatographic partitioning of impurities contained in a CO2 stream injected into a deep saline aquifer: Part 1. Effects of gas composition and in situ conditions." International Journal of Greenhouse Gas Control **3**(4): 458-467.

Ben Baccar, M., Fritz, Bertrand, Made, Benoit (1993). "Diagenetic albitization of K-feldspar and plagioclase in sandstone reservoirs; thermodynamic and kinetic modeling." Journal of Sedimentary Research **63**(6): 1100-1109.

Carling, G. T., Fernandez, Diego P., Johnson, William P. (2012). "Dust-mediated loading of trace and major elements to Wasatch Mountain snowpack." Science of The Total Environment **432**(0): 65-77.

Carroll, S. A., W. W. McNab, Z. Dai and S. C. Torres (2013). "Reactivity of Mount Simon Sandstone and the Eau Claire Shale Under CO2 Storage Conditions." Environmental Science & Technology **47**(1): 252-261.

Castelletto, N., P. Teatini, G. Gambolati, D. Bossie-Codreanu, O. Vincké, J.-M. Daniel, A. Battistelli, M. Marcolini, F. Donda and V. Volpi (2013). "Multiphysics modeling of CO2 sequestration in a faulted saline formation in Italy." Advances in Water Resources **62, Part C**(0): 570-587.

Corey, A. T. (1954). "The interrelation between gas and oil relative permeabilities " Producers Monthly **19**(1): 38-41.

Court, B., Bandilla, Karl W., Celia, Michael A., Janzen, Adam, Dobossy, Mark, Nordbotten, Jan M. (2012). "Applicability of vertical-equilibrium and sharp-interface assumptions in CO2 sequestration modeling." International Journal of Greenhouse Gas Control **10**(0): 134-147.

D. Garcia, C. L. L., and J.D. Miller (2006). "Experimental Evaluation of a Mineral Exposure Model for Crushed Copper Ores." Society for mining, metallurgy, and Exploration, Inc. (SME): 261-268.

De Silva, G. P. D., P. G. Ranjith and M. S. A. Perera (2015). "Geochemical aspects of CO2 sequestration in deep saline aquifers: A review." Fuel **155**(0): 128-143.

Gaus, I. A., Mohamed Czernichowski-Lauriol, Isabelle (2005). "Reactive transport modelling of the impact of CO2 injection on the clayey cap rock at Sleipner (North Sea)." Chemical Geology **217**(3–4): 319-337.

Gottlieb, P. W., G. Sutherland, D. Ho-Tun, E. Suthers, S. Perera, K. Jenkins, B. Spencer, S. Butcher, A. Rayner, J. (2000). "Using quantitative electron microscopy for process mineralogy applications." JOM **52**(4): 24-25.

Hoffert, M. I., K. Caldeira, G. Benford, D. R. Criswell, C. Green, H. Herzog, A. K. Jain, H. S. Kheshgi, K. S. Lackner, J. S. Lewis, H. D. Lightfoot, W. Manheimer, J. C. Mankins, M. E. Mauel, L. J. Perkins, M. E. Schlesinger, T. Volk and T. M. L. Wigley (2002). "Engineering: Advanced technology paths to global climate stability: Energy for a greenhouse planet." Science **298**(5595): 981-987.

Keeling, C. D. (1997). "Climate change and carbon dioxide: An introduction." Proceedings of the National Academy of Sciences **94**(16): 8273-8274.

Kharaka, Y. K., D. R. Cole, J. J. Thordsen, E. Kakouros and H. S. Nance (2006). "Gas–water–rock interactions in sedimentary basins: CO2 sequestration in the Frio Formation, Texas, USA." Journal of Geochemical Exploration **89**(1–3): 183-186.

Kongsjorden, H., O. Kårstad and T. A. Torp (1998). "Saline aquifer storage of carbon dioxide in the Sleipner project." Waste Management **17**(5–6): 303-308.

Kweon, H., Payne, Christian, Deo, Milind (2015). "Reactive and Pore Structure Changes in Carbon Dioxide Sequestration." Industrial & Engineering Chemistry Research **54**(16): 4552-4560.

Lai, P., Moulton, Kevin, Krevor, Samuel (2015). "Pore-scale heterogeneity in the mineral distribution and reactive surface area of porous rocks." Chemical Geology **411**: 260-273.

Lasaga, A. C. (1984). "Chemical kinetics of water-rock interactions." Journal of Geophysical Research: Solid Earth **89**(B6): 4009-4025.

Lee, M., Wang, Sookyun, Kim, Seyoon, Park, Jinyoung (2015). "Investigation of the Relationship between CO2 Reservoir Rock Property Change and the Surface Roughness Change Originating from the Supercritical CO2-Sandstone-groundwater Geochemical Reaction at CO2 Sequestration Condition." Energy Procedia **76**: 495-502.

Li, L., Peters, Catherine A., Celia, Michael A. (2007). "Applicability of averaged concentrations in determining geochemical reaction rates in heterogeneous porous media." American Journal of Science **307**(10): 1146-1166.

Lin, C. L. G., C. (2005). "Microscale Characterization and Analysis of Particulate Systems via Cone-Beam X-ray Microtomography (XIMT)." Innovations in Natural Resource Processing: 421-432.

Matisoff, W. C. E. a. G. (1996). "Evaluation of Kinetic Models for the Smectite to Illite Transformation." Clays and Clay Minerals **44**(1): 77-87.

Miller, J. D., Lin, C. L., Garcia, C., Arias, H. (2003). "Ultimate recovery in heap leaching operations as established from mineral exposure analysis by X-ray microtomography." International Journal of Mineral Processing **72**(1–4): 331-340.

Mora, C., A. G. Frazier, R. J. Longman, R. S. Dacks, M. M. Walton, E. J. Tong, J. J. Sanchez, L. R. Kaiser, Y. O. Stender, J. M. Anderson, C. M. Ambrosino, I. Fernandez-Silva, L. M. Giuseffi and T. W. Giambelluca (2013). "The projected timing of climate departure from recent variability." Nature **502**(7470): 183-187.

Morris, J. P., R. L. Detwiler, S. J. Friedmann, O. Y. Vorobiev and Y. Hao (2011). "The large-scale geomechanical and hydrogeological effects of multiple CO2 injection sites on formation stability." International Journal of Greenhouse Gas Control **5**(1): 69-74.

Navarre-Sitchler, A. and G. Thyne (2007). "Effects of carbon dioxide on mineral weathering rates at earth surface conditions." Chemical Geology **243**(1–2): 53-63.

Oelkers, E. H. and J. Schott (2005). "Geochemical aspects of CO2 sequestration." Chemical Geology **217**(3–4): 183-186.

Okwen, R. T., M. T. Stewart and J. A. Cunningham (2010). "Analytical solution for estimating storage efficiency of geologic sequestration of CO2." International Journal of Greenhouse Gas Control **4**(1): 102-107.

Olajire, A. A. (2013). "A review of mineral carbonation technology in sequestration of CO 2." Journal of Petroleum Science and Engineering **109**: 364-392.

Rathnaweera, T. D., P. G. Ranjith, M. S. A. Perera and S. Q. Yang (2015). "Determination of effective stress parameters for effective CO2 permeability in deep saline aquifers: An experimental study." Journal of Natural Gas Science and Engineering **24**(0): 64-79.

Reeder, R. J. and W. A. Dollase (1989). "Structural variation in the dolomite-ankerite solid-solution series; an X-ray, Moessbauer, and TEM study." American Mineralogist **74**(9-10): 1159-1167.

Salimi, H., K.-H. Wolf and J. Bruining (2012). "The influence of capillary pressure on the phase equilibrium of the CO2–water system: Application to carbon sequestration combined with geothermal energy." International Journal of Greenhouse Gas Control **11, Supplement**(0): S47-S66.

Schott, J., Pokrovsky, Oleg S., Oelkers, Eric H. (2009). "The Link Between Mineral Dissolution/Precipitation Kinetics and Solution Chemistry." Reviews in Mineralogy and Geochemistry **70**(1): 207-258.

Siegenthaler, U., Oeschger, Hans (1987). "Biospheric CO2 emissions during the past 200 years reconstructed by deconvolution of ice core data." Tellus B **39**(1-2): 140-154.

Smith, M. M., Wolery, Thomas J., Carroll, Susan A. (2013). "Kinetics of chlorite dissolution at elevated temperatures and CO2 conditions." Chemical Geology **347**: 1-8.

Sohrabi, M., N. I. Kechut, M. Riazi, M. Jamiolahmady, S. Ireland and G. Robertson (2012). "Coreflooding Studies to Investigate the Potential of Carbonated Water Injection as an Injection Strategy for Improved Oil Recovery and CO 2 Storage." Transport in Porous Media **91**(1): 101-121.

Song, Z., H. Song, Y. Cao, J. Killough, J. Leung, G. Huang and S. Gao (2015). "Numerical research on CO2 storage efficiency in saline aquifer with low-velocity non-Darcy flow." Journal of Natural Gas Science and Engineering **23**(0): 338-345.

Tiwari, P., Deo, M., Lin, C. L., Miller, J. D. (2013). "Characterization of oil shale pore structure before and after pyrolysis by using X-ray micro CT." Fuel **107**(0): 547-554.

van Genuchten, M. T. (1980). "A Closed-form Equation for Predicting the Hydraulic Conductivity of Unsaturated Soils1." Soil Science Society of America Journal **44**(5).

Wang, Q., J. Luo, Z. Zhong and A. Borgna (2011). "CO2 capture by solid adsorbents and their applications: Current status and new trends." Energy and Environmental Science **4**(1): 42-55.

Wawersik, W. R. R., John W.Dove, Patricia Harris, JerryLogan, John M. Pyrak-Nolte, LauraOrr Jr, Franklin M. Ortoleva, Peter J.Richter, FrankWarpinski, Norman R. Wilson, John L.Wong, Teng-Fong (2001). Terrestrial sequestration of CO2: An assessment of research needs. Advances in Geophysics. D. Renata and S. Barry, Elsevier. **Volume 43:** 97-IX.

Wilson, E. J., T. L. Johnson and D. W. Keith (2003). "Regulating the Ultimate Sink: Managing the Risks of Geologic CO2 Storage." Environmental Science & Technology **37**(16): 3476-3483.

Xu, T., Apps, John A., Pruess, Karsten (2003). "Reactive geochemical transport simulation to study mineral trapping for CO2 disposal in deep arenaceous formations." Journal of Geophysical Research: Solid Earth **108**(B2): n/a-n/a.

Xu, T., Kharaka, Yousif K., Doughty, Christine, Freifeld, Barry M., Daley, Thomas M. (2010). "Reactive transport modeling to study changes in water chemistry induced by CO2 injection at the Frio-I Brine Pilot." Chemical Geology **271**(3–4): 153-164.

Xu, T. and K. Pruess (1998). Coupled modeling of non-isothermal multiphase flow, solute transport and reactive chemistry in porous and fractured media: 1. Model Development and Validation.

Zhou, Q., J. T. Birkholzer, C.-F. Tsang and J. Rutqvist (2008). "A method for quick assessment of CO2 storage capacity in closed and semi-closed saline formations." International Journal of Greenhouse Gas Control **2**(4): 626-639.